MEASUREMENT OF CHARM MESON PRODUCTION IN AU+AU COLLISIONS AT $\sqrt{S_{NN}}$ =200 GEV

A dissertation submitted

to Kent State University in partial

fulfillment of the requirements for the

degree of Doctor of Philosophy

by

Amilkar Quintero

May, 2016

Dissertation written by

Amilkar Quintero

Licenciado en Fisica, Universidad de Carabobo, 2007

M.S., Florida Institute of Technology, 2010

Ph.D., Kent State University, 2016

Approved by

_____ , Chair, Doctoral Dissertation Committee
Dr. Spyridon Margetis

_____ , Members, Doctoral Dissertation Committee
Dr. Flemming Videbaek

_____ ,
Dr. Declan Keane

_____ ,
Dr. Michael Strickland

_____ ,
Dr. Robert Twieg

_____ ,
Dr. Robin Selinger

Accepted by

_____ , Chair, Department of Physics
Dr. James T. Gleeson

_____ , Dean, College of Arts and Sciences
Dr. James L. Blank

TABLE OF CONTENTS

LIST OF FIGURES

LIST OF TABLES

ACKNOWLEDGEMENTS

All my gratitude goes to Dr. Spiros Margetis, for giving me the chance to work with him. During the entire program, I learned a lot of very important and interesting topics of physics. Beside physics, he also taught me to become a better person. He was an excellent advisor.

I was very honored to work under the supervision of Dr. Flemming Videbaek. He definitely made a huge impact in my professional life. I am will try to follow his example all my life since it is incredible the deep knowledge of physics he has and the ability to manage, almost perfectly, administrative task without losing performance.

I want to thank all STAR collaboration at BNL specially the software and computing group and Dr. Yuri Fisyak. Yuri is an inspiration for me, he introduced me to this wonderful world of computing; without his help none of this work would be possible. I want to thank also the STAR LBL group for the support with the HFT program and the analysis tasks.

Thanks to all my colleagues at Kent State, especially to Dr. Jonathan Bouchet, Michael Lomnitz, Prashanth Shanmuganathan and Ayman Hamad, for their help in this work and their friendship.

I want to dedicate this thesis to God, my parent and all my family in particular to Vianney for all the support that she gave.

CHAPTER 1

Introduction

The search for the origin of our universe has led scientists to study the most primitive states of the matter known such as the Quark Gluon Plasma (QGP), a state that was discovered in 2005 by the Relativistic Heavy Ion Collider (RHIC) at Brookhaven National Laboratory (BNL). QGP is a state of the matter where quarks and gluons are free to move over the extended volume of a nucleus, beyond the boundaries of individual nucleons [Adams et al. 2005; Adcox et al 2005; Arsene et al. 2005; Back et al. 2005]. The creation of QGP appears to contradict the basic confinement principle of Quantum Chromo Dynamics (QCD), the theory of strong interaction, which states that it is impossible to have free quarks [Gross, Wilczek 1973; Politzer 1973]. Current heavy ion collisions reach very high energies that can compress and heat matter to such extremes that can "liberate" the quarks and gluons of a nuclei for a very short period of time. The behavior of nuclear matter at these energies has never been studied experimentally so most of their properties are still unknown. One of the features of this exotic matter found at RHIC is its low shear viscosity, which is very close to the theoretical limit, so it is referred to as the "Perfect Liquid". Another feature, that is a direct outcome of work like the one presented in this dissertation, is that the hot nuclear matter we create in the lab behaves does not behave like a weakly interacting gas but rather as a strongly interacting liquid. Because of these the created hot nuclear matter found at RHIC is called sQGP where "s" is for "strongly interacting" plasma.

The extreme temperature and density that creates the QGP is similar to the conditions at few microseconds after the Big Bang. The study of QGP could clarify some of the properties of the Big Bang. This can be done in a controlled and systematic way in laboratory conditions. However, there is little knowledge about this state of matter; QCD-based theories and models are being tested and challenged to describe these new findings in order to reveal and uncover the underlying physics.

1.1 The Standard Model

One of the major successes in modern physics is the Standard Model (SM), since it organizes the world of subatomic particles and their interactions in a consistent and robust scheme. It was established in 1970 by several authors around the world and its predictions are still being tested, like the discovery of the Higgs Boson in 2012.

The Standard Model is a prelude of a unified field theory or "the Theory of Everything" postulated by Einstein after his theory of general relativity in 1915 because the Standard Model clusters three of the four known forces in nature: strong, weak and electromagnetic. The Standard Model fails to incorporate the gravitational force because current theoretical frameworks have failed to apply a renormalizable quantum field theory to gravity at Planck scales [Zee 2010].

The initial classification of the elementary particles in the SM comes due to their spin: fermions have half integer spin and bosons with integer spin. The bosons are the force carriers, so they are responsible of the interaction between particles. The currently known bosons are: the photon (γ) is the force carrier of electromagnetic force, the Z^0 and $W^{+/-}$ force carrier of the weak nuclear force (although W bosons have electric charge so

they experience electromagnetic force too), the gluons are the force carriers of the strong force, and the Higgs boson which is the carrier particle of the Higgs Field that interacts with most elementary particles (not photons nor gluons) and can explain the mechanism of how these particles acquire their masses. The Higgs boson does not have intrinsic spin (spin zero) so it can be classified as a boson [Aad et al. 2013]. The table 1.1 summarizes the Bosons in the Standard model.

Table 1.1: Bosons in the Standard Model and their properties [CPEP 2014].

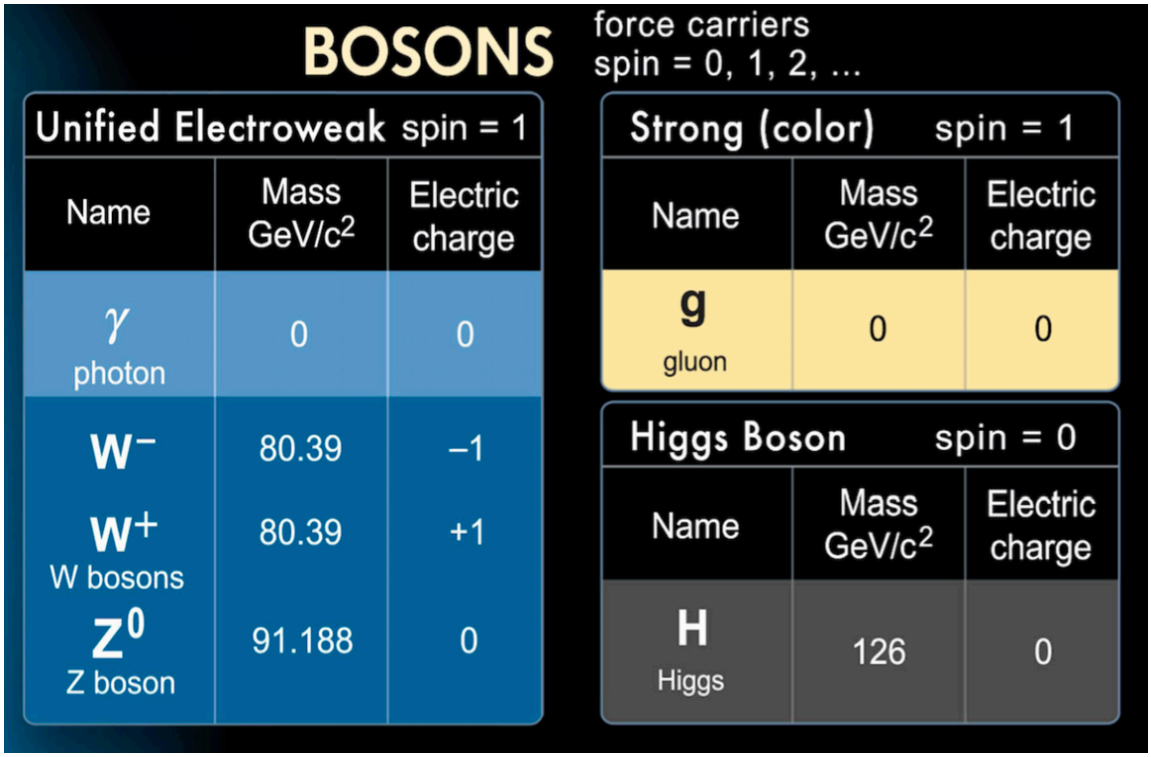

On the other hand, the fermions are the particles that constitute common matter. The fermions can be separated into two categories depending on their electric charge. The

fermions with integer charge are called leptons. There are six leptons, which are: the electron, the muon (μ) and the tau (τ), each of these has a neutrino associated. Fermions with third integer charge are called quarks. There are also six known (flavor) quarks: up, down, charm, strange, top and bottom. Pairs from each classification of quarks and leptons show similar physical behavior so they are grouped together to form a generation. Table 1.2 shows the classification of the fermions with a summary of some of their most important properties.

Table 1.2: Fermions in the Standard Model and their properties [CPEP 2014].

FERMIONS matter constituents spin = 1/2, 3/2, 5/2, …

Leptons spin =1/2			Quarks spin =1/2		
Flavor	Mass GeV/c^2	Electric charge	Flavor	Approx. Mass GeV/c^2	Electric charge
ν_L lightest neutrino*	$(0-2)\times10^{-9}$	0	**u** up	0.002	2/3
e electron	0.000511	−1	**d** down	0.005	−1/3
ν_M middle neutrino*	$(0.009-2)\times10^{-9}$	0	**c** charm	1.3	2/3
μ muon	0.106	−1	**s** strange	0.1	−1/3
ν_H heaviest neutrino*	$(0.05-2)\times10^{-9}$	0	**t** top	173	2/3
τ tau	1.777	−1	**b** bottom	4.2	−1/3

Another major difference between quarks and leptons is the forces that govern their interactions. Leptons are influenced by electromagnetic and weak nuclear forces,

except the neutrinos that interact only weakly since they do not have electric charge. Quarks interact with each other via the strong nuclear force by exchange of gluons (details in next section). However quarks can also interact with fermions via electromagnetic (photons too) or weak nuclear force.

In addition to all of the particles mentioned, each fermion has a counter particle called anti-particle which has the same mass and spin but opposite electric charge and other quantum numbers. Bosons are their own antiparticles.

1.2 Quantum Chromo Dynamics and the Quark Model

Quantum Chromo Dynamics (QCD) is the physics theory that describes the nuclear (strong) force, which governs the interaction between quarks and gluons. Analogous to Quantum Electro Dynamics (QED) where the photon is the force carrier, gluons are the force carriers in QCD. Major differences arise since there is only one force carrier in QED (the photon) while in QCD there are eight different gluons. QCD is a non-Abelian gauge theory with the SU(3) symmetry group.

The electrons and the interaction between quarks produce all the common (or detectable) matter known in the universe. When quarks bind together they form *Hadrons*. Hadrons are the association of two or more quarks. In the Quark Model they are divided into two main categories: *mesons* which are the binding of one quark and one anti quark, and *baryons* which are the union of three quarks or three antiquarks.

During the development of the Standard Model, new particles were discovered, causing some confusion with the theory at the time. Baryons with three quarks and identical spin contradict the Pauli exclusion principle. The discovery of these new

particles leads to the conclusion that a new degree of freedom must be introduced to form hadrons. The "color charge" was introduced to address this issue. Analogous to the colors in the visual spectrum, quarks and gluon can have three different color charges: Red, Green and Blue, and its corresponding opposite color charge anti-Red, anti-Green and anti-Blue. With the introduction of color charge, hadrons can be formed when the total color charge is neutral; this is when the sum of the color charges produces white, like with the visual spectrum, or the color cancels like a Red plus anti-Red combination. A baryon must form with one red, one green and one blue quark; while a meson forms from the union of one color quark and one anti-color anti-quark.

This theory seems not to be restricted to hadrons of two and three quark combinations. Recently, exotic hadrons have been reported; hadrons formed by tetra-quarks (results called into question) [Aaij et al. 2014] and penta-quarks [Aaij et al. 2015]. From the start of QCD theory and with its continuous development there was no theoretical reason to exclude hadrons with more than three quarks as long as the total color charge remains neutral; however it took more than fifty years to prove them.

In contrast to the photons in QED that do not carry electric charge, gluons like the quarks also carry color charge, so they can also interact with themselves. The eight different existing gluons come from the superposition of a gluon to be in a combined state of color and anti color with a normalized probability in SU(3). The gluon self-interaction combined with the specific number of quark flavors give rise to two singular properties of QCD, which are *confinement* and *asymptotic freedom*.

1.2.1 Confinement and Asymptotic Freedom

Confinement in QCD means that states of isolated quarks do not exist. Since the strength of the interaction between quarks keeps growing as one tries to separate them, eventually the interaction will be sufficient to create a quark anti-quark pair from the vacuum, instead of further separating the original quarks. There is no exact analytic proof of the confinement in QCD, since numerical or perturbative approximations must be used to solve the renormalization group equation of the strong coupling constant. However all the searches for free quarks have given so far negative results [Olive et al. 2015].

In QED, a virtual cloud of particle-antiparticle pairs screened a charge particle in vacuum. This effect is completely analogous to the polarization in a dielectric medium. The strength of the interaction (coupling constant) becomes larger in short distances by providing the particle with large momentum transfer, because the virtual cloud is being penetrated closer to the bare charge. On the other hand, when the momentum transfer is small, the strength of the interaction converges to its asymptotic value that is the fine structure constant $\alpha \approx 1/137$; so classical rules of electrodynamics can be applied. This scenario is inverted in QCD due to self-interaction of the gluon octet.

The value of the strong coupling constant is not exactly predicted by the theory but it can be obtained experimentally. However at one loop order (first order approximation) provides a running strong coupling (α_s) depending on momentum transfer (Q). Equation (1.1) shows this relation:

$$\alpha_s(Q^2) = \frac{12\pi}{(33 - 2n_F)\ln(Q^2/\Lambda^2)} \tag{1.1}$$

where n_F is the number of quark flavors and Λ is a dimensional parameter which is experimentally constraint to be $\Lambda_{QCD} \sim 0.22$ GeV [Ryder 1996]. As long as the n_F is below 16 (and we currently have only 6 quark flavors) the α_s will decrease at higher energies. From the equation (1.1), confinement can be seen at small momentum transfer (equivalent to large distances) since the strong coupling increased rapidly, making the interaction stronger which translates to unfeasibility of free quarks. Figure 1.1 shows the results obtained by different experiments for the strong coupling constant value in QCD. The other interesting feature of QCD occurs when the momentum transfer is small. This is called asymptotic freedom.

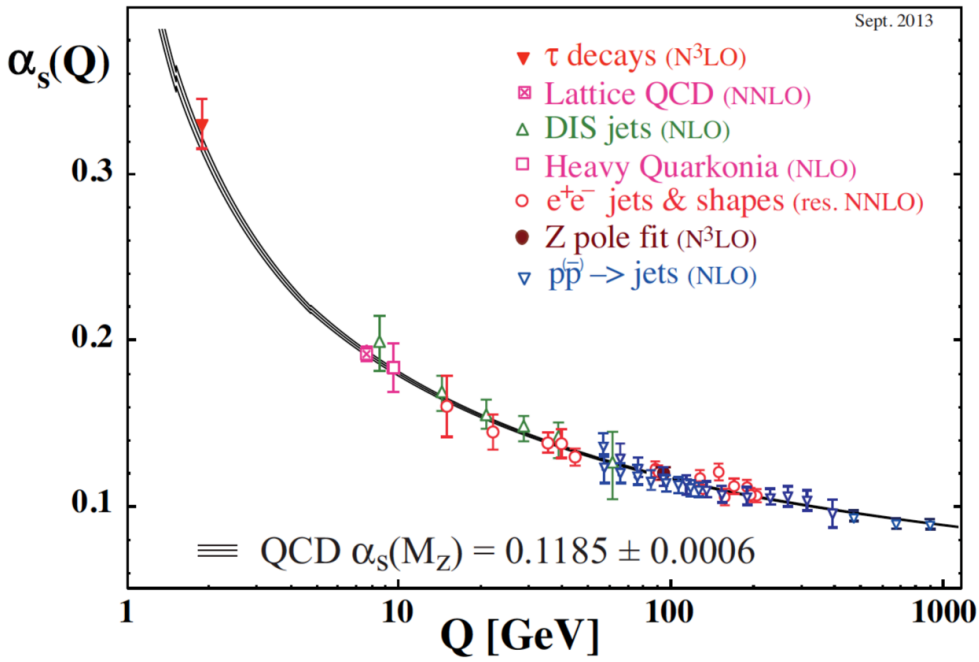

Figure 1.1: Current summary of measurements of α_s as a function of the energy scale Q [Olive et al. 2014].

At very high energies or small distances the strong coupling is very weak (see Figure 1.1) so the bond between quarks can be broken and quarks can move freely. The diminishing of the strong coupling is due to the color screening. While the distance between quarks reduces (high energy), the sum of the gluon interaction in the virtual color charge cloud will reduce the strength of the bare color charge of the particle. If these free quarks are strongly coupled and not diluted, a new state of matter can be produced called the Quark Gluon Plasma.

1.3 Quark Gluon Plasma

The Quark Gluon Plasma (QGP) is a state of matter produced in very high-energy nuclear collisions where the necessary high temperature and density conditions can be created. The coupling between the quarks of both the incoming nuclei and the produced particles gets weaker and therefore the quarks (and gluons) behave like quasi-free particles. Where the crossover of the phase transition between QGP and the hadronic phase happens is still unknown. Lattice QCD calculations suggest that this critical temperature is around 155 MeV (~1.8×10^{12} Kelvin); however this temperature has not been confirmed by experimental data [Muller 2015]. Figure 1.2 shows a representation of the QCD phase diagram expected for nuclear matter. At low temperature and low baryon chemical potential, QCD spontaneously breaks chiral symmetry. This mechanism allows quark to acquire mass 99% of their mass. When the temperature and the density reach a certain value, chiral symmetry is restored for light quarks (up, down and strange) so they behave, as if they are massless [Ryder 1996].

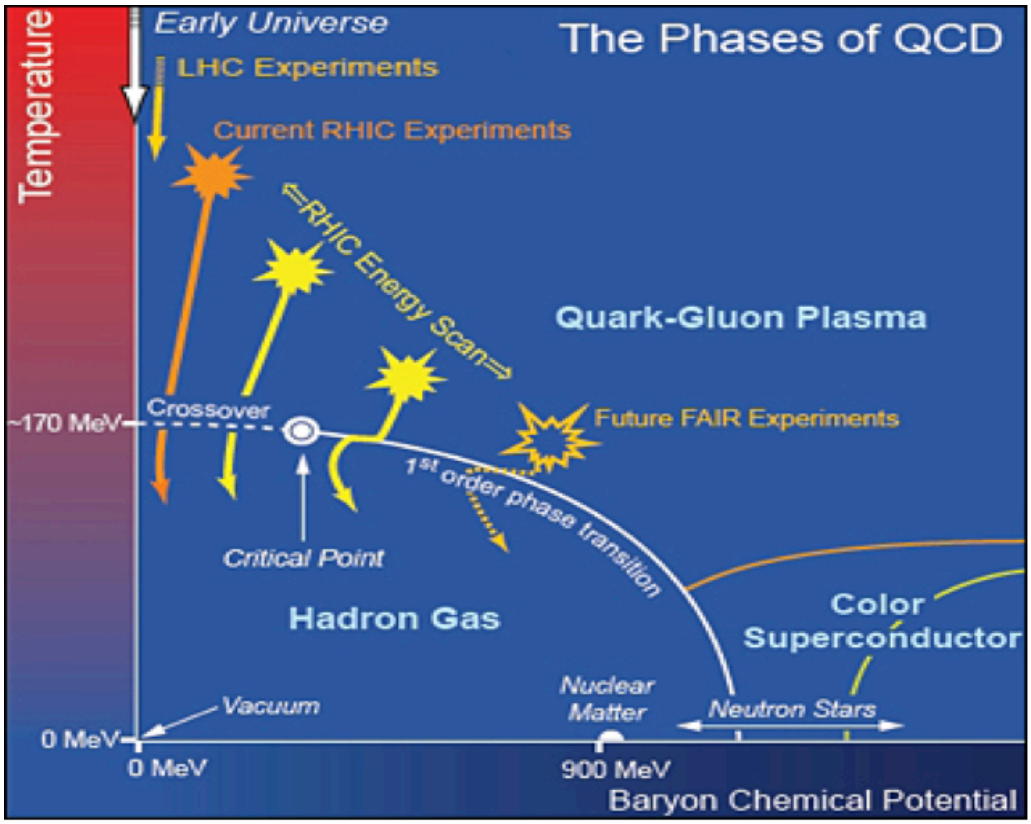

Figure 1.2: A QCD phase-diagram sketch of nuclear matter. Lines show the boundaries of the phases and the regions studied by different experiments [Bushwick 2010].

A phase transition will arise in the system due to the chiral restoration. A second order phase transition (in the traditional sense of statistical mechanics) is expected to occur at zero or low baryon chemical potential. Lattice QCD cannot conclusively prove this hypothesis, but has defined the critical temperature at 155 MeV. Experimental data is needed. In the case of an excess in the baryon chemical potential, Lattice calculations have also shown that the Hagedorn's statistical bootstrap model with an exponential growing mass spectrum of hadrons describe the equation of state of QCD and other

observables, at lower temperatures than the critical temperature, with very good agreement. The Hagedorn gas model undergoes a first order phase transition [Muller 2015]. Currently, one of the major scientific challenges is to experimentally find this critical temperature to prove this theory. The Relativistic Heavy Ion Collider already started a Bean Energy Scan program to search this critical point. In 2019 the program will begin the second phase to optimize and finalize the results obtained before.

The energy necessary to produce QGP could be encountered only in two scenarios in nature: few microseconds after the Big Bang and possibly in the center of super dense stars. These energy and density conditions can be replicated by colliding heavy ions at velocities close to the speed of light. There are several signatures indicating the QGP generation, like jet quenching, parton collectivity and suppression of particle production.

1.4 High Energy Heavy Ion Collisions

Colliding atomic nuclei is a semi-controlled method to unveil the nature inside the nuclear structure. The first step is to smash nuclei together at velocities close to the speed of light in vacuum, trying to “break” them and “liberate” their constituent partons (quarks and gluons). The relativistic velocity makes the nuclei contract (length contraction) making the two beams collide like two disks as observed in the laboratory frame. The collision forms a unique quark-gluon “fireball” of high energy (temperature) and high density that makes possible to reach a point where nearly asymptotically free quarks exist, the QGP phase. Figure 1.3 shows a representation of the evolution of a heavy ion collision.

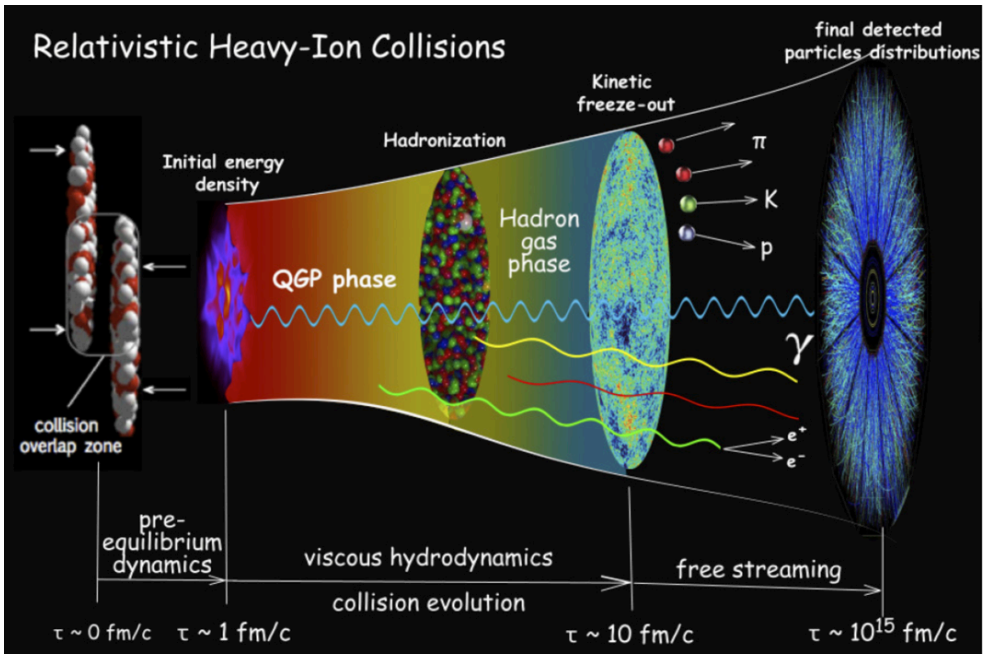

Figure 1.3: Artistic representation of the space-time evolution of a heavy ion collision ("little bang") following similar stages as the "Big Bang" in cosmology [Heinz 2013].

After the collision a brief period of pre-equilibrium conditions is formed before going through the QGP phase. In this phase the parton-parton collisions are very energetic and the environment is favorable for the creation high p_T and/or heavy flavor particles. The QGP phase is supposed to be created immediately after these high p_T or heavy flavor "probes" are produced. The modification in behavior of these probes, relative to elementary nucleon-nucleon collisions, provides valuable information and insights about the nature of the hot partonic matter they have just traversed (see section 1.5). The pressure-driven expansion of the interaction volume increases so temperature and density reduce with time. It is established that approaches based on a Hydrodynamic

picture of the collision can be used to describe the QGP phase after thermal equilibrium is reached [Heinz 2013]. As the system keeps expanding a critical temperature is reached where the "free" quarks and gluons are confined again into hadrons. During this hadronization phase, the density and temperature is still high enough that interactions are dominated by inelastic collisions and hadron production. The system is still expanding and cooling until a *chemical* freeze-out temperature when elastic interactions become dominant and particle production ratios are fixed. Finally, when the system is dilute enough and the hadron mean free path comparable to the system size, the momentum of the hadrons are unchanged; this is called *kinetic* freeze-out.

The initial geometry of the collision, i.e. the impact parameter (b) of the two nuclei determines the bulk features of the interaction like the number of participants (N_{part}), sometimes also called "wounded nucleons" in the collision, that is the total number of nucleons in the overlap region of the two colliding nuclei. The impact parameter determines in a similar way the number of binary (nucleon-nucleon) collisions (N_{bin}). Small values of impact parameter lead to "central" or "head-on" collisions, whereas large b-values to "peripheral" ones [Chaudhuri 2012]. None of these variables (b, N_{part} or N_{bin}) can be directly measured so a model must be introduced in order to determine these quantities. The number of participants is assumed to be proportional to the number of bulk produced particles, the "soft" physics, whereas the binary collisions are more appropriate for the scaling of the more rare, high p_T phenomena. The most common method used to calculate the relation between the particle multiplicity (which can be measured) and these quantities is the Glauber model. This model assumes the

nuclei as a collection of spheres distributed as Saxon-Woods density function, moving in a straight line and colliding directly to each other. Figure 1.4 shows a representation of the collision of two nuclei according to their centrality.

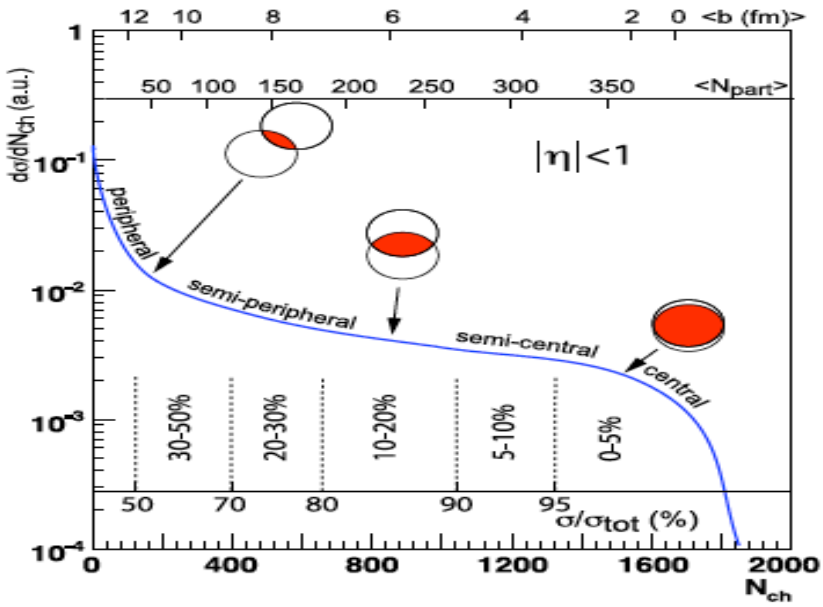

Figure 1.4: Multiplicity distribution of a heavy-ion collision (Au+Au 200 GeV) where its relation to impact parameter (b), participant nucleon (N_{part}) and the different centrality classes are also shown [Chaudhuri 2012].

At this time, there are two particle accelerators in the world capable to reach such relativistic velocities to study the strong interaction in the nucleus. The largest and most powerful particle accelerator in the world is the Large Hadron Collider (LHC) at CERN, in Geneva, Switzerland; where particles travel through a ring of 27 kilometers and collide with center of mass energy of 13 TeV. The other major particle accelerator is the Relativistic Heavy Ion Collider (RHIC) (more in section 2.1).

1.4.1 Jet Quenching and particle suppression

A highly energetic ion collision will produce partons with high transverse momentum that will experience a cascade fragmentation creating a collimated cluster of particles, called *jets*. The jets are mainly produced in pairs traveling in opposite directions but in some cases a third jet might also be produced. The mechanism of jet production and their energy loss in hot nuclear matter was studied since the 90's [Wang, Gyulassy 1992]; however, it is still a subject of debate [Mehtar-Tani et al. 2013]. When the jet-pair is produced close to the boundary of the formed "fireball" in a high-energy nuclear collision, one jet will likely abandon the high-density region of the fireball while the opposite jet will travel through the fireball experiencing energy loss due to its interaction with the medium. This scenario has been tested with p-p, d+Au and Au+Au collisions. The p-p system provides the reference data set and the d+Au system helps us understand cold nuclear matter effects. Figure 1.5 shows early results from the STAR collaboration on jet quenching. The results show that one of the pair jets (the away side) disappears (gets greatly suppressed) only in central Au+Au collisions, which indicates that the vanished jet traveled through an "opaque" region, that is a dense and strongly interacting nuclear matter [Adams et al. 2003].

The properties of the medium can be measured by estimating the energy loss of particles produced in the early stages of the collision. This can be done with light-quark particles like pions or with particles containing heavy flavor (charm and bottom) quarks like the D or B mesons. The energy loss mechanism is occurring either via inelastic scattering (gluon radiation) in the medium (analogous to Bremsstrahlung), or energy loss

by elastic collisions. The exact energy loss mechanism is still a subject of investigation so precise measurements must be performed and compared to theory predictions.

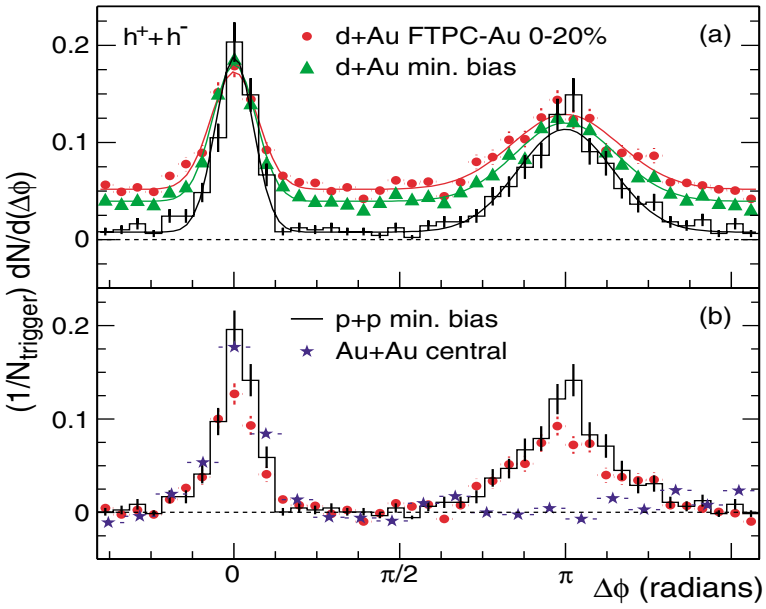

Figure 1.5: Azimuthal correlation of jet in multiple collision scenarios. The top figure shows the efficiency corrected correlation in d+Au central and minimum bias collisions, while the bottom figure shows the azimuthal correlation in central Au+Au compared with p+p. The away side jet is completely suppressed only in Au+Au 200 GeV [Adams et al. 2003].

The nuclear modification factor (R_{AB}) is a relation that quantifies the energy loss of the particle going through the medium. It is the ratio of the number of particles produced in a particular collision system A + B as a function of p_T divided by a reference measurement, usually p + p collisions scaled by the number of binary collision (N_{bin}) to eliminate trivial geometry effects. Equation (1.2) shows the nuclear modification factor relation:

$$R_{AB} = \frac{1}{N_{bin}} \frac{dN_{AB}/dp_T}{dN_{pp}/dp_T} \quad (1.2)$$

In the absence of nuclear effects, in other words, if nuclear collisions are just a mere superposition of elementary p-p collisions, the value of R_{AA} should be one. But if the produced high p_T particles lose large fractions of their energy while they traverse the medium, then the R_{AA} value is expected to be less than one. The exact value of R_{AA} and the specific p_T and particle flavor systematics will provide the needed measurements theorist need to calculate important medium properties. Figure 1.6 shows the R_{AA} estimated by the ALICE and STAR collaborations for D-mesons. The suppression of the particles can be seem for $p_T > 2$ GeV/c, however differences between both measurements are observed at lower momenta (see figure insert).

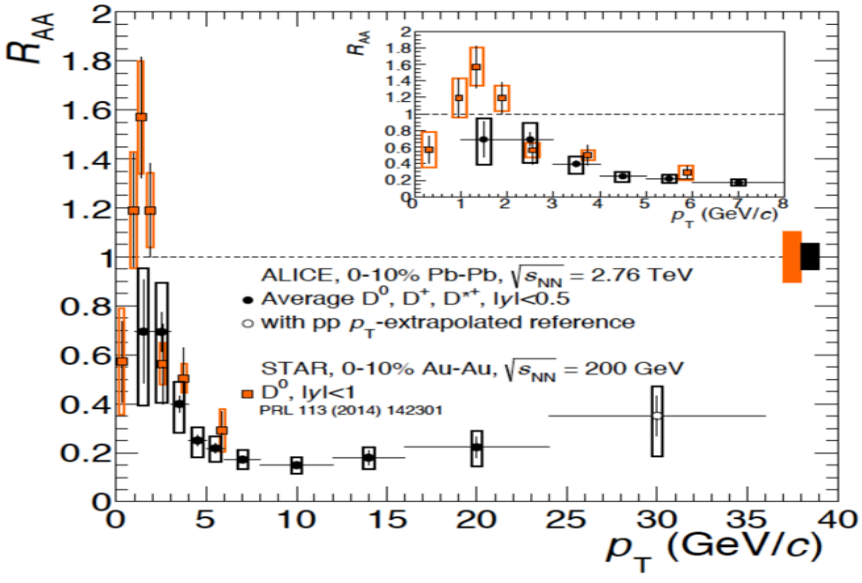

Figure 1.6: Comparison of the nuclear modification factor results of D-mesons for ALICE and STAR collaborations [Adam et al. 2015].

1.5 Heavy flavor quarks

Heavy quarks (charm and bottom) are formed mainly in the early stages of the collision prior to the QGP formation, so they will carry information of the evolution of the system. The temperature of the QGP is lower than the melting temperature necessary to destroy most of the heavy quark bound states. Also, their interaction with the hot and dense QGP will not change the abundance due to their high-energy production threshold because their production is dominated by gluon fusion in hard collisions due to their large masses. Perturbative QCD (pQCD) approaches can quantitatively model this phenomenon [Cacciari, Nason, Vogt 2005].

Open[1] heavy flavor measurements, like D-mesons, are excellent tools to probe and study the QGP. Details of their interaction with the surrounding medium can be studied through energy loss (R_{AA}) and elliptic flow (v_2) measurements thus providing valuable information about the nature of the medium and its degree of thermalization.

Initial studies of D-meson reconstruction using the non-photonic electrons, showed a large magnitude of energy loss that was inconsistent with model assumptions regarding mass hierarchy, since heavy quarks show similar level of suppression of light quarks [Adare et al. 2007]. However, reconstructing the D-mesons from electrons is an indirect method because it is very difficult to separate the electron contribution coming from bottom decays. Precise measurements of directly (using hadronic decay) reconstructed

[1] The term open indicates that the meson contains one heavy quark (or antiquark).

heavy mesons would provide better understanding of the energy loss mechanisms and the properties of QGP.

The D^0 meson is the most feasible charmed particle to study the properties of the QGP. It is relatively abundant in heavy ion collision with a branching ratio of 3.89% in the two-body hadronic decay channel of a kaon and a pion. However, there are still some technical complications to reconstruct the D^0, especially at low momentum where the combinatorial background is large. In this work, we study the Run 2014 data sample of 887M Au+Au events at 200 GeV, using the STAR collaboration detectors at RHIC with the newly installed Heavy Flavor Tracker (chapter 2). We used an algorithm based on the Kalman Filter to reconstruct the D^0 signal, which is not the standard reconstruction method used in STAR collaboration. Multivariate analysis techniques (machine learning) are applied to optimize the significance of the signal obtained (chapter 3). Finally, we present results for D^0 meson p_T spectra and nuclear modification factor for central events and discuss the obtained results with current theory models (chapter 4). Conclusions and future research are discussed in the last chapter.

CHAPTER 2

Experiment Setup

2.1 Relativistic Heavy Ion Collider

The Relativistic Heavy Ion Collider, better known as RHIC, is located at Brookhaven National Laboratory (BNL) about 100 km east of New York City. RHIC started operation in the year 2000 providing an astonishing amount of data to constrain our understanding of QCD theory and providing great discoveries since then.

RHIC is a versatile collider since it can collide heavy ions in a wide variety of species and energy ranges; beside it is the only accelerator in the world able to collide polarized protons, which makes it an excellent facility for spin studies.

The main component of the RHIC complex is a 3.8 kilometers (2.4 miles) ring where ions are accelerated almost to the speed of light and make them collide in up to six intersection points. Several accelerator facilities complement the RHIC ring to provide and initial boost for the colliding ions. The journey of the colliding ions starts at the Electron Beam Ion Source (EBIS), which consist of a quadruple linear accelerator where the negatively charge ions are trapped, so an electron beam ionize them to further release into the next step of the accelerator chain. EBIS provides all stable ion species from deuterons to uranium, including noble gases such as helium and argon. It has reduces operational cost and offers better performance that the previous Tandem van de Graaff accelerators. To collide protons the Linear Accelerator (Linac) is used instead. The

BOOSTER is a pre-acceleration stage with accepts heavy ions from EBIS or protons from 0.2 GeV Linac to inject them to the AGS. The Alternating Gradient Synchrotron (AGS) was one of the major particle accelerators in the world. Currently, the AGS is used as a pre-acceleration of ions or protons before entering RHIC, to provide the final acceleration before collisions occur.

Initially RHIC maintained four physics experiments located at different ring positions. PHOBOS already finished their data taking in 2005 and BRAMHS in 2006. Actually only two major collaborations PHENIX and STAR are still in operation. Figure 2.1 shows an aerial view of the RHIC complex, pointing the major facilities for the acceleration of the ions and the two major experiments location in the RHIC ring.

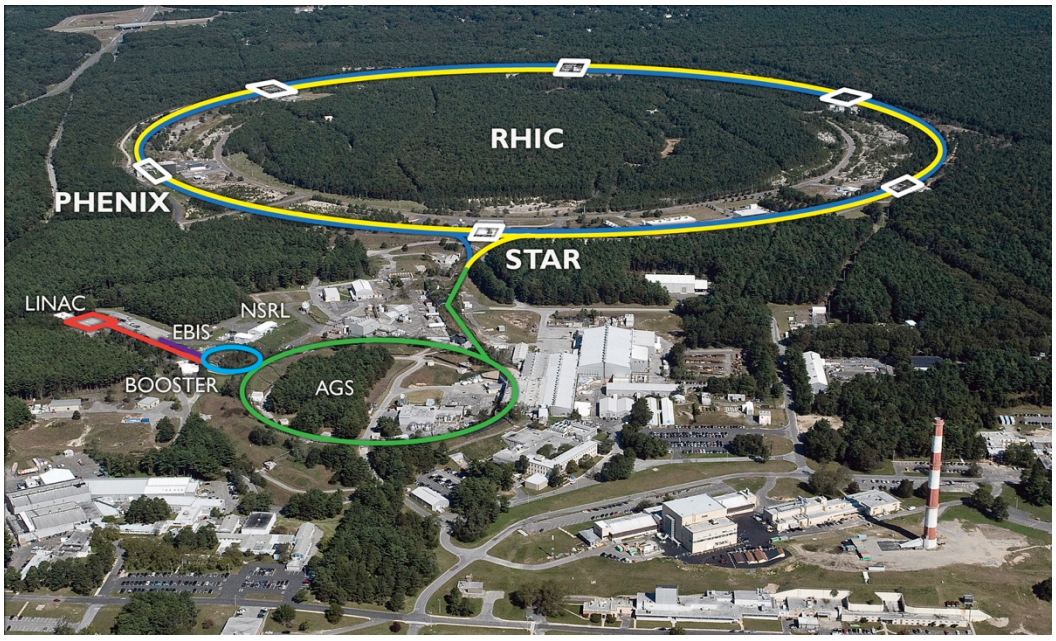

Figure 2.1: Aerial view of the Relativistic Heavy Ion Collider complex at Brookhaven National Laboratory [Walsh 2013].

2.2 STAR Experiment

One of the two larger collaborations at RHIC is the Solenoid Tracker At RHIC or STAR. The conceptual design for STAR collaboration started early 1990 with the first data taking physics run at RHIC in the year 2001. The collaboration is composed of more than 55 institutions around the world, with around 550 collaborators including students, scientists, engineers and technicians; which maintain all the detectors ready for every year data runs at RHIC. All of these collaborators study and analyze the data produced for all the physics to perform [Ackermann et al. 2003].

The goal of STAR is to study the behavior of strong interacting matter at high energy density produced at RHIC collisions. One of the main purposes was to look for signatures of QGP formation. In 2005 after long discussion and studies of the data PHOBOS, BRAMHS, STAR and PHENIX announced the discovery of the QGP making it one of the major advances in physics in the last years [Adams et al. 2005].

The name STAR derives for the room temperature solenoid magnet that reaches a maximum value of 0.5 T to compute the momentum and tracks the produced charged particles. STAR has the capability of measuring identified hadron production over a large solid angle with complete coverage in the azimuthal angle ϕ. It incorporates multiple types of detectors that are capable of providing high precision measurements of tracking, momentum and particle identification. Figure 2.2 shows a diagram of the detectors used by the STAR collaboration. The STAR collaboration has been very successful with major contributions and discoveries in several areas of the field, which complements the physics results of the other major high energy physics experiments.

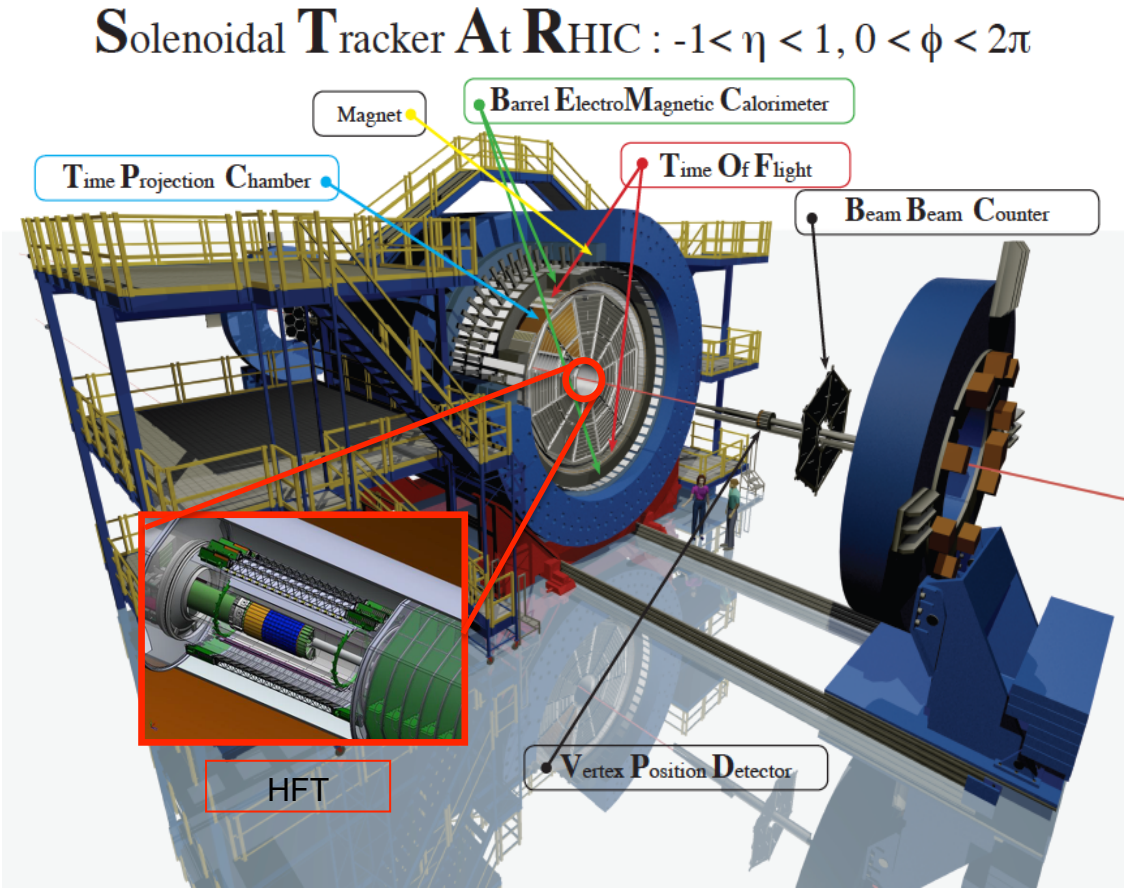

Figure 2.2: Representation of the STAR major detectors at Brookhaven National Laboratory. The Heavy Flavor Tracker (HFT) is the inner vertex detector, commissioned in 2014.

2.3 Time Projection Chamber

The STAR's Time Projection Chamber (TPC) was the largest TPC built for many years until the one commissioned in ALICE at the LHC. The TPC is the main detector of the whole experiment and performs the charged track reconstruction, momentum determination of each reconstructed track and particle identification due the ionization energy lost of the track.

The TPC is a 4.2 meters length, 0.5 and 2 meters inner and outer radius cylinder inside the STAR magnet. It provides full azimuthal coverage ($0<\varphi<2\pi$) and $|\eta| < 1.8$ in pseudorapidity from the interaction point. Figure 2.3 shows a representation of the TPC.

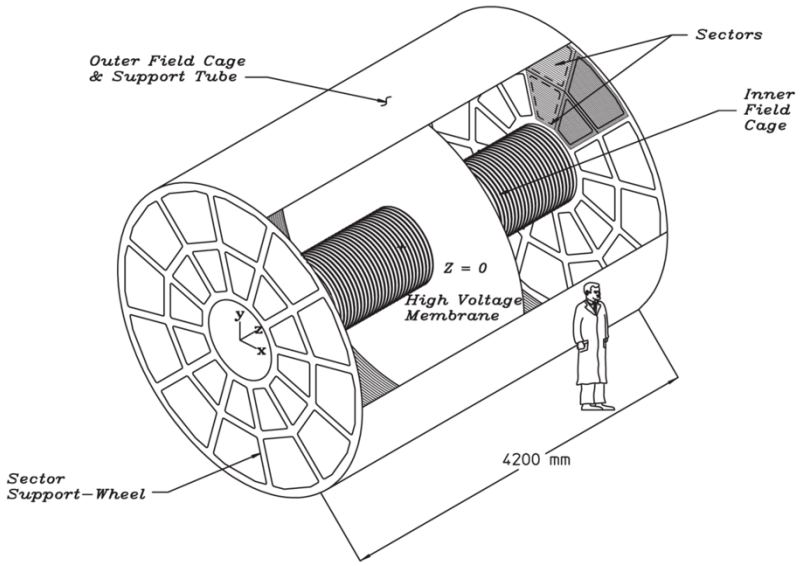

Figure 2.3: Representation of the STAR TPC [Anderson et al. 2003].

The TPC is divided in the middle by a central membrane, which operates at 28kV. The end caps of the TPC are grounded multi-wire proportional chambers (MWPC) to provide a uniform electric field of 135 V/cm. The inner and outer cylinders provide a series of equipotential rings that divide the space between the central membrane and the anode planes into 182 equally spaced segments. The TPC is filled with P10 gas (10% methane, 90% argon) regulated at 2 mbar above atmospheric pressure to minimize any air leakage and prevent contamination.

Charged particles passing through the TPC will ionize the gas. The produced electrons will drift onto the end caps with a drift velocity of 5.45 cm/μs for a total drift-time of up to 40 microseconds. The signal is recorded by a series of readout pads, located within the TPC volume, for the posterior amplification and digitalization. These readout pads are located in 12 sectors azimuthally (each covering $\pi/6$), and each sector contains 45 pad-rows, which measure the total deposited energy in time. Furthermore, the pads are divided in inner and outer section since the track density is bigger closer to the interaction point [Anderson et al. 2003]. An upgraded TPC inner section will be installed in 2018 and expected to start data taking in 2019. The new inner section will increase the number of rows from 13 to 40 allowing extending the actual coverage. Also the current inner sector has suffered intense radiation during its 15 years of use. The complete replacement of the inner pads with an updated readout system will allow better resolution and increase slightly the coverage of the TPC.

2.4 Time Of Flight detector

STAR has an incredible particle identification (PID) capability. The TPC is the main detector for particle identification by measuring the energy loss of the passing particle. Beside the TPC, STAR has a Time Of Flight (TOF) detector also used for particle identification. As its name suggests, the particle identification is done by measuring the time of the particle from the interaction vertex (its initial position) to the point of the detector (the track length). The speed of the particle is computed at that point with a precision of 85 ps, so the mass can be easily calculated using the momentum obtained by the TPC. The TOF is located outside the TPC at radius ~225 cm from the

interaction point, covering $|\eta| < 0.9$ and full azimuthal angle. It consists of Multi-gap Resistive Plate Chamber (MRPC) technology, which collects the current produced by the electron avalanche in the ionized gas due to the passing particles. The TOF system increases the particle identification capabilities. It extends kaon-pion separation up to 1.6 GeV/c and proton separation up to 2.8 GeV/c. STAR particle identification efficiency increase ~95% by combining TOF and the dE/dx from the TPC [Llope 2003].

2.5 Vertex Position Detector

The Vertex Position Detector or VPD is the main event-vertex trigger detector used for heavy ion collisions since it is optimal for recording minimum bias events. The VPD consists of two set of photomultipliers located at 570 cm of the interaction point, at each side of the beam pipe, and covering a region of $4.24 < |\eta| < 5.1$. The vertex position is calculated by measuring the difference in time of the signal that arrives at each east and west detectors. This detector has very good time resolution, which results in a vertex position resolution of 1-3 cm as determined offline [Llope 2014].

2.6 Heavy Flavor Tracker

In relativistic heavy ion collisions, the relatively low abundance of heavy quarks and their short lifetimes makes them difficult to distinguish from the event vertex and the combinatorial background; therefore, there is a need for a high precision vertex detector to reconstruct their decay particles. In 2014 a newly micro vertex detector was installed in the STAR experiment at Brookhaven National Lab. The Heavy Flavor Tracker (HFT)

was designed to perform direct topological reconstruction of the weak decays of heavy flavor particles [Margetis 2009].

The HFT is not the first vertex detector in STAR. From 2003 until 2009, the Silicon Vertex Tracker (SVT) was commissioned to improve the tracking and strange and multi-strange particle identification capabilities of the TPC. The design of the SVT (amount of scattering material, distance from the interaction point, i.e. track pointing resolution) was not optimized for charmed meson reconstruction so an attempt to identify and reconstruct charmed mesons with it was not successful [Joseph 2011]. The HFT uses Monolithic Active Pixel Sensor technology (MAPS), which can be made very thin thus reducing multiple scattering. This is the first time in collider experiments that this technology is used [Contin 2015]. Figure 2.4 shows a simulation performed in this work, to estimate the pointing resolution of the HFT for different particle species.

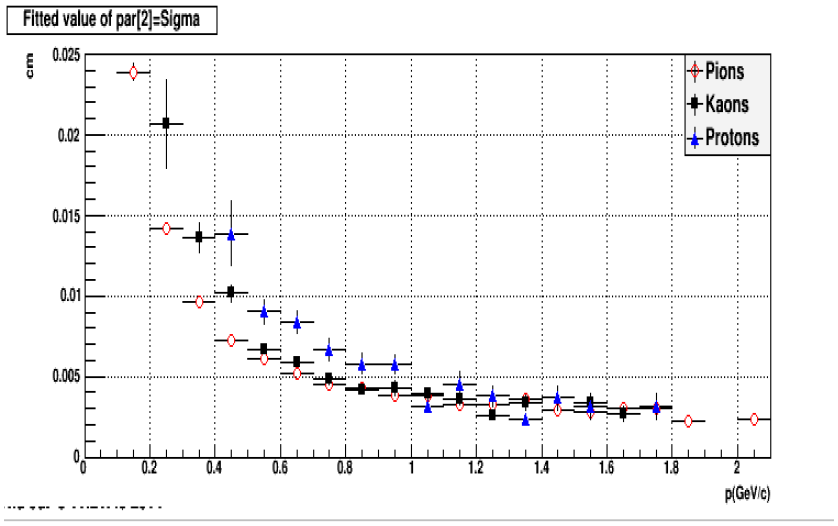

Figure 2.4: Pointing resolution in the z-axis of minimum bias Au+Au simulation performed with the HFT for pions (red), kaons (black) and protons (blue) with respect to the transverse momentum.

The HFT improves STAR track pointing resolution from a few millimeters to ~30 microns for 1 GeV/c pions, allowing direct reconstruction of short lifetime particles. The reported value for pointing resolution of 0.750 MeV kaons in Run 2014 is about 45 microns, which is one of the best track pointing resolutions ever achieved in a collider experiment, in both r-phi and z directions [Contin 2015].

The HFT is composed of three sub-detectors with different technologies to complement each other and obtain the required performance. Figure 2.5 shows a representation of the three sub detectors.

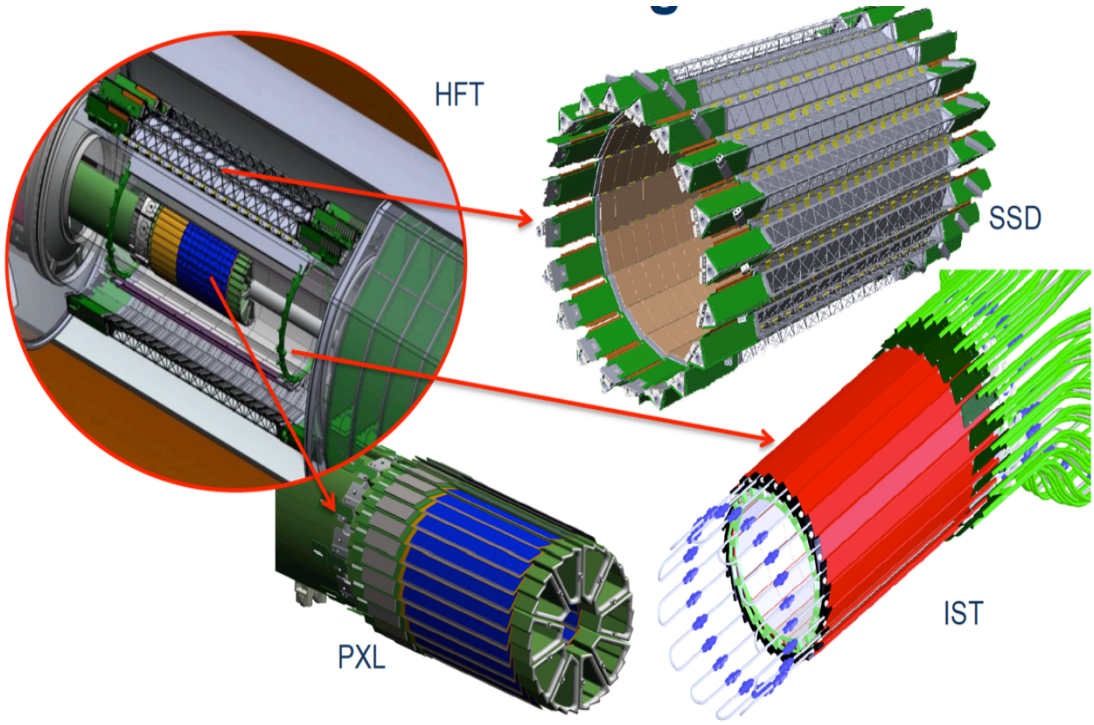

Figure 2.5: Representation of the three sub detectors that conform the HFT: the PIXEL, IST and SSD [Contin 2015].

2.6.1 The Silicon Strip Detector

The Silicon Strip Detector (SSD) is a double-sided strip detector already in STAR since 2004, but the electronics was upgraded for the HFT program. Figure 2.6 shows a picture of the detector before installation.

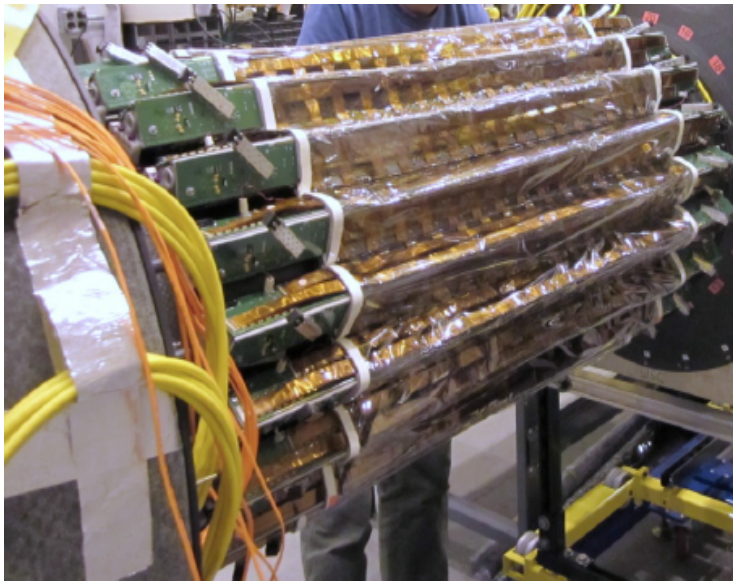

Figure 2.6: Picture of the SSD assembled and mounted on its support structure.

The SSD is located at 22.3 cm radius from the interaction point being the fourth and outer layer of the HFT. It has full azimuthal coverage and pseudorapidity coverage $\sim|\eta| < 1.2$. The SSD consists of 20 carbon fiber ladders of approximately one meter each surrounding the interaction point. This sub detector is mounted into a carbon fiber frame. Each ladder is tilted ~11 degrees in their radial axis, allowing small overlap of active area for better performance; this overlap is also used for alignment purposes. Every ladder has 16 wafers of 7.45 cm x 4.35 cm, 300 microns thick and an ADC board at one end, along

the beam line. A wafer uses double-sided silicon strip technology with 768 strips per side. The silicon strip technology relies on reversely biased P/N junctions. Electron-hole pairs are generated, when a particle goes through the detector, allowing the electronics to record the event. The cooling system is airflow based [Bouvier 2005].

2.6.2 Intermediate Strip Detector

The Intermediate Silicon Tracker (IST) is a single-sided silicon pad sensor technology located at 14 cm radius from the interaction point. The IST consists of 24 carbon fiber ladders of 50 cm long. Each ladder has 6 silicon pad sensors of 3.8 cm x 7.5 cm, readout electronic chip and aluminum cooling tubes. The cooling system for this detector is liquid coolant. The main propose for both SSD and IST is to guide the tracking system from the TPC to the Pixel [Wang 2014]. Figure 2.7 shows a picture.

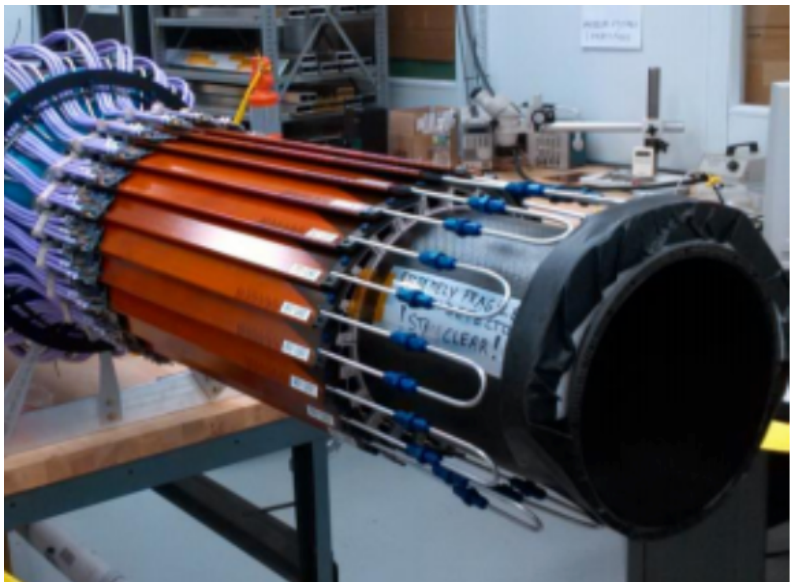

Figure 2.7: Picture of the assembled IST on its support structure. One can see the liquid cooling pipes as well as the readout cables.

2.6.3 Pixel

The most inner layer of the HFT is called Pixel (PXL). It consists of two layers, at 8 cm and 2.8 cm, of the new Monolithic Active Pixel Sensors (MAPS) technology [Hu-Guo et al. 2010]. The PXL has 10 sectors of carbon fiber tubes, which a particular shape designed to accommodate 4 ladders per sector; one ladder at 2.8 cm and the other three at 8 cm from the interaction point. Each ladder has an active length of 20 cm with 10 MAPS sensors. Each sensor of 2 cm x 2 cm accommodates 928 x 960 pixels to allow an incredible hit resolution of 6.3 microns. Figure 2.8 show a picture of half of the detector before installation.

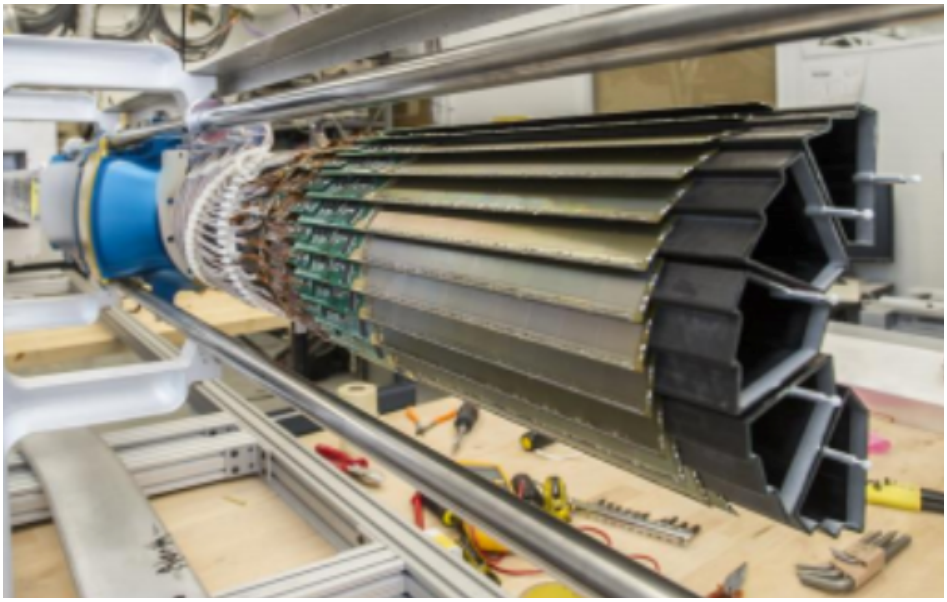

Figure 2.8: Picture of one half of the Pixel detector showing its five trapezoidal sectors. Each sector supports four ladders, three outside (visible) and an inner one. Also shown is the Pixel support and insertion mechanism.

The MAPS sensors are based on commercial complementary metal–oxide–semiconductor (CMOS) technology (it is used as an image sensor in a camera for example), where the signal processing is integrated in the same silicon sensor. The charge collection is mainly through thermal diffused electrons in a low-doped epitaxial layer and collected in a large electric field region [Qiu 2014]. This new technology reduces the collection time and yields a good signal to noise ratio. Each CMOS pixel size has been reduced to improve the radiation tolerance. These sensors were thinned down to ~50 microns to reduce the material budget in this sub detector, to minimize multiple Coulomb scattering and to be able to reach the desired resolution. Figure 2.9 shows a representation of the pointing resolutions achieved in each layer of the HFT from a TPC track. Also the supporting frame material has been designed to control the vibration and also minimize multiple scattering, but being strong and practical to allow fully replacement of the PXL in 12 hours. Besides the PXL is air-cooled which minimizes the material utilization [Contin 2015]. Certainly the PXL is the most important sub detector of the HFT since it provides the required pointing resolution to topologically reconstruct short life time particle like charm mesons. A disadvantage of the detector is that it has a slow readout and records all hits that take place within 186 μs of the reaction of interest, Therefore it would not be possible to work alone, since its proximity to the interaction point and the about 4 additional minimum bias events creates a highly dense hit environment that will make impossible an accurate tracking reconstruction of the decay particles. The PXL relies on hits from either the IST or SSD to connect the tracks from the TPC (which is the main tracking detector) to provide the excellent resolution.

The results from the STAR collaboration using MAPS technology look very promising. The ALICE collaboration at LHC is planning to use this technology in their upcoming upgrade inner detector the Inner Tracking System or ITS [Senyukov 2013].

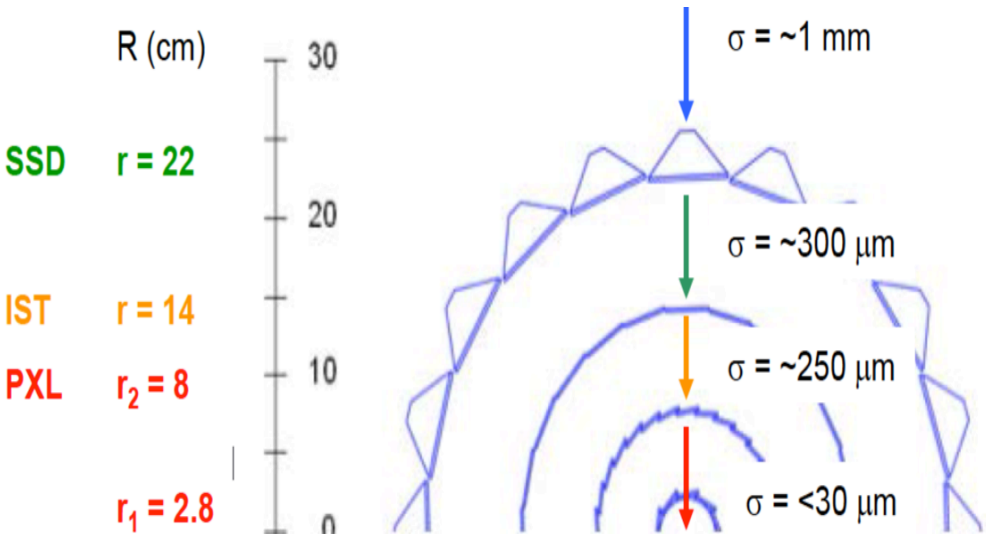

Figure 2.9: Estimated pointing resolution of each layer of the HFT [Contin 2015].

2.7 Other detectors in STAR

STAR is equipped with several other detectors designed for different physics measurements. Next, a summary of some major detectors available during data taken in 2014, but not used for this work, is shown.

- Electromagnetic calorimeters: composed by the barrel (BEMC) and the endcap (EEMC) calorimeter enclosing the TPC. BEMC is located above TOF, with an acceptance of $|\eta| < 1.0$ and 2π in azimuth, matching the acceptance of the TPC. The EEMC covers $1 < \eta < 2$. As calorimeters, the main objects of study are electrons.

These systems help with the identification of the electrons since they measure the size of the shower developed by the particle passing through the calorimeter [Beddo et al. 2003]. Electrons would deposit most of their energy in the calorimeters.

- Trigger system: the bunch crossing time frequency at RHIC is 10 MHz, being around one thousand times larger that the read out capability of most detectors. The TPC records hits over 40 μs thus will cause many Pile-Up vertices to be recorded in each event. The trigger system is divided in four levels that bond the information from the fast detectors like VPD, Zero Degree Calorimeter (ZDC) and Bean-Bean-Counter (BBC), to the slow detectors like the TPC. These slow detectors reduce the rate by five orders of magnitude. The ZDC and BBC are detectors located each side of the beam line, to estimate the vertex position. The principle is the same as explained for the VPD, but the technology used if different. As indicated by its name, the ZDC is a calorimeter, and the BBC use scintillators [Bieser et al. 2003].
- Muon Telescope Detector (MTD): recently added to STAR in 2014, the main purpose of the MTD is to provide accurate measurements of di-muon decays over a wide range of transverse momentum in order to distinguish heavy flavor correlations from initial lepton pair production. The technology used in the MTD is MRPC as in TOF [Yang et al. 2014].

CHAPTER 3

Data Analysis

3.1 Event selection

The installation of the HFT (and MTD) in 2014 came with a three-year program. The priority for STAR in the first year was to record more than one billion minimum bias events of Au + Au collisions at center of mass energy 200 GeV per nucleon, needed for the heavy flavor program. More specifically, the physics goals from the first year dataset were the measurement of charm flow and charm nuclear modification (R_{AA} and R_{CP}) factor. The plan for year-2 of this program (Run 2015) was the recording of about a billion proton-proton 200 GeV events for reference data plus smaller samples of proton-Nucleus (p-Au and p-Al) collisions at 200 GeV for cold nuclear matter studies. The third year was planned for a longer Au+Au 200 GeV run yielding about 2 billion events for detailed charmed studies and a first attempt at bottom mesons and the Λ_C baryon.

Both the HFT and MTD were fully installed in 2014 to accomplish their physics goals. After more than 15 weeks of running, the goal in number of events was achieved and around 1.2 billion events are suitable for data analysis. About 20% extra events were recorded in order to compensate for lost acceptance due to some dead sensors in HFT. Minimum bias trigger is required for this type of analysis since very peripheral events are difficult to trigger, so as the name suggests, minimum bias will trigger almost all hadronic collision events. The VPD allows to trigger on events where the primary vertex was within the acceptance of the PXL detector.

The first stage in offline processing the raw data from the detectors is to execute a reconstruction algorithm, exclusive to STAR, called Big Full Chain (BFC). The name indicates the possibility of setting options to the output readable data file. For example, some detectors can be turned off for a particular analysis, to save memory and running time in the computer. In BFC the raw data are properly calibrated and then cluster/hit and track reconstruction algorithms reconstruct the PID, momentum etc. of the produced particles together with the event vertex position. STAR software and computing team, always release an official production of the data taken each year for all physics analyses. Several output files could be produced by the BFC. For physics analysis this output file is called MuDst (from the prefix "micro" or "μ", and Dst [Data Summary Tapes]), and contains all relevant event information except hit information. The BFC output file format is in ROOT format since STAR uses the ROOT framework as its reconstruction and analysis backbone. In the MuDst, the data about the event, tracks etc is organized in a ROOT tree structure, so is easy to operate the information required for the analysis.

The LBNL STAR group further compressed the official production by removing redundant information, to save disk space and expedite processing times. The PicoDst (prefix pico) files are a smaller and optimized version of the MuDst, with information required mostly for the heavy flavor program; acceptance is optimized for some detectors (HFT primarily), so bad quality tracks and events were rejected. Studies made by the same group showed that the loss in performance of the analysis is marginal but the computational and storage advantages are substantial. Last step to perform the physics

analysis is to extract the track parameters from the PicoDst files, with an analysis code developed in this study for charm meson reconstruction in the two-body decay channel.

Almost all PicoDst production at LBNL is used in this analysis; from approximately 1.2 billion events in the total production, 887 million events are used. Some event cuts are applied to the PicoDst files to maximize the quality of the selected events in order to ensure a good reconstruction by the tracking algorithm and constrain these events to be within the acceptance of the HFT. The cuts required for this analysis are standard for this type of analysis for the Run 2014 data in STAR:

- Vertex Z position $|Vz| < 6$ cm. To guarantee hits in the HFT acceptance for central region tracks.
- $|Vz - VPD| < 3$ cm. This is a request that the tracking-based reconstructed event vertex position along the beam direction (V_Z) is within 3 cm from the VPD triggered position.
- RefMult >10. RefMult is the track multiplicity associated with the primary vertex within pseudorapidity[1] $|\eta| < 1$. This allows a minimum number of tracks for a correct primary vertex determination.

---

[1] Pseudorapidity (η) is an approximation of Rapidity (y) using the angle of a particle relative to the beam axis: $y=0.2\ln[(E+p_Z)/(E-p_Z)]$ and $\eta= -\ln[\tan(\theta/2)]$. It can be shown that rapidity and pseudorapidity are equal for massless particles or at high momenta. Rapidity is a kind of relativistic velocity with its intervals being Lorentz invariant.

Figures 3.1 shows the vertex position used in the analysis, estimated by the BFC using the reconstructed tracks. The left-panel shows the beam (z) coordinate distribution. We observe that the peak position of the distribution is shifted by about a centimeter to negative z-values. The right-panel shows the transverse (x-y) position of the event vertex, i.e. the beam cross section. Note the logarithmic scale in the density (z) dimension. We observe that the beam line was shifted by about 2 mm in both the x and y direction.

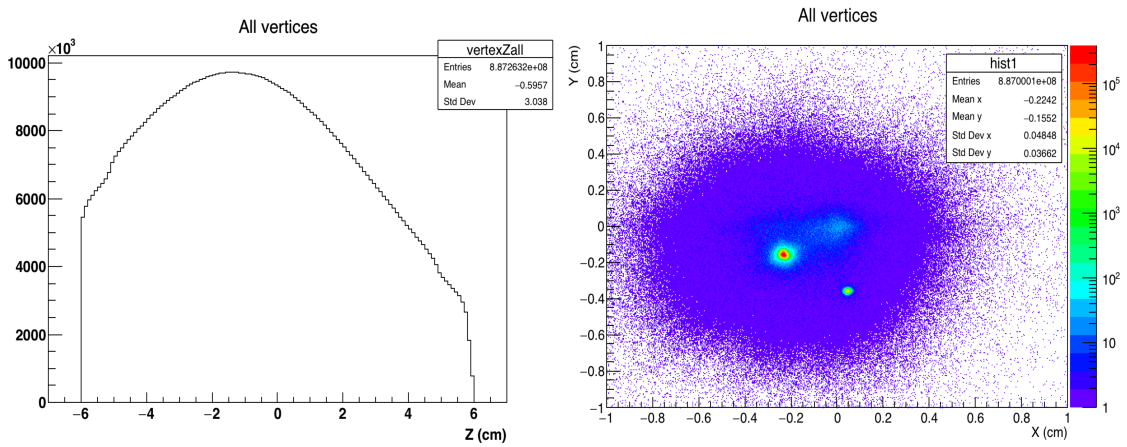

Figure 3.1: Vertex Z position (left), and vertex X and Y position (right), calculated by the reconstruction algorithm used for this analysis.

Figures 3.2 shows the correlation between the z-vertex position obtained from tracking (in offline reconstruction) and the triggered value given by the VPD detector. A good (diagonal) correlation between the two is shown demonstrating the power of VPD is event vertex selection. The primary vertex reconstruction is performed in offline reconstruction (BFC) with tracking information using a Minuit-based algorithm to estimate the full 3D position of the primary vertex [Reed, 2010]. Since fitting algorithms

are sensitive to initial (seed) values and in order to avoid local minima, a z-position scan is first performed and seed vertex candidates are formed. Typically the primary vertex position is estimated by looking (iteratively) for the space point that minimizes the distance of closed approach (DCA) of all the reconstructed tracks after outlier-track rejection. This method is used in analysis of heavy ion collisions since it is a high multiplicity environment therefore there is enough statistics for the vertex estimation. Several vertices along the z-axis will be produced due to pileup events (un-triggered events that happen within the readout time frame of the TPC or PXL detector, more frequent in the high-luminosity p-p environment). All vertices are first reconstructed and then ranked according to certain criteria for their probability of being the triggered event.

The set of all reconstructed tracks in the TPC (with or without HFT hits) is called *Global Tracks*. Global tracks within 3 cm from the primary vertex are refitted with the vertex space point on them and the ones successfully fitted become *Primary Tracks*, which are the tracks originated from the event vertex.

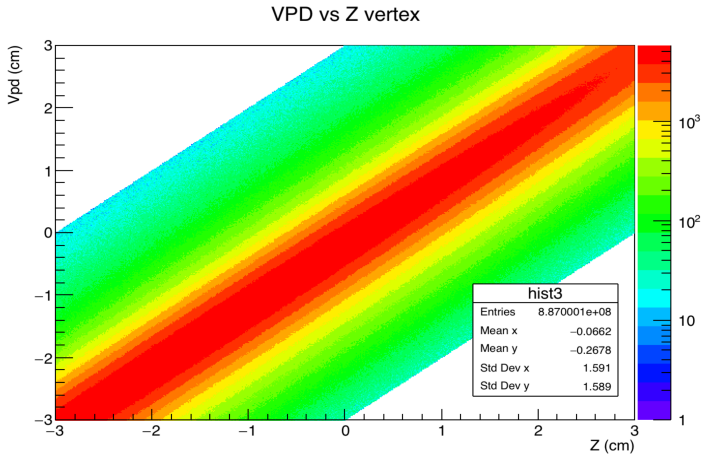

Figure 3.2: Correlation between the track fitted vertex Z position and the triggered position derived from VPD detector.

In our analysis, a Kalman Filter method was used to calculate the primary vertex (see section 3.4.2 for more details). Although PicoDst files already include the primary vertex of the event, the Kalman Filter method performance is better that the Minuit method for primary vertex estimation, as shown by previous studies and studies from other groups in STAR. Figure 3.3 shows a comparison of a small sample of Run 2014 production comparing results of the primary vertex of Kalman Filter vertex finder (KFV) minus VPD (black curve) and Minuit minus VPD (red curve). The KFV is finding about 15% more vertices and it shows a better rms. Several internal STAR studies are also evaluating the efficiency of the Kalman Filter vertex finder for Au+Au collisions and other colliding species (p+p collisions have a different vertex reconstruction algorithm), so this algorithm can be use as the official vertex reconstruction method in STAR.

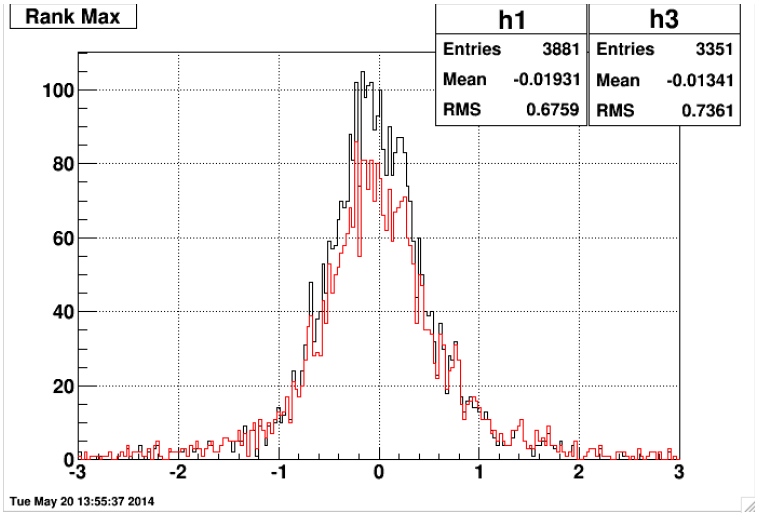

Figure 3.3: Comparison of the primary vertex with Kalman Filter minus VPD (black) and Minuit minus VPD (red).

3.2 Track selection

The track selection is standard for this type of analysis in STAR. The purpose is to ensure good quality of the reconstructed tracks used for the analysis. The track quality selection cuts are the following:

- The number of TPC hits used to fit a track should be greater than 20.
- The ratio of TPC hits on the track divided by maximum possible number of TPC hits for the given track geometry should be greater than 0.52. This is to avoid considering both segments of split tracks.
- Number of TPC hits used in the dE/dx PID calculation greater than 10.
- Transverse momentum of the track greater than 0.3 GeV/c to minimize ghosting and ensure good reconstruction quality.
- Tracks must have at least one hit in each of the two PXL layers and one hit in the IST layer.
- Track DCA to primary vertex less than 0.04 cm.

3.3 Particle identification

The TPC and TOF are the detectors used for hadron (pion and kaon in our case) particle identification. The TPC is the main tracking detector and also the main particle identification detector. The TPC measures the energy loss (dE/dx) due to the ionization of the charged particles passing through the TPC gas. Each particle species will show a different energy loss rate with respect to its momentum. This difference in dE/dx is used to distinguish particles with momentum less than ~0.6 GeV/c, using only the TPC. STAR used the Bichsel function to obtain the identity of the measured track [Bichsel 2006]. The

identification is done by applying a cut on the standard deviation from the centroid of the measured dE/dx per track. The standard deviation relation is given by the equation (3.1):

$$\sigma_{particle} = \ln\left[\frac{dE/dx_{measured}}{dE/dx_{expected}}\right]\frac{\sqrt{N}}{A} \tag{3.1}$$

where N is the number of dE/dx points and A is known as the fractional resolution for tracks with a single dE/dx point [Bichsel 2006]. Figure 3.4 shows the result for the dE/dx of all the particles that pass the tracks cuts, for a portion of the statistics available.

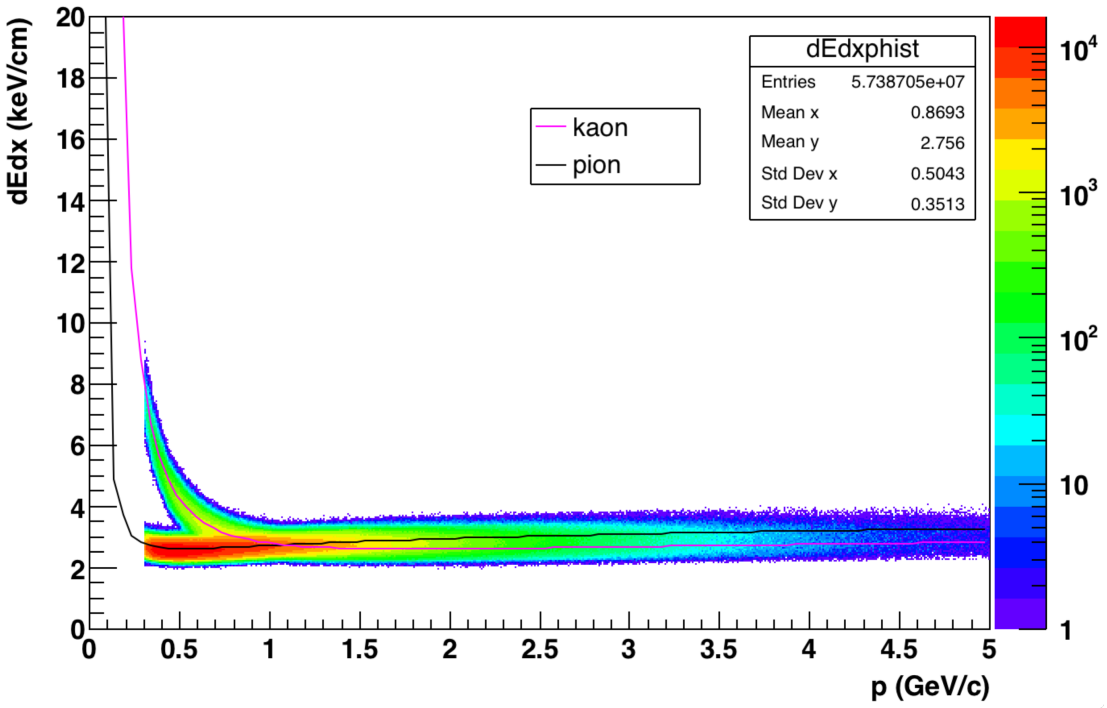

Figure 3.4: Energy loss, dE/dx, in the TPC for a sample of particles from this analysis. Only particles compatible with the pion (lower band) or kaon (upper band) hypothesis are shown here. For momenta greater than ~0.6 GeV/c the bands merge and it is not possible to distinguish the particles.

For this study, only kaons and pions need to be identified. The cut used for both kaons and pions is 2 sigmas from the expected value. The lines correspond to the expected result for pion (black) and kaons (magenta). Protons are not used in this analysis, so the proton band in not shown in the previous figure. All of the tracks have TPC information so the dE/dx for all the tracks is available.

TOF information might not always be present due acceptance and efficiency of this detector. Thence, TOF is used for particle identification when its information is available. TOF increase the pion-kaon band separation to 1.6 GeV/c. A combined TPC and TOF criteria is needed to identify a particle if TOF is available but if there is no TOF information, only the TPC is used. The fraction of the velocity with respect to the speed of light β is calculated using the time of flight of the track (obtained with TOF) and the length of the track. This value is compared with the expected value for a specific particle and the momentum (p) from the TPC, following the equation (3.2):

$$\frac{1}{\Delta\beta} = \left| \frac{1}{\beta_{TOF}} - \frac{1}{\beta_{particle}} \right| = \left| \frac{1}{\beta_{TOF}} - \sqrt{\frac{m^2_{particle}}{p^2_{TPC}} + 1} \right| \tag{3.2}$$

For both kaons and pions the acceptance criteria used in this analysis is common in STAR also; both pions and kaons are required to have $\Delta\beta^{-1} < 0.03$. Figure 3.5 show the mass squared calculated with the TOF information, for kaons and pions. The proton band should be above the kaons but protons are removed to reduce background.

The TOF can separate the pion and kaon bands up to ~1.6 GeV/c, above this value, it is very difficult to correctly identify the particles. Usually tracks can be identified as two or more different particles at the same time, if the track is in an overlap

region between particle species; this increases the combinatorial background. In this analysis, each track gets a unique PID assignment, so the track is identified either as a kaon or a pion, whichever $\Delta\beta^{-1}$ hypothesis is closer to the β^{-1} of the particle.

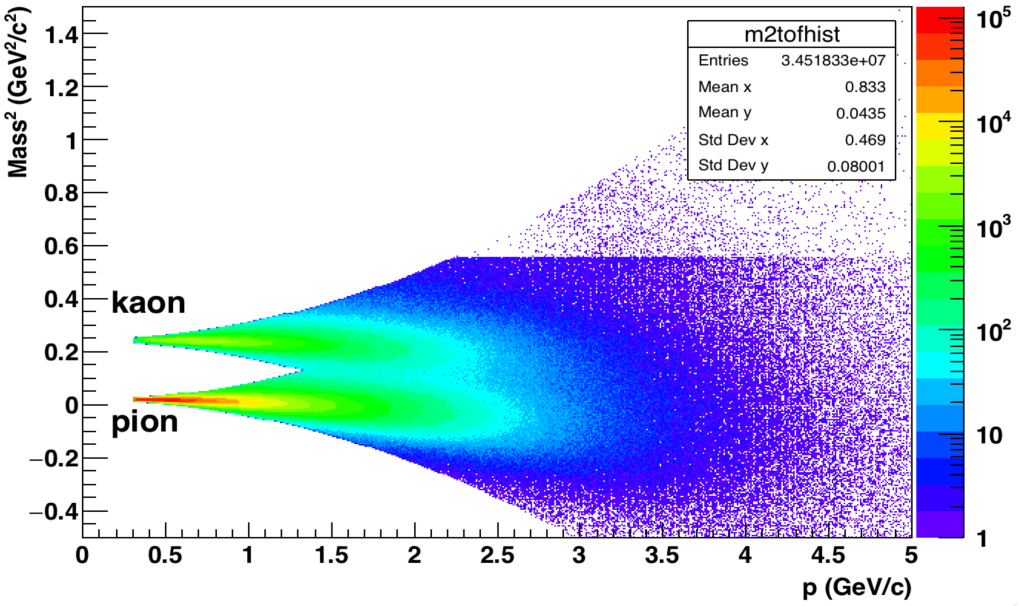

Figure 3.5: Mass squared calculated with the TOF information, for kaons (top band) and pions (bottom band).

An initial attempt to separate kaons and pions when TOF information was not available (~40% of the statistics due to TOF acceptance), using only TPC dE/dx information by using multivariate methods was performed. The training was done using a simulation since the correct identity of a track is known. The classifier with the best performance was BDT (section 3.7 will explain details about this method). The variables used for the training are dE/dx, momentum, charge and the sigma values for kaons, pions, protons and electrons. However this method was not used in the final analysis due to its poor performance separating the particles when the σ_{TPC} overlaps, as evaluated through

MC simulations. Figure 3.6 shows the result for the classifier response to separate kaons and pions. From the figure, it can be seen that the kaon (red) and pion (black) lines do not show any separation; ideally there should be a threshold value in the x-axis where the kaons and pions could be separated. By the time of this study, STAR simulation framework did not include TOF hits so this method could not be used when TOF hits are available.

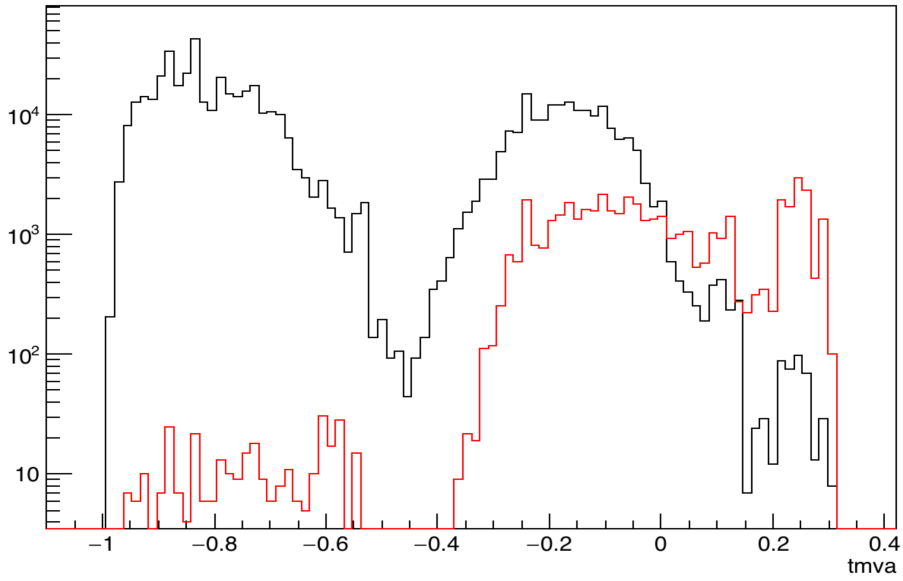

Figure 3.6: Classifier response to separate pions (black) and kaons (red). The x-axis represents the value of the classifier. No useful separation between the particles was achieved.

The separation for kaons and pions using this multivariate method is not very efficient since it recovers only 10% of the kaons. To maintain the unique PID per track, all tracks in the overlap region of pions and kaons were identified as pions. A contamination study is discussed in section 4.

3.4 D^0 Reconstruction

The reconstruction of the D^0 meson and its charge conjugate starts after the identification of kaons and pions by performing a secondary (decay) vertex search in track combinations. Since charmed mesons decay in a short time ($c\tau \sim 120$ microns), the reconstruction has to be done from the daughter particles. The sum of the 4-momentum vector for each pion and kaon per event must generate the invariant mass of the D^0, when opposite charges of the tracks is required; most of this addition will be background. By combining same charge tracks, the background should be reproduced since this is the combination of two random tracks with no physical implication. Other methods to reproduce the background are to mix daughter particles of different events (mixed event), and rotated the momentum vector of one of the particles in the 4-momentum addition (rotated background). These two methods were not used for this study because they did not reproduce the background correctly and/or take more computational time.

The tracking algorithm will reconstruct the track of the particles as a helix. However, the mother particle analyzed (D^0 in this study) has to be done by combining the daughter particles in a systematic way, so the background does not overcome the signal. Two methods are described in the following sections.

3.4.1 Helix Swimming

The standard reconstruction algorithm used in most heavy ion collision experiments [Adamczyk et al. 2014, Adam et al. 2015], is based on a helix swimming of the reconstructed tracks. When a short lifetime particle is produced in a collision and further decays, the daughter particles will travel into the detectors following a specific

path. If these daughter particles are charged, they will follow curved trajectories or helices due to the magnetic field that converges to each other in the point where the mother particle decayed. This point is called secondary vertex since the primary vertex is where the collision occurred. In an ideal scenario, these helices will converge exactly in the same point; however, due to limited tracking resolution of the detectors, these helices will be shifted from the secondary vertex and might never cross each other. The Helix swimming method consists in finding the distance of closest approach (DCA) between the helices and defining the midpoint as the secondary vertex. Once the secondary vertex is identified, topological and kinematic conditions must be required to identify the particle decay and to reduce the combinatorial background. Figure 3.7 shows a representation of the D^0 decay with the pion and kaon tracks.

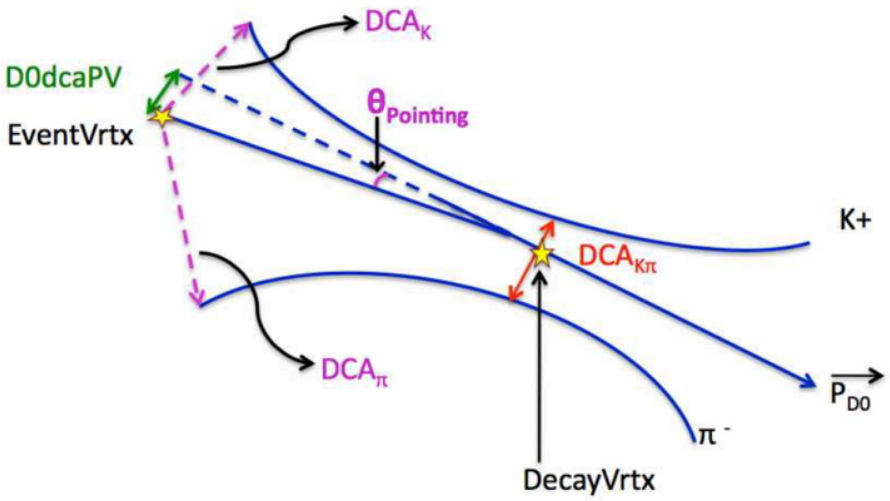

Figure 3.7: Diagram of the helix representation of a D^0 decay [Joseph 2011].

For D^0 reconstruction, some of the topological decay variables (cuts) required are:

- DCA from the pion track to the primary vertex to reject primary tracks.
- DCA from the kaon track to the primary vertex to reject primary tracks.
- DCA of reconstructed D^0 track to the primary vertex.
- DCA between the two daughter tracks.
- The decay length of D^0.
- Pointing angle of the reconstructed D^0 and the decay length direction.

Besides topological cuts, some constraints in the momentum of each daughter track might be required, because of the high number of low momentum tracks, not necessary coming from D^0 decays, that contribute greatly to the background and rapidly overcome the signal.

Helix swimming has been proven to be a simple, computational fast and reliable method for D^0 reconstruction. With the introduction of the HFT in STAR, the pointing resolution of the DCA improves considerably (by about two orders of magnitude relative to TPC alone).

3.4.2 Reconstruction Algorithms based on Kalman Filter

The Kalman Filter is one of the most common methods used to clean noisy signals in several areas such as electronics, telecommunications, trajectory optimization, econometric, etc. The method relies on measurements done over time, which constrains noise and other inaccuracies, to optimize a set of variables that cancel these inaccuracies. Rudolf Kalman developed the method focusing in signal communication [Kalman 1960]. The method compares the system theoretical model (e.g. a control signal or the equations

of motion of the system, etc.) with the measured values in time. A set of parameters, computed from the difference between the expected value (the model) and the measured value, will weight the measurement in order to minimize those differences. These weights are calculated via covariance matrix of the errors of the measurements, and are updated with each measurement. The main difference between using Kalman or take the average of the noisy signal is that Kalman uses the last updates weight to correct the actual measurement while averaging must be done over set of measurements which will take more computational time. The Kalman Gain is the formal expression to refer to the weights.

The current standard tracking method was implemented few years after the commissioning of the STAR experiment. Kalman Filter was the chosen fitting algorithm due its performance in tracking efficiency and computational resources. The track model is defined to be a helix trajectory (charged particle) with some consideration on energy loss and Coulomb scattering, going through the STAR magnetic field and material. The tracking starts by doing an inward tracking to the detectors (going into the beam pipe), since is a low hit density environment compared to the inner layers. A seed track is initialized before working the Kalman machinery. This seed track is a short length track in the outer layers but needed to have enough information for a good estimation of the final track parameters. After initialization of the track Kalman Filter calculate the position of the hit in the next layer and match it with the corresponding hit, within error margins. If the track does not have a matching hit in one layer, this layer is skipped. Once a hit is matched with a track the Kalman parameters are updated and the process

continues until the last innermost layer of the sub-detectors. Once the inward tracking is complete, a new tracking pass is performed but this time going outward, however most of the hits are already found so this pass basically updates the track parameters [ITTF 2003].

The Kalman Filter is the most common fitting and filtering method for particle reconstruction but in STAR decay vertex reconstruction is traditionally done using the helix swimming approach. In our analysis, the D^0 reconstruction is done using an algorithm based on the Kalman Filter, called KFParticle. This package we used was originally designed for CBM experiment, however it was rapidly adapted to ALICE (CERN) experiment since the algorithm only depend on the parameters obtained in the tracking, so it is independent of the geometry of the experiment [Gorbunov, Kisel 2007]. The KFParticle package uses the full error (covariance) matrix for each track, so a more complete approach is performed to the secondary vertex reconstruction.

KFParticle provide several parameters of the reconstructed particle, like momentum, decay length and life time, also provides errors and fit quality estimates (deviations) of the decay particle. After several trials, only 4 topological variables are used to obtain the D0 candidates. These variables are:

- DCA from kaon to the primary vertex divided by the deviation of the kaon and the primary vertex (trk1vtx/trk1vtxdev).
- DCA from pion to the primary vertex divided by its deviation (trk2vtx/trk2vtxdev).
- Decay length divided by its error (dist/disterr).
- Probability of the fit (Prob).

KFParticle define the deviation from a particle to the primary vertex as the square root of the chi squared of the track's fit. This is an estimation of the quality of the fit performed in that particular track, for the particle reconstruction.

3.5 Charmed meson signal

After the selection of the minimum bias events, the quality cuts for the tracks and the identification of kaon-pion pairs with opposite sign, the invariant mass of the D^0 can be reproduced using KFParticle package and applying some topological cuts to improve the signal to background ratio. Figure 3.8 shows the D^0 + D^0bar peak obtained with the full statistic available in Run 2014.

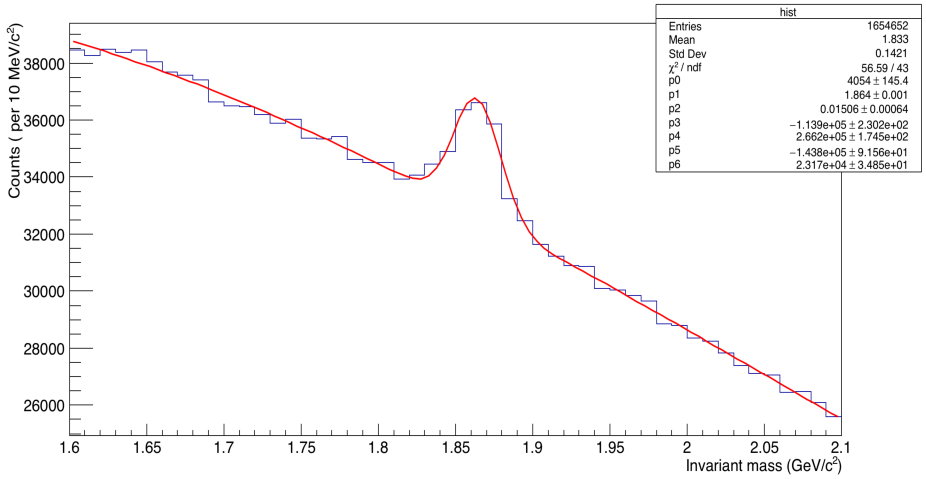

Figure 3.8: Raw D^0 signal obtained (without cut optimization) with the Run 14 data sample.

A Gaussian function is fitted for the signal and 3rd order polynomial for the background. The result obtained for the invariant mass is 1.864 GeV/c^2 ± 0.001 GeV/c^2, being in agreement with the average world measurement of D^0 mass. With the fit

parameters obtained, the yield of the signal is 15262 D^0 candidates, within 3 sigma from the mean value. The cuts used for that signal obtained is shown in Table 3.1

Table 3.1: Non-optimized cuts used to obtain the D^0 signal in figure 3.8.

Fit Probability	> 0.3
trk1vtx/trk1vtxdev	< 0.005
trk2vtx/trk2vtxdev	< 0.0055
dist/disterr	> 5

These cuts are obtained by trial and error to get the maximum yield possible with a clear signal. However no systematic study is done to optimize the cuts. Multivariate techniques were used for this propose.

3.6 Signal Significance

The biggest inconvenience while looking for a desired weak signal (S) in a data sample is dealing with the background (B), mostly coming from random track combinations. A "significant" observation is performed when one or more hypothesis can be proven or refuted from that observation, for example ratio of signal (S) over its error is more than five (5σ). Also, the result obtained will not change if more data included [Sinervo 2002]. This is the standard rule for new particle discovery, which is not our case. Taking the ratio of the signal and its error, one assumes that the errors are Gaussian distributed which might not be always correct. The effective signal or significance of a

signal was introduces to evaluate the signal strength. Equation (4.1) gives the relation of the significance in the case when the background is very well known (zero statistical error can be assumed). Otherwise one has to multiply the background (B) in the formula by a factor of two [Ullrich 2009]:

$$significance = \frac{S}{\sqrt{S+B}} \tag{4.1}$$

To optimize a signal, the significance must be maximized. As an example, the former STAR D^0 analysis based solely on TPC+PID cuts was yielding a significance in the order of 10^{-4} while a typical HFT-based analysis returns significance greater than 10, a gain of about five orders of magnitude.

Traditional analyses use "rectangular" cuts on the reconstructed parameters of the candidate particle decay in a systematic manner to maximize the significance and get the cleanest signal possible. By rectangular we mean fixed-value cuts independent of the value of the rest of the cut variables. By applying rectangular cuts a considerable amount of the signal can be lost because this method does not take into consideration possible correlations between the variables, i.e. it implicitly assumes that the cut variables are independent. While this is true for some cut variables, as we will show later most variables are correlated to varying degrees.

3.7 Multivariate analysis

Machine learning is a branch of computer sciences that determine patterns in large data sets, by applying multivariate analysis models to identify a common behavior. Machine learning techniques are widely used in many data analysis problems and are also

in wide use in high-energy physics experiments. The two major types of problems that machine learning addresses are classification and regression. A regression problem estimates the value of a given variable given its parameters. The simplest regression problem is calculate the slope of a line given two points in a 2-D coordinate system; in this case the equation of the line will exactly predicts the outcome of any other given input value. Classification problem consists in separating two or more set of data.

Machine learning problems start by selecting a multivariate technique or classifier to be used. There are no specific guidelines nor condition pick a classifier; usually constrain comes from computational limits since the outcome of the classifiers vary with each data sample. After selecting the technique to use, the most important phase in the process is the training where a portion of the data goes through the classification or regression process. There are two types of training, a supervised training where the algorithm is provided with a sample of the required output, and unsupervised training where the algorithm must find the patterns of the data by itself. The classifier will provide a probability of the input parameters to be the desirable output. The last step is to validate the output of the classifier by testing it to a sample of the statistic available. This testing sample must be different of the sample used for training, and must be sizable enough to assure that the classifier converge to the desirable output. Usually the fraction of training to testing sample is 3:2 [Ng 2014]. The multivariate techniques considered in this analysis, are briefly explained next:

- Likelihood: this method relies on the probaility density functions of the signal and the background inputs. The likelihood of an event to be either signal or background is

obtained by multipliying the probability of each individual event (which are suppose to be independent) in the training phase, and normalizing it by the total likelihood of all the event [Hoecker et al. 2007].

- Fisher: is a type of supervised method for classification problems where a multidimensional phase space is reduced by a linear discriminator. The linear discriminator is a one dimension variable obtained from the hyperspace of correlated input variable, that maximize the separation between the mean of the input signal and the mean of the background and maintaining events from the same class in a close vicinity [Alpaydin 2010].
- Boosted Decision Trees (BDT): is a binary decision structure, where a variable undergoes a finite series of split criteria until a condition is fulfilled. The phase space is split into several regions that are identified either signal or background in the training stage. Each decision is weighted according to the average of the individual decision tree depending if the event belongs to the signal or background category. In some sense, the BDT is a finite series of rectangular cuts. Each cut is defined by the separation power between the signal and the background [Hoecker et al. 2007].

The Toolkit for Multivariate Analysis (TMVA) is a set of object oriented packages integrated into ROOT for classification and regression problems. This package is a powerful tool in high-energy physics analysis to identify signal in large background situation [Hoecker et al. 2007]. All of the previous multivariate techniques were use by TMVA to maximize the efficiency of the acquired signal.

3.8 Simulation sample

Monte Carlo simulation of the daughter particles is needed to compare with the data. In this analysis we used supervised training since a simulated signal is used as the input to train the classifier.

STAR collaboration has a standard framework (called Starsim) for all detector simulations based on GEANT-3 (Geant) package [Agostinelli et al. 2003]. Geant simulates the passage of particle through matter taking into account all physical processes, in this case each individual detector in STAR. The experiment description varies from year to year since insertion and/or decommission of individual detectors, as it is the case of Run 2014 with the commission of the HFT. Starsim takes into account the geometry used for the run to study. The geometry of each detector must be coded individually and coupled to the Starsim framework to perform a simulation. Figure 3.9 shows the beam pipe (left) and a sector of the SSD (right), partially or fully implemented coded by the author of the dissertation. These figures are the actual Geant representation of the geometries in STAR. Each sub-detector has a similar visual representation.

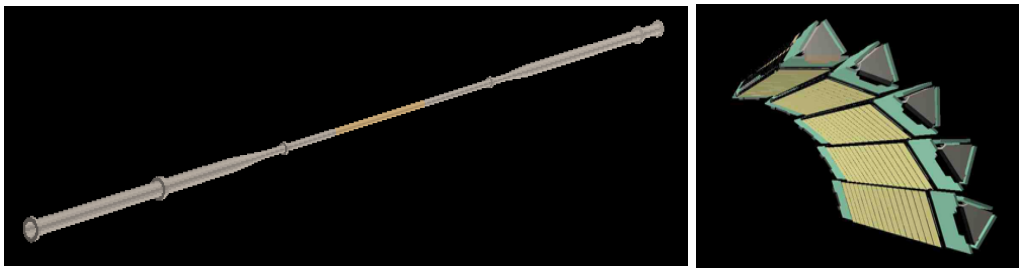

Figure 3.9: Geant geometry of the beam pipe (left) and a sector of the SSD (right) for STAR run 2014.

The particle production and its kinematic is performed within Geant following a QCD inspired event generator from more complex simulation packages for particle decay like Pythia [Sjöstrand et al. 2015] applying most of the known decays for several subatomic particles. Also the Hijing model [Wang, Gyulassy 1994] can simulate the heavy ion collision itself and the subsequent particle production. A pure D^0 sample was produced to discriminate the signal by training a specific classifier, using the only studied decay channel kaon-pion. A Hijing simulation is certainly more realistic simulation since it can also reproduce the background; however, the cleanest signal possible is needed for the purpose of the classification. Figure 3.10 shows the input distribution in p_T of D^0 in simulation performed.

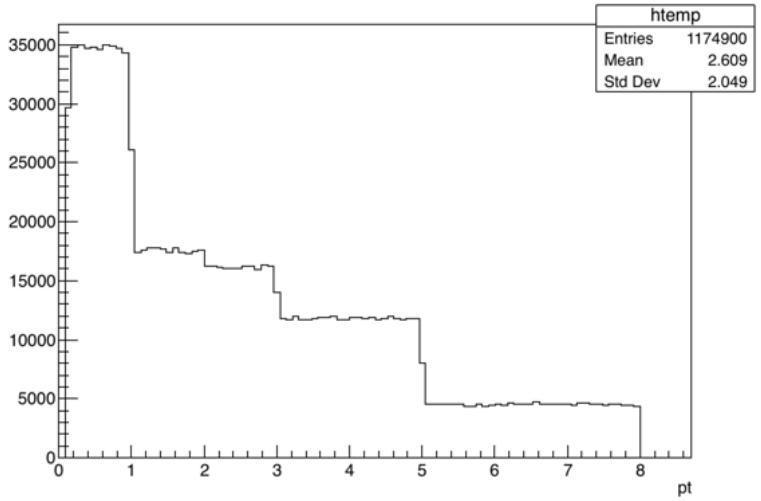

Figure 3.10: The p_T distribution of simulated D^0s. The number of particles produced is different for different momentum regions so that the momentum distribution after reconstruction is almost flat.

A total of about 25 thousand events were simulated with a Gaussian shape of mean 0.1 cm and width 2.5 cm in the z axis, to assure that the produced tracks have hits in the HFT. There are 50 D^0 particles per event, which yields more than a million D^0 to perform the training. The pseudorapidity value of the particles is a flat distribution in the interval [-1,1]. A step transverse momentum distribution is needed to produce a flat p_T distribution after the reconstruction since the reconstruction efficiency drops at lower p_T values. The efficiency studies will be discussed in section 4.2. A flat p_T distribution of the input signal is needed in the training, so there is no bias of higher over lower transverse momentum values.

The same analysis code is used to reconstruct both data (see section 3.4) and the simulation, with exactly the same base cuts to reduce the background in the data. Figure 3.11 shows the mass and p_T of the reconstruction results of the simulation sample.

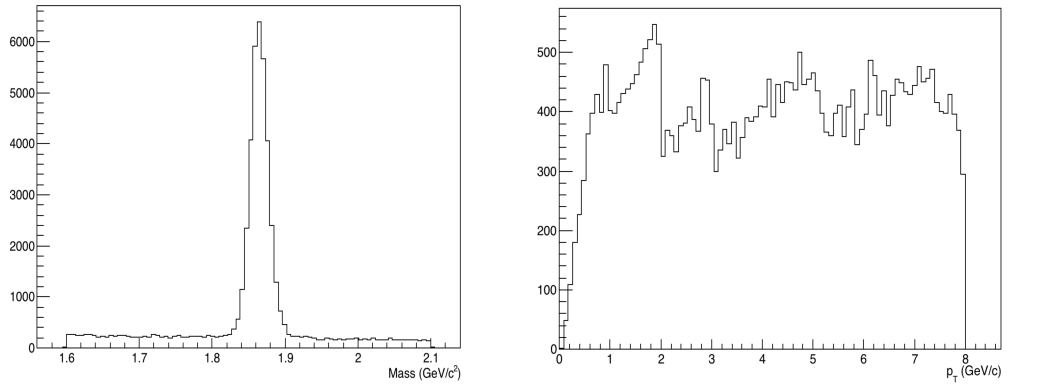

Figure 3.11: Reconstructed invariant mass (left) and the reconstructed transverse momentum (right) of D^0 in the simulation sample.

The total number of D^0 candidates reconstructed is ~50 thousand. Some of these candidates are results from combinatorial background as can be seen outside of the D^0 mass range in figure 3.11 (left). The number of reconstructed D^0 events within the mass range is 36418, which are the ones used for the training and produce a pseudo flat transverse momentum distribution (figure 3.11 right).

3.9 Training phase and classifier results

One of the advantages using the TMVA package is its simplicity to apply different classifiers without modifying many parameters to obtain good results. A supervised training is used to separate signal and background. In this case, the signal is the Geant simulation sample prepared (see previous section), while the background is the actual data sample. Figure 3.12 shows the reconstructed mass of both signal and background samples used for the training phase.

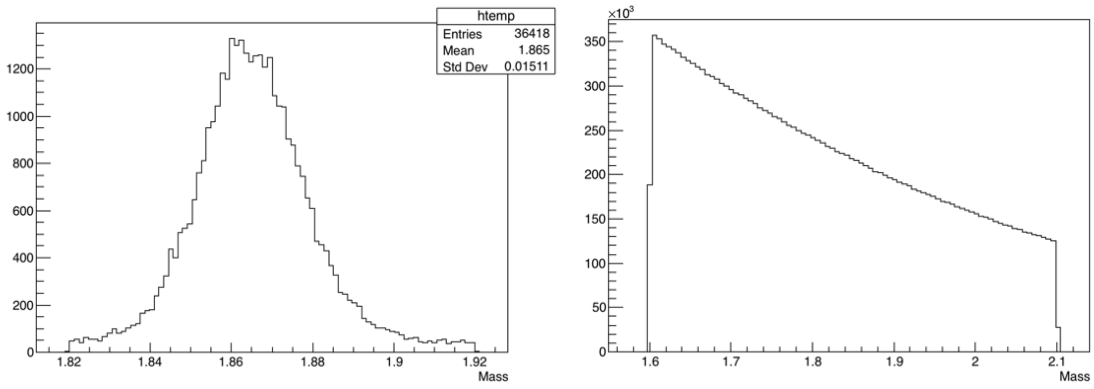

Figure 3.12: Reconstructed mass for the signal (simulation) within mass range of D^0 (left), and for the background (data) in the studied mass range (right). Note the different x-axis range in the histograms.

The total number of reconstructed D^0 within the correct mass range is ~36 K, and there are two million candidates for the background. These candidates will be used in the in the training and testing phase by TMVA. The ratio of training to testing events used for this study is 3:2. The input number of candidates for the training phase plays an important role since a large number of events might not improve the discrimination power of the classifier but increase the computational time, while a small number of events might result in a poor training, which translates into a poor classification. Figure 3.13 show normalize histograms of the set of variables used in the training for both signal (blue) and background (red), where the separation power between signal and background of these training variables can be seen.

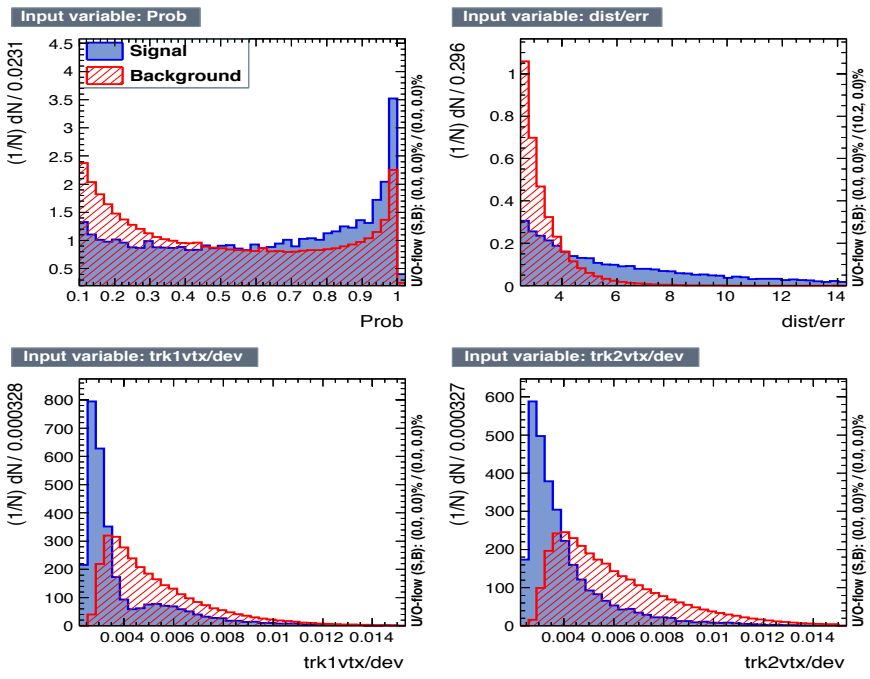

Figure 3.13: Variables used for the training of the signal and the background. The probability of the fit (top left), decay length divided by its error (top right), DCA from kaon track to the primary vertex divided by its deviation (bottom left) and for the pion (bottom right).

The chosen variables to separate the signal and background are the same as selected in section 3.4: DCA from kaon/pion track to the primary vertex divided by its deviation, decay length divided by its error and the probability of the fit. Several variables were tested in the training; however the best result and computing time was obtained with the selected variables. The advantage of using few variables to train the classifier is less computational time besides few variables imply less modification the signal within the background.

The computational time of the TMVA package for this study, with all the parameters set before is typically twenty minutes. The three classifiers mentioned in section 3.7 were used plus the optimization of rectangular cuts (CUTS) which is also available in the package. Figure 3.14 shows the performance of each classifier ranked by best efficiency of the signal and purity. BDT provides the best result in this analysis.

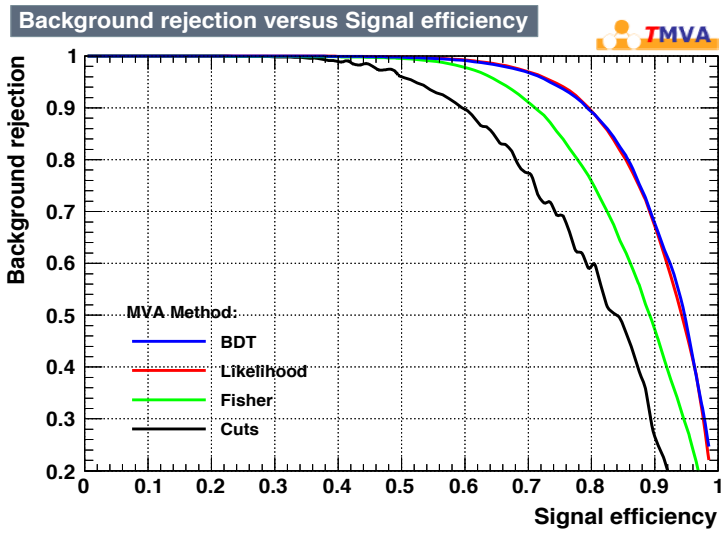

Figure 3.14: Performance of each classifier, ranked by best efficiency of the signal and purity.

It is important to check that the training and testing samples behaves similar, so the result can be applied to a larger sample without any bias. Figure 3.15 shows the results overlapping the training and testing samples for each classifier studied. The three classifiers used show good agreement between training and testing samples. For the background input the overlapping is almost perfect, since the number of entries used in the background is very large. This agreement shows that no more entries for the background are needed; a smaller sample might be used however the performance obtained is acceptable. The overlapping for the signal is not perfect but there is no bias during the training phase as seen in figure 3.15. More simulation sample can be produced to increase the number of entries for the signal but the main constrain is the computational resources since producing a large signal sample like the one used consumes a lot of computational time and disk space. Besides, the flat momentum distribution must be manually engineered since the total reconstruction efficiency depends on the transverse momentum of the candidate.

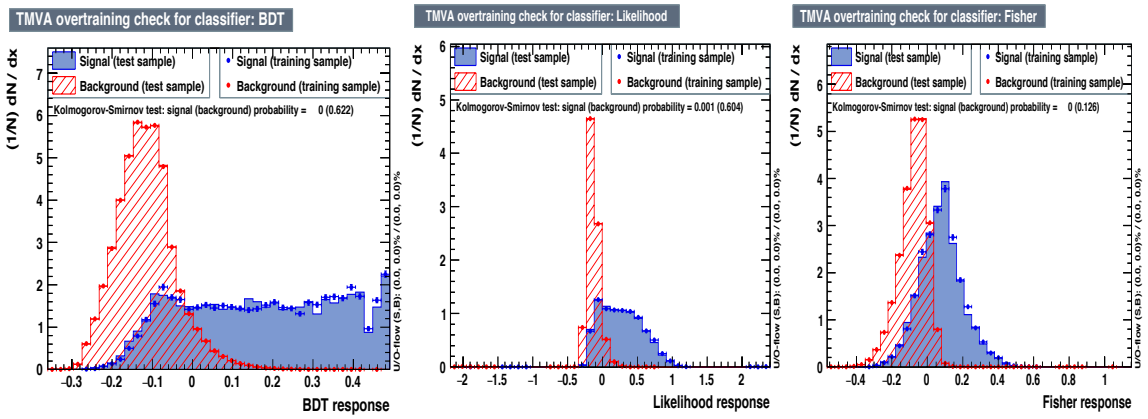

Figure 3.15: Overlapping of the results of the training and testing samples for BDT (left), Likelihood (center) and Fisher (right).

The classifier response can be quantified a single variable (called "TMVA cut" in this analysis); so from the four variables used in the training, the output is only one variable that discriminates signal and background efficiently. The table 3.2 shows the TMVA cut values of signal and background from the figure 3.15. The x-axis in the three figures 3.15 represents the TMVA cut. The signal becomes more prominent than the background after certain value (table 3.2) depending on the performance of the classifier. Ideally, using a classifier with total discrimination power, the TMVA cut will separate completely the signal and the background; however it can be seen in figure 3.15 that after the crossing point of signal and background, there is still some residual background. Below the TMVA cut there is underlying signal that could not be separated by the classifier.

Table 3.2: TMVA cut value of when signal overcomes the background.

Classifier	Cut
Likelihood	0.058
Fisher	0.016
BDT	0.053

Figure 3.16 shows the D^0 reconstruction mass for all the centralities and integrated transverse momentum using TMVA cut greater than zero using the BDT classifier, which gives the best result from all the classifiers tested.

As in section 3.5, a Gaussian function and 3rd order polynomial is fitted. The result obtained for the invariant mass is 1.864 GeV ± 0.001 GeV. The yield of the signal

(within 3 sigma from the mean value) is 39064 ± 1776 particles, which improves considerably the result without optimized cuts.

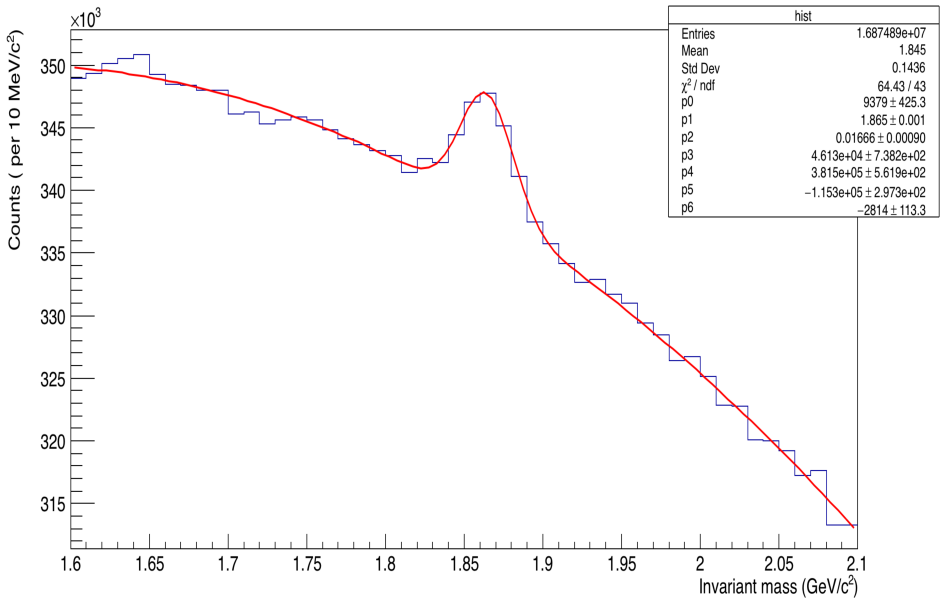

Figure 3.16: Reconstructed D^0 mass with TMVA cut and a Gaussian plus 3rd order polynomial.

3.10 Selection of TMVA cut

For the physics analysis all these reconstructed D^0 particles must be separated into centrality and p_T bin. The TMVA cut should vary for each of these criteria. Figure 3.17 shows the variation of the TMVA cut, the calculated yield and significance for the result shown in figure 3.16. The criterion to select the best result is to obtain the maximum yield with a good fit and a considerable significance. Significance greater than 5 must be consider good. This variation will be considered for the systematic error studies.

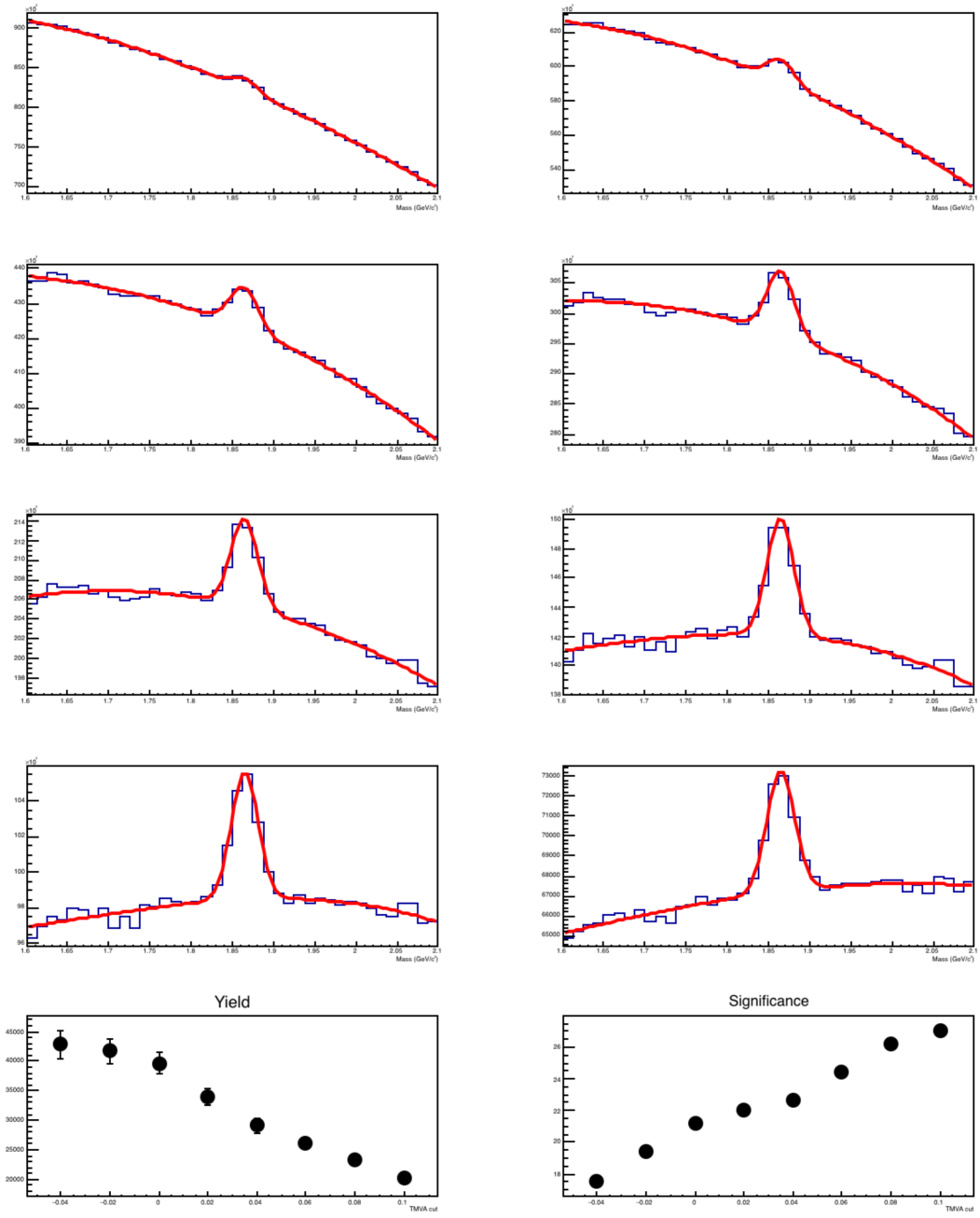

Figure 3.17: Variation of the TMVA cut for the D^0 candidates with integrated p_T spectrum and all centralities. Two bottom plots are the yield (left) and the significance (right) for each of the different TMVA cuts.

CHAPTER 4

Physics results

4.1 Invariant mass spectra

Many interesting physical properties about QGP can be obtained with the calculation of the spectrum of a specific particle or a set. These include simple properties like the production cross section of the particular species or the fitted inverse slope ("temperature") for thermal studies. Here we are interested in more complex observables like the Nuclear Modification Factor, as we discuss it below. The D^0 charm meson is used here for this purpose. The invariant yield is given by [Adamczyk et al. 2014]:

$$dN = \frac{1}{2\pi p_T}\frac{1}{N_{ev}}\frac{d^2N}{dp_T dy}\frac{1}{\Gamma}\frac{1}{eff} \tag{4.1}$$

The spectra of particles produced in a heavy ion collision are taken with respect to the transverse momentum (p_T) since this quantity is Lorentz invariant, within a certain rapidity region (Δy). The invariant yield (dN) should be first normalized to the total number of events (N_{ev}) in the sample. The proper spectrum of a particle is obtained by the branching ratio of the particle (Γ) in the selected decay channel, in this case Γ=3.88% for D^0 -> K π. Also, the efficiency (*eff*) correction for the spectrum must be included and it includes both the geometrical acceptance and the reconstruction efficiency, which can be a function of p_T and y. This last correction is important in order to perform R_{AA} measurements since the data must be compared with a p + p baseline spectrum which will have a different efficiency correction than Au + Au sample (details in the next section).

The biggest challenge to obtain the spectra is getting an optimized and robust signal in different p_T and centrality bins. The methods proposed, maximize the yield in different bins to obtain reliable physics measurements. The TMVA cut can be different per individual p_T and centrality bin. Ideally, a single training would be done per each of these bins (30 bins in this study); however, there is a computational limitation since producing all these simulation samples for different trainings will take a lot of disk space to obtain a sizable amount of events per bin for a good performance of the classifier. For this study, a single training was performed for all p_T and centralities. Figures 4.1 to 4.5 show the yields for different p_T bins at centralities 0-80%, 0-10%, 10-20%, 20-40% and 40-80%. Table 4.1 has the results of the yields obtained in the figures together with the corresponding TMVA cut.

Table 4.1: Result of the yield per centrality and p_T bins with the used TMVA cut.

Centrality	p_T (GeV/c)	Yield	Error	Significance	TMVA cut
0-80%	0.7	536	162	3.35	0.09
	1.5	17559	1099	15.36	0.00
	2.5	9550	556	16.77	0.08
	3.5	3026	241	12.28	0.16
	4.4	778	122	6.33	0.16
	5.8	440	69	6.17	0.16
0-10%	0.7	129	44	2.79	0.09 (Prob>0.97)
	1.5	1684	200	8.35	0.12 (Prob>0.65)
	2.5	2176	239	8.96	0.14
	3.5	547	103	5.64	0.20 (Prob>0.3)
	4.4	86	15	6.02	0.36
	5.8	50	10	6.12	0.38
10-20%	0.7	308	97	3.02	0.10
	1.5	2306	263	8.58	0.08
	2.5	3312	322	9.81	0.08
	3.5	902	110	8.19	0.18
	4.4	167	26	6.51	0.30
	5.8	123	30	4.07	0.18
20-40%	0.7	180	51	3.19	0.12
	1.5	3046	195	15.48	0.08
	2.5	2743	187	14.52	0.10
	3.5	1195	161	7.75	0.08
	4.4	318	50	6.06	0.18
	5.8	117	21	5.89	0.26
40-80%	0.7	198	41	4.51	0.04
	1.5	849	76	11.15	0.04
	2.5	553	54	11.65	0.10
	3.5	279	29	10.27	0.16
	4.4	68	13	6.83	0.24
	5.8	35	8	5.15	0.26

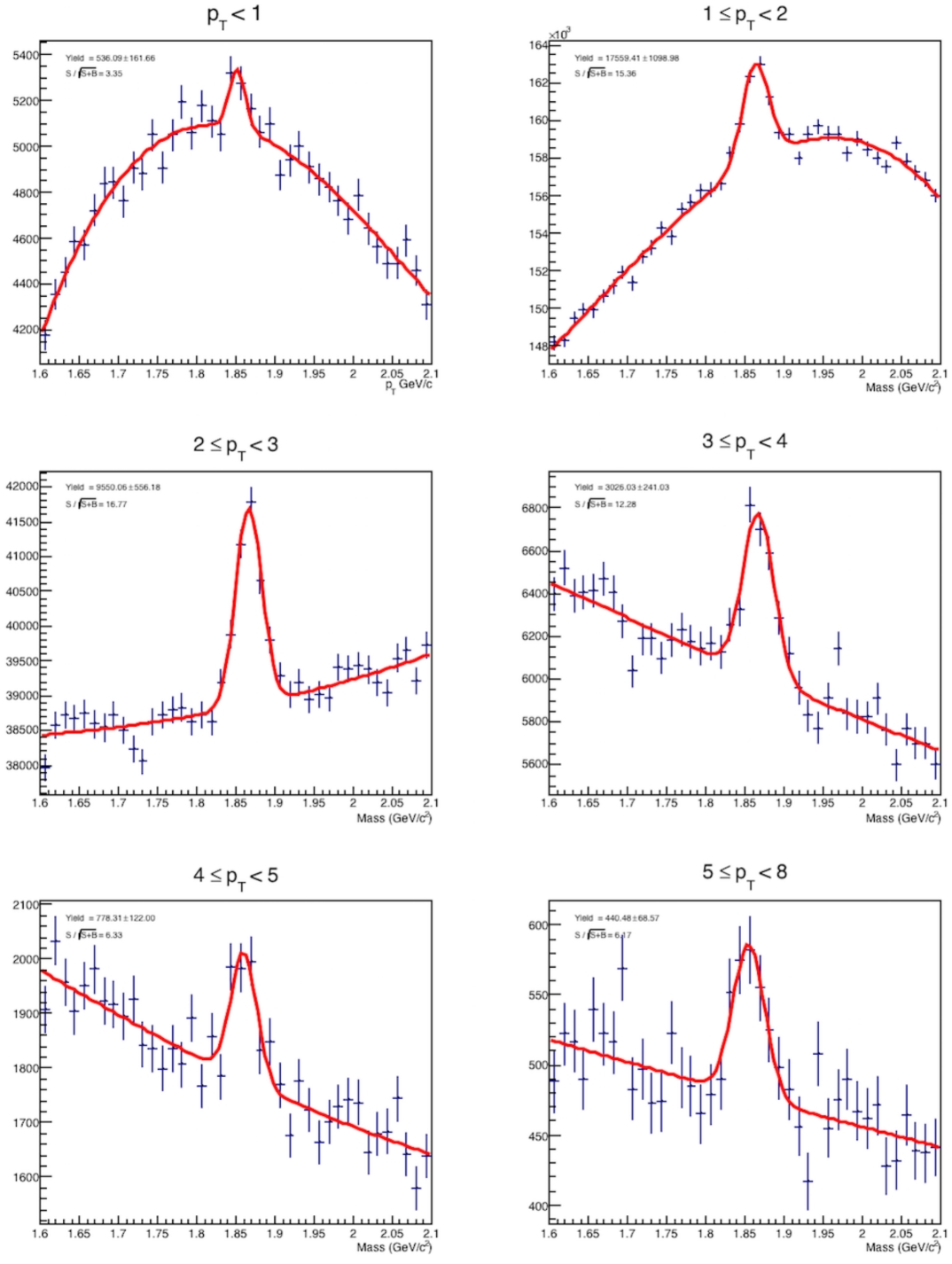

Figure 4.1: Signal obtained for different p_T ranges for near minimum bias collisions, the centrality range of 0-80%. Clear D^0 peaks are seen in all p_T bins.

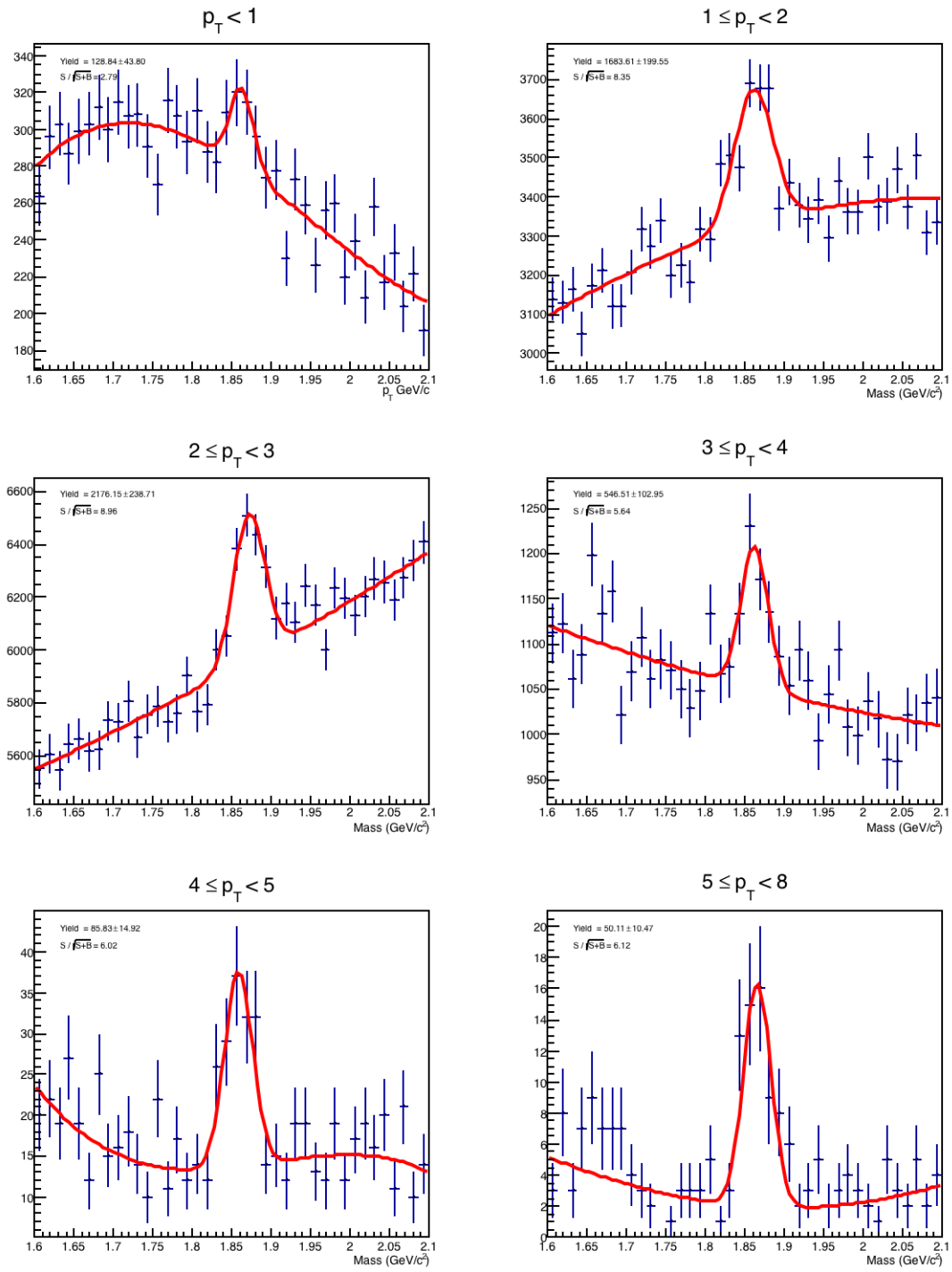

Figure 4.2: Signal obtained for different p_T ranges for the most central collisions, the centrality range of 0-10%.

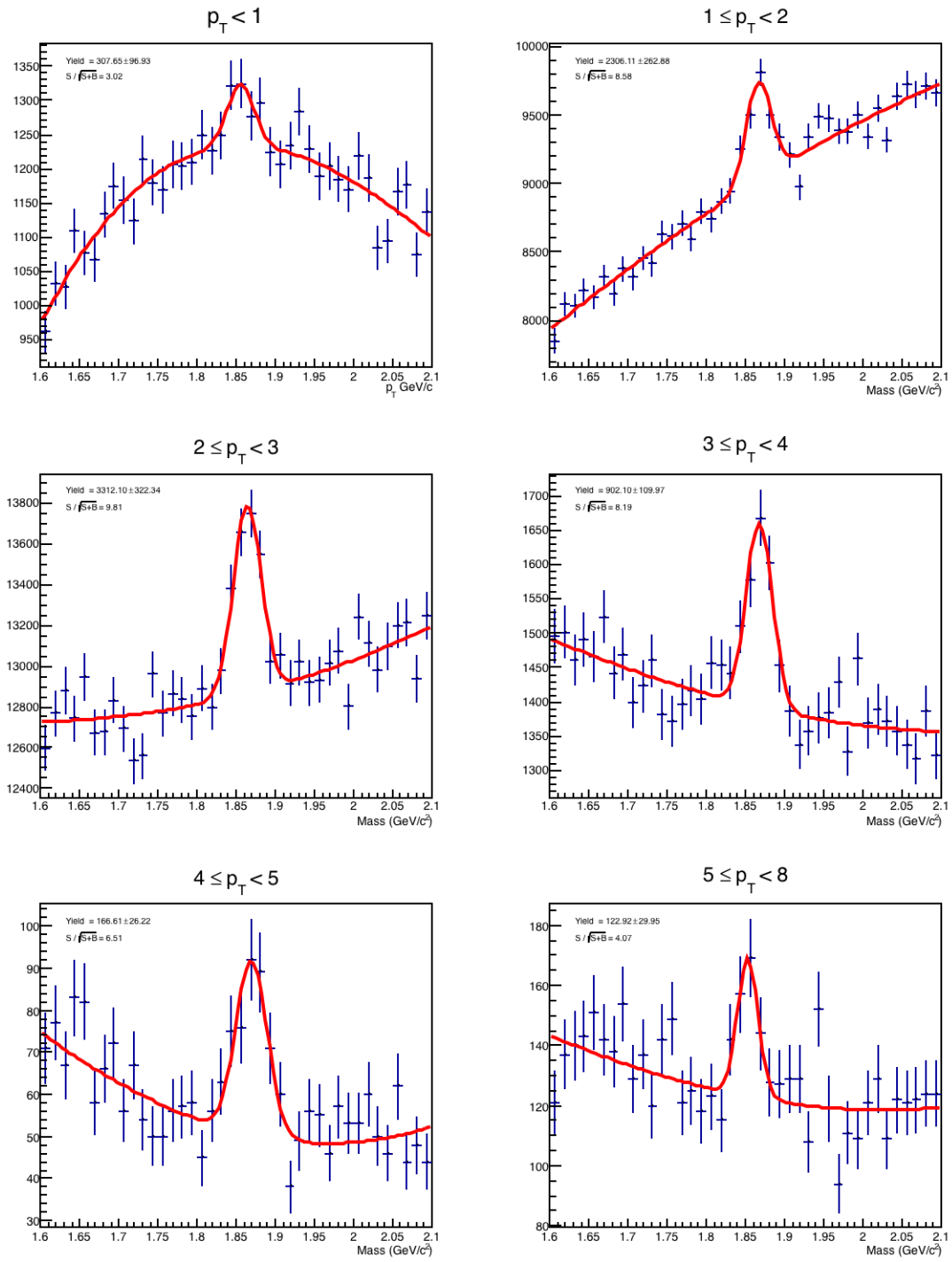

Figure 4.3: Signal obtained for different p_T bins at centrality 10-20%.

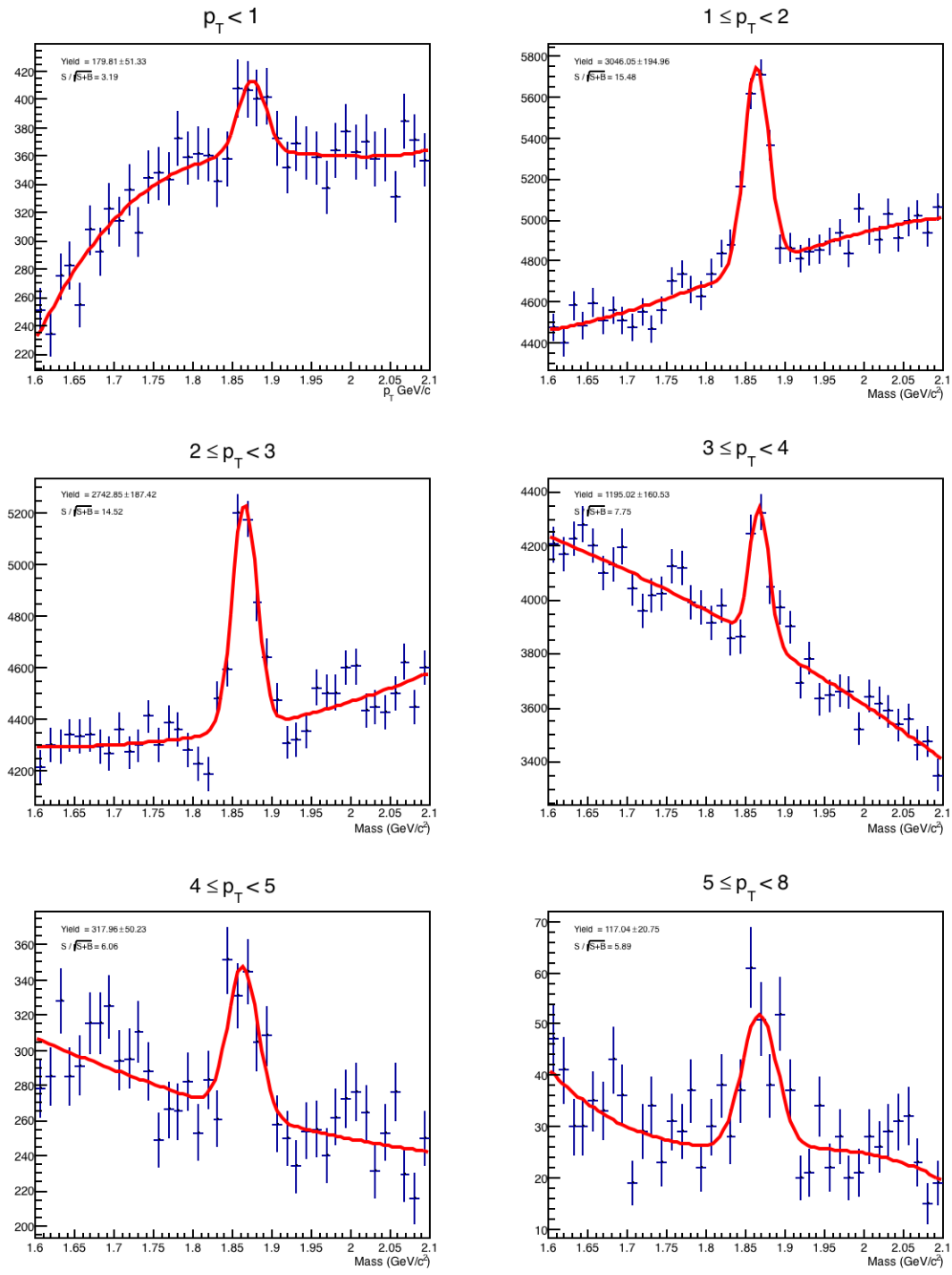

Figure 4.4: Signal obtained for different p_T bins at centrality 20-40%.

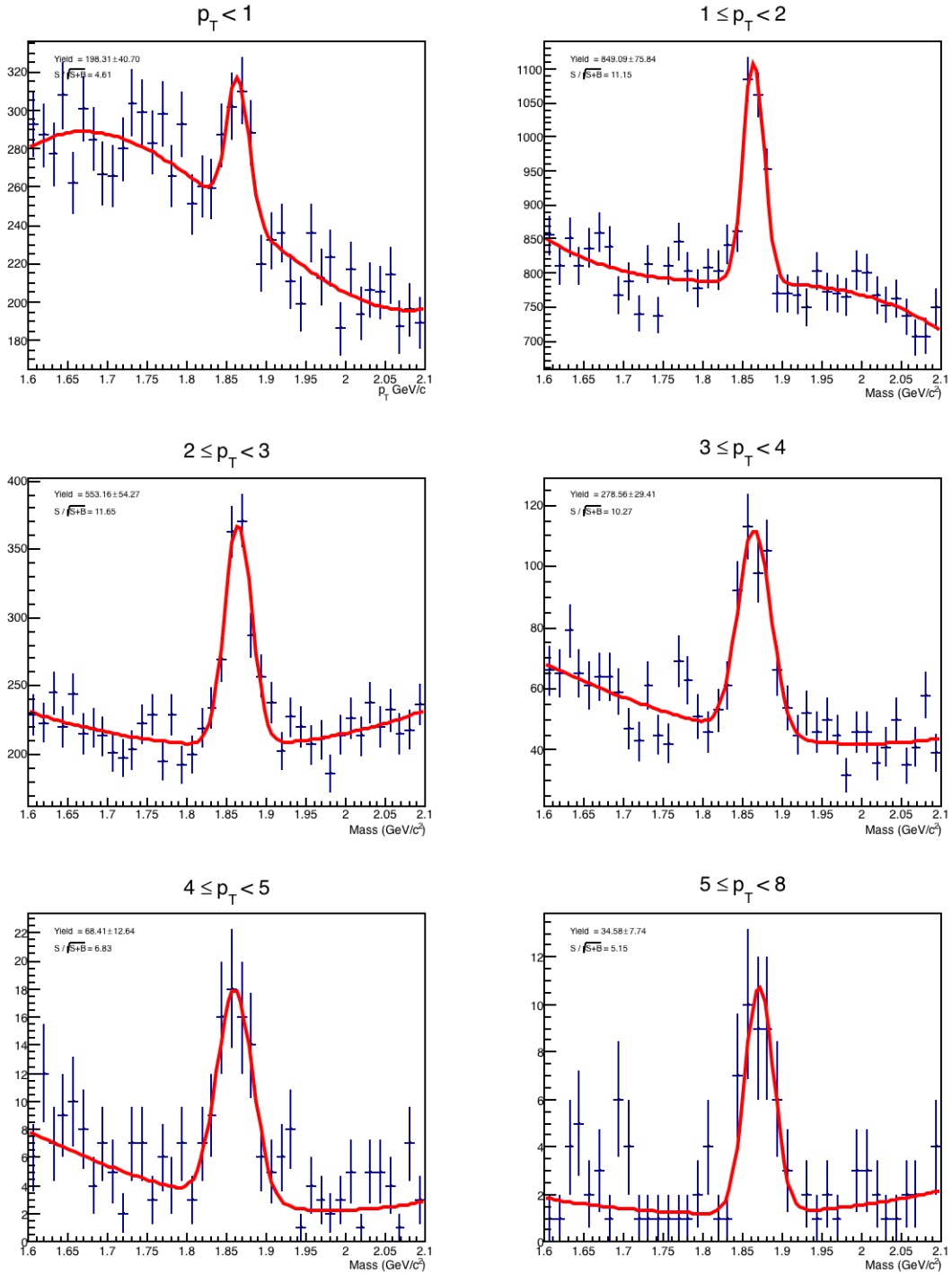

Figure 4.5: Signal obtained for different p_T at centrality 40-80%.

Figure 4.6 shows the results of the raw yield obtained at different p_T and centrality bins from the table 4.1. Figure 4.6 shows the statistical error bars only and obtained from the fit parameters. The systematic error estimation is discussed in section 4.3. The last p_T bin (5.8 GeV/c) contains the value for the yield of D^0 candidates within a p_T in the range of [5,8] GeV/c. The spectra of the D^0 meson can be extracted for the data in this figure (see equation 4.1). It must be corrected by efficiency to provide the corrected spectra. Since for each point presented in figure 4.6 a different TMVA cut was used, it is critical that the efficiency calculation is done for each point individually in order to obtain the proper spectrum for each centrality. This is discussed in the next section.

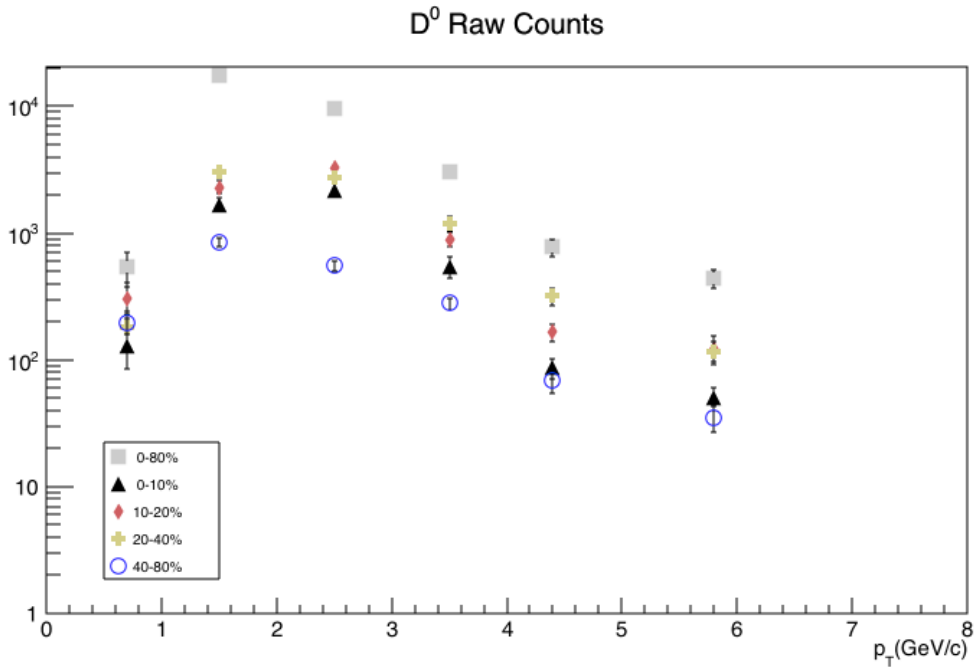

Figure 4.6: Uncorrected D^0 yield for the five centrality classes. The points are the raw yield (raw counts) obtained for different p_T and centrality bins.

4.2 Efficiency correction

Normally, the efficiency correction in STAR is evaluated by embedding simulated particles in real events (to best represent the "background" environment) and run them over the full reconstruction chain BFC. The insertion of the HFT detector brought new challenges to the embedding infrastructure already in STAR. The pointing resolution of the Pixel is within the order of magnitude of its physical irregularities; a detailed survey of the active area of the detector is performed before the run to take into account these irregularities and provide accurate results. In simulation the Pixel detector is shaped as an ideal structure, so embedded particles with the current STAR setting will cause incongruences in the geometries used since the simulation will be done with ideal geometry while the reconstruction of the data is with real geometry, and this difference will cause a complete mismatch in the tracking. By the time of this work, several complications were presented since it is still very challenging to insert the realistic geometry of the Pixel to the STAR simulation framework. It is worth mentioning that the TPC does not have this problem due to its larger pointing resolution (~ mm). Currently there are several efforts within the collaboration that try to solve this problem.

Here we used an alternative approach, which is to use fully simulated MC Hijing events as the best estimate of the background and then estimate the efficiency in reconstruction of D^0 mesons. A total of ~150k Au+Au 200 GeV Hijing events embedded with 20 to 50 D^0 per event with p_T in the range [0.1 - 8] GeV/c and $|\eta|<1$ was used for that purpose. Pile-up was included in a portion of this simulation. Pile-up refers to extra hits recorded by the detector, as part of the triggered event that does not belong to this

event. Pile-up affects only the PIXEL detector and the reason is its relatively slow readout time (~0.2 ms). Pile-up in Au+Au collisions has two components: the first is minimum bias Au+Au events that occur during the readout time of the triggered event. The other is electron-positron pairs created in electromagnetic interactions between the two Au+Au nuclei. Both sources contribute about the same amount of extra hits to the PIXEL detector. The total amount of pileup hits in the PIXEL is about 10,000 in the first layer and about 4,000 in the second one (recall that a central Au+Au collision leaves about 2,000 hits in each of the PIXEL layers. Two Hijing samples were created. One is for 0-10% central event because this is the sample needed to obtain the R_{AA}. The other is for the most peripheral bin 40-80% which is needed to obtain the R_{CP} ratio. Figures 4.7, 4.8, 4.9 and 4.10 show information about the events, the reconstruction and the parameters used to train the classifier for the signal optimization, of three different samples; the pure D^0 sample simulation (see section 4.3), the Hijing "background" sample and the data sample. This comparison is to check the accuracy of the simulation to reproduce the data.

The results in the previous figures show that the Hijing simulation is reproducing correctly the behavior of the data in the most central events. With this Hijing simulation a first approximation of the reconstruction efficiency, including tracking, acceptance and topological cut, is deduced and presented in figure 4.11 in different p_T bins and for central and peripheral events.

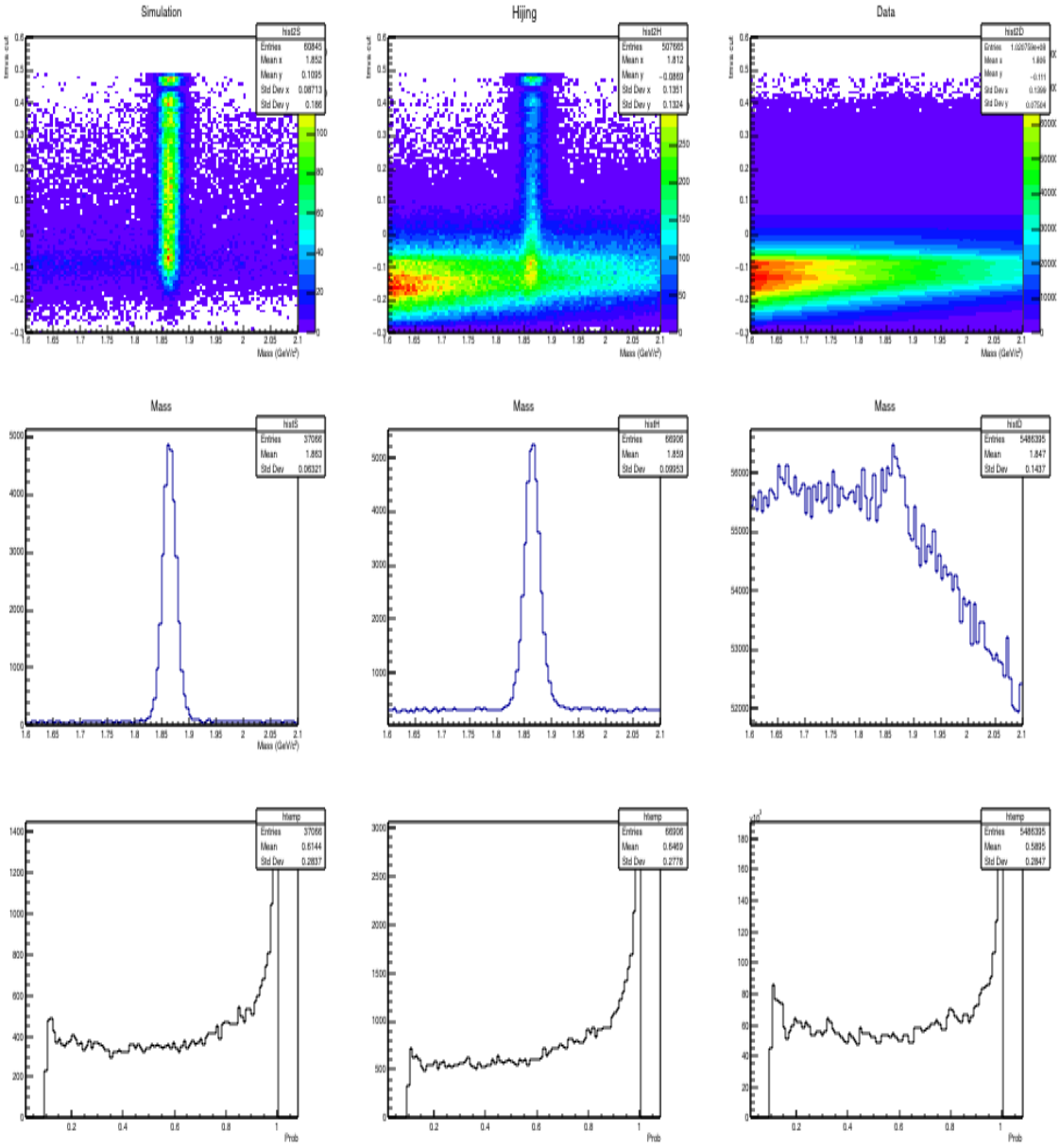

Figure 4.7: Comparison of the pure D^0 sample simulation (left), the Hijing "background" (middle) and data (right): TMVA cut vs reconstructed mass (top), reconstructed mass (middle) and probability of the fit (bottom). Mass and probability are shown for a TMVA cut > 0.02.

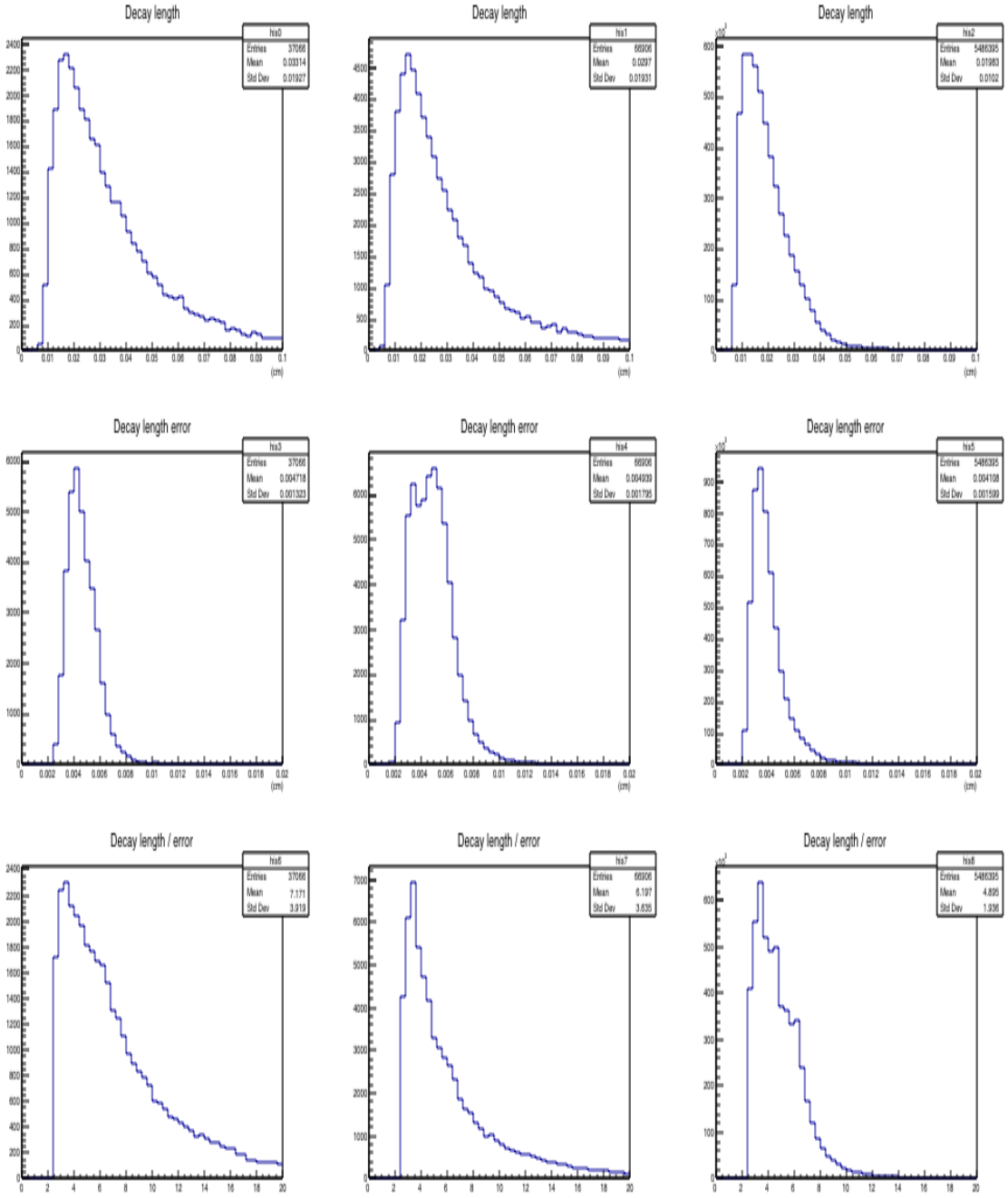

Figure 4.8: Comparison of the pure simulation (left), Hijing (middle) and real data (right); of the decay length (top), the error of the decay length (middle) and the decay length divided by its error (bottom). The values are shown by using TMVA cut > 0.02.

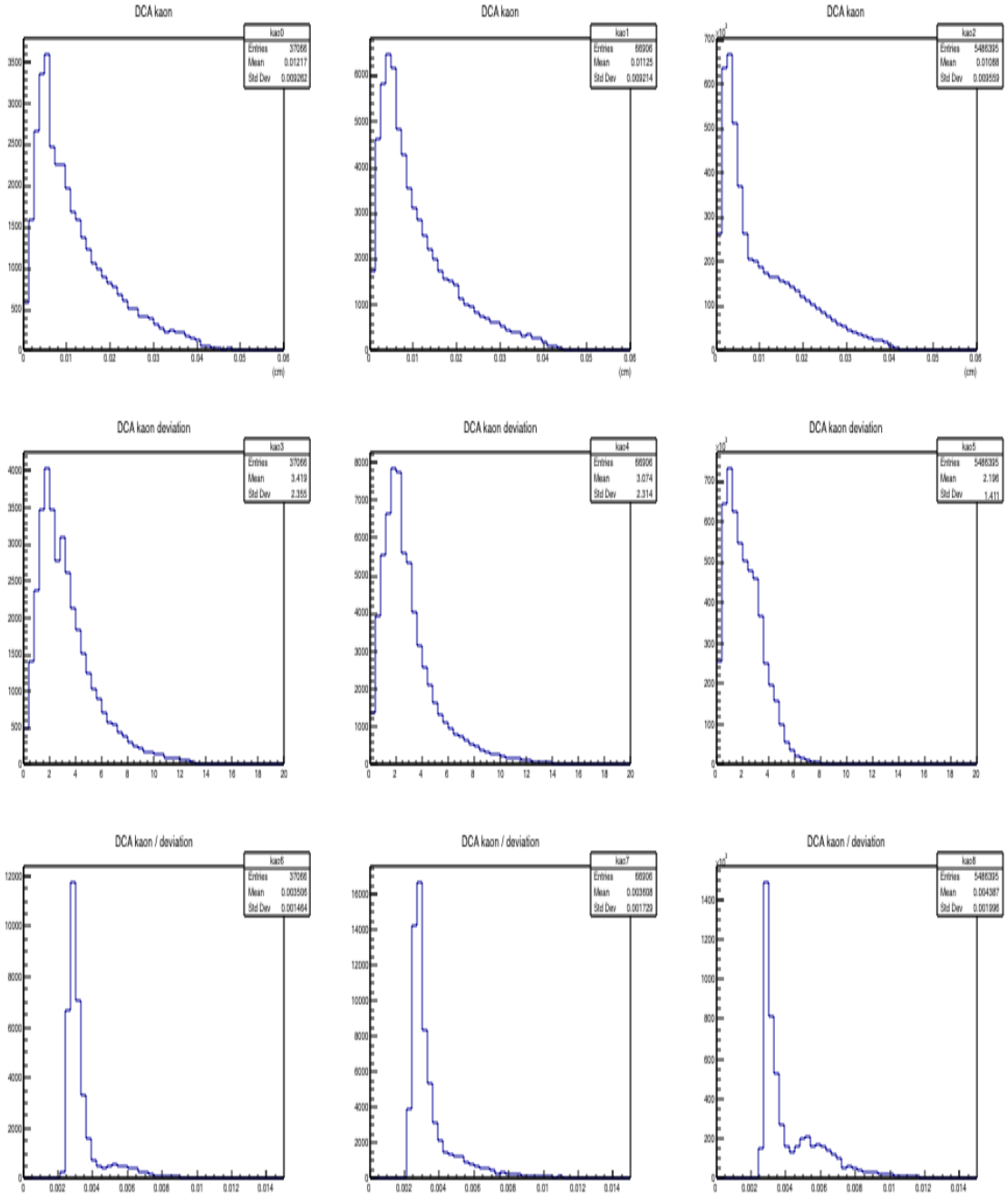

Figure 4.9: Comparison of the pure simulation (left), Hijing (middle) and real data (right); of the kaon DCA (top), the deviation (middle) and the DCA divided by its deviation (bottom). The values are shown by using TMVA cut > 0.02.

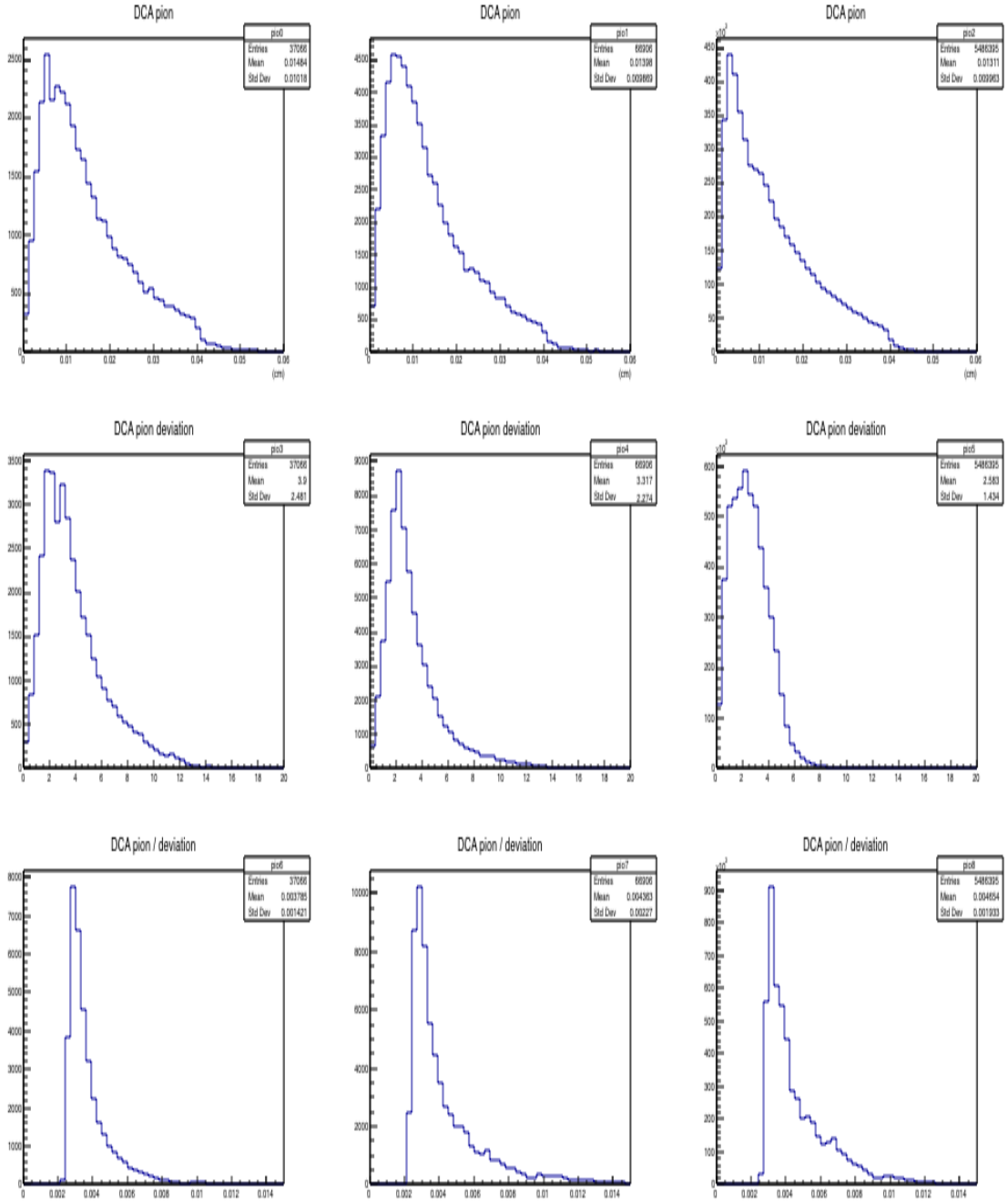

Figure 4.10: Comparison of the pure simulation (left), Hijing (middle) and real data (right); of the pion DCA (top), the deviation (middle) and the DCA divided by its deviation (bottom). The values are shown by using TMVA cut > 0.02.

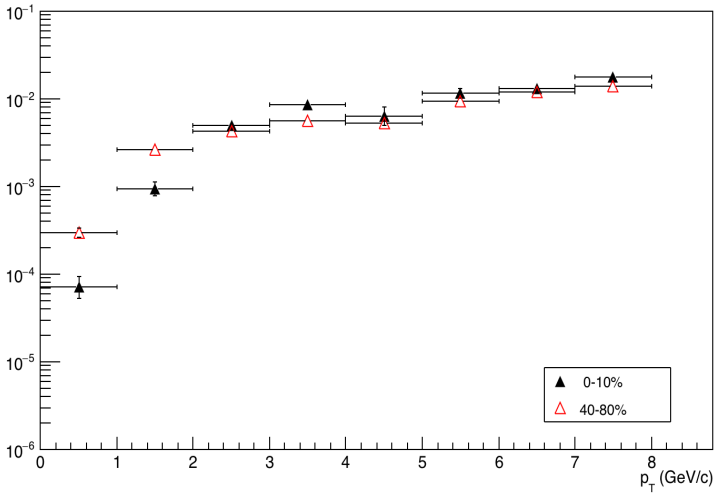

Figure 4.11: Reconstruction efficiency estimation for the most central sample of 0 - 10% (black) and 40 - 80% peripheral events, using Hijing simulated events. Individual TMVA cuts are applied per each p_T and centrality bins.

We should keep in mind that the use of Hijing instead of data events as background has been shown to lead to a slight overestimation (~10-15%) of the efficiency factor since the Hijing environment is "cleaner" than real data. So we expect an underestimation of the charmed meson invariant yields in the final, corrected spectra. By using Hijing simulations we do not correct detector inefficiencies (dead sensors), a 10-20% effect, but some of these individual effects compensate for each other when calculating the final R_{AA} factor. We also use the R_{CP} (central to peripheral) ratio, which is using results from the same data sample and therefore most systematic effects cancel out, as an alternative way to estimate the nuclear modification factor. By comparing the results for R_{AA} and R_{CP} one can estimate the magnitude of the remaining systematic uncertainties in the measurements.

The reconstruction, in this Hijing simulation, is performed with 100% particle identification efficiency because the particle type (ID) of the track is known. An estimation of the efficiency of particle identification must be done in order to obtain the proper total efficiency of D^0 reconstruction. One of the difficulties is to estimate the pion contamination in the kaon sample because there is no simulation available for the TOF in the STAR framework. Figure 4.12 shows the dE/dx for kaons (left) and pions (right) when TOF is available in a portion of the full statistic available. It can be seen for the kaons at p_T>3 GeV/c^2 that some of the particle are pions but are misidentified.

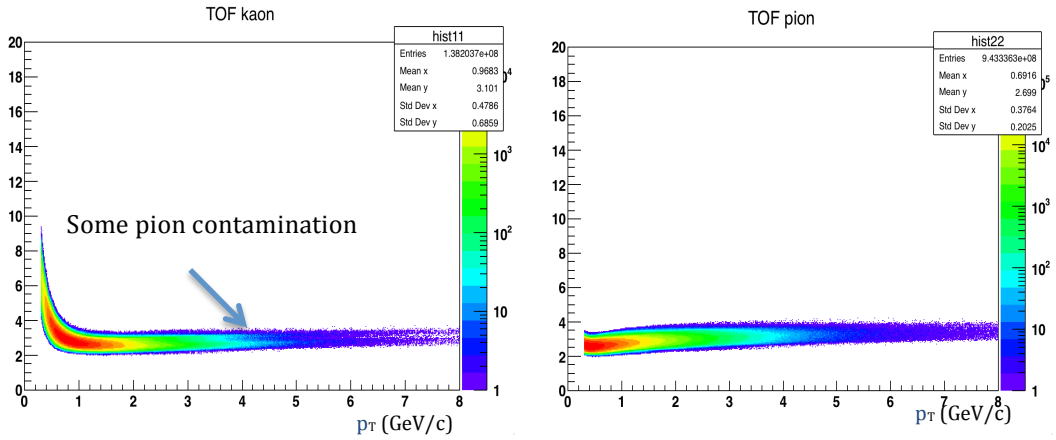

Figure 4.12: The energy loss dE/dx of the kaons (left) and the pions (right) when TOF hits are available, for a portion of the data set.

TOF hits are present in ~60% of the total tracks due to TOF acceptance so this contamination only affects that percentage of the data at p_T>1.6 GeV/c when TOF is not able to distinguish between kaons and pions. The other portion of the data with no TOF hits (~40%) lay on the region where TPC is unable to distinguish the particles (p_T>0.9 GeV/c). For this region the Hijing simulation might be used to estimate the purity of the

kaon and pion sample used for the reconstruction. Figure 4.13 shows dE/dx vs. momentum for the tracks of a Hijing sample with the TPC id requirement and Geant identification (top row), with the track reconstruction identification explained in section 3.3 (middle row) and those with the correct Geant ID of the reconstructed track (bottom row), for kaons (middle column), pions (right column) and both particles (left column).

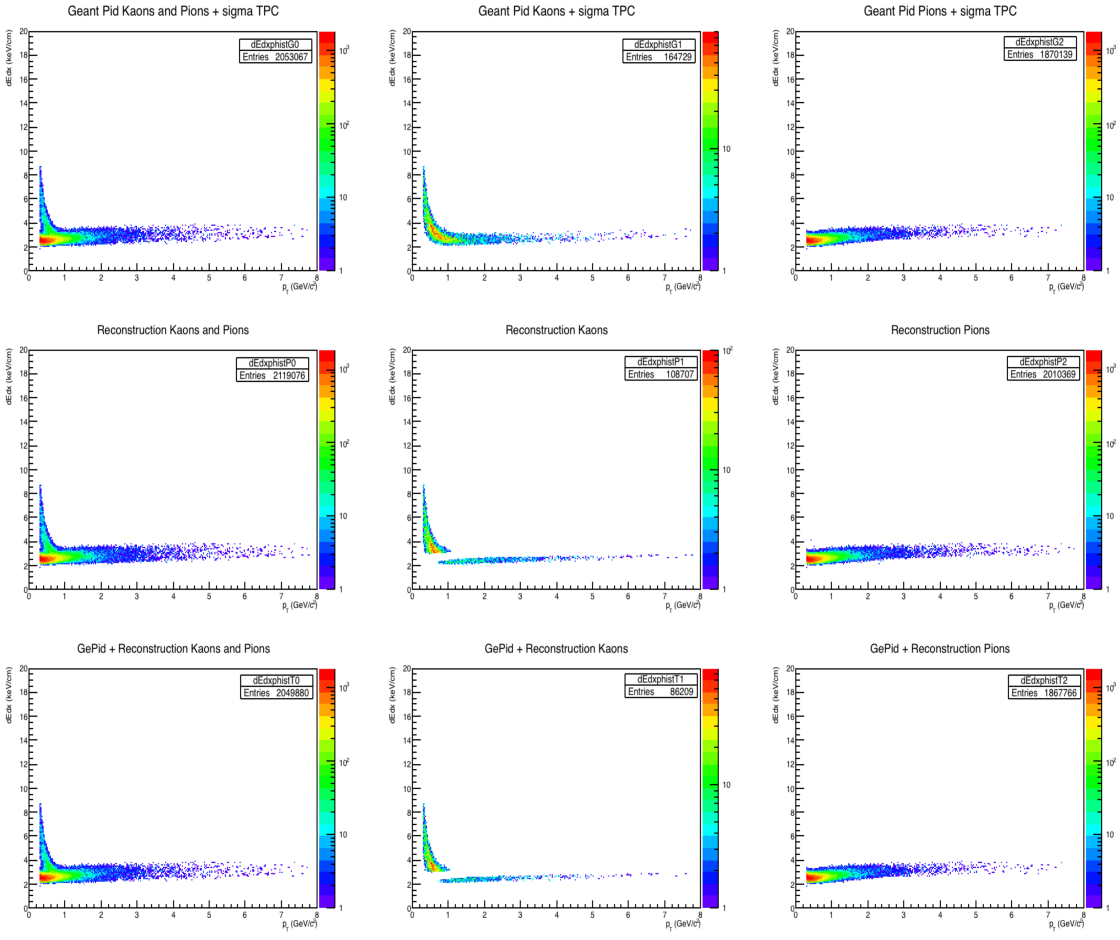

Figure 4.13: The tracks of a Hijing sample with the TPC id requirement and Geant identification (top row), the track reconstruction identification (middle row) and the correct Geant id of the reconstructed track (bottom row).

With the middle and bottom rows information, the purity of the tracks used for D^0 reconstruction can be calculated for different p_T bins. Figure 4.14 shows the purity of the kaons and pions estimated with the Hijing sample in figure 4.13; this result correspond to 40% of the tracks that do not have TOF hit information.

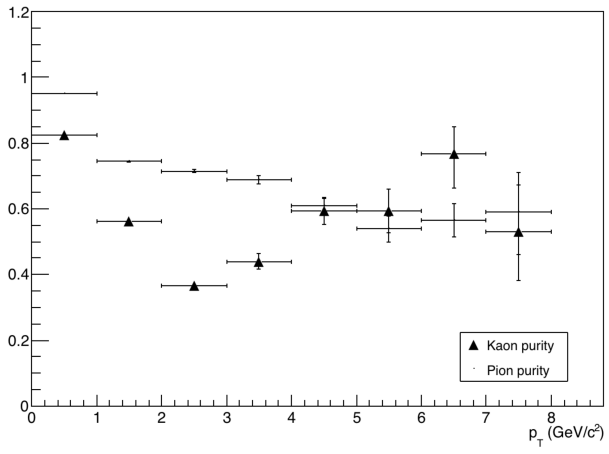

Figure 4.14: Purity of the kaons and pions used for the reconstruction of the D^0.

The efficiency of TOF particle identification was estimated for the Run 2010 and 2011 and used for the STAR previous spectra calculations without the HFT [Zhang 2013]. That estimate assigns a constant value of efficiency 90% for kaons and 95% for pions at p_T>2 GeV/c^2 within the acceptance of the TOF. For the current study, these values will be taken for the total D^0 reconstruction efficiency estimation. Equation (4.2) shows the first approximation of the total efficiency for D^0 reconstruction:

$$eff = \frac{dN/dp_T^{Rc}}{dN/dp_T^{MC}}\left(0.6 * TOF_{eff} + 0.4 * TPC_{purity}\right) \quad (4.2)$$

The fraction in equation (4.2) is the number of reconstructed candidates by the number of Monte Carlo (simulated) D^0 by p_T bin, which is given in figure 4.11. A weighted relation between TPC and TOF purity estimations is multiplied by that quantity. For each D^0 p_T bin we found the average p_T value for the two daughter particles. Then we used figure 4.14 to find the corresponding purity factors and used the average value of kaons and pions to make the PID efficiency correction.

4.3 Systematic errors estimation

There are several sources of systematic errors in a measurement. A typical way to estimate their magnitude is by varying the sensitive cut-variables around their nominal cut-value and recalculate its effect on the final corrected value. The width of the resulting variation in the final result is quoted as the systematic error. Four sources of systematic errors are considered in this study:

- The main variable that provides a systematic error in this study is the TMVA cut. This value was varied 0.02 units of the optimal cut to test the robustness of the signal.
- The binning of the histogram was reduced from 0.0125 counts/(GeV/c^2) to 0.01 counts/(GeV/c^2) (Bin 1); also increased to 0.0166 counts/(GeV/c^2) (Bin 1.6).
- The original range of the mass region fitted was reduced from [1.6,2.1] to [1.75,1.95] and the background was fitted with a 2^{nd} order polynomial.

The fourth source of systematic uncertainties could be obtained by subtracting the same-sign background from the raw signal and then fit the original function to get the D^0 yield. This method was not used because in some of the cases the same sign background does not match the background shape. Figure 4.15 shows the signal and the same sign

background for $1 < p_T < 2$ bin in the most central events 0-10%. Table 4.2 shows the variation of each systematic error contribution to the yield. The systematic error is the standard deviation of the four sources considered in this study. The systematic uncertainty is estimated, on average, to be about 22% for the most peripheral bin (40-80%) and 18% for the most central one.

Table 4.2: Systematic error estimation of the four sources considered.

Centrality	Mean p_T	Raw Yield	Pol2	Bin 1	Bin 1.6	+0.02	-0.02	Systematic Error (%)
0-10%	0.7	129	16%	1%	2%	5%	38%	20
	1.5	1684	52%	4%	5%	75%	10%	37
	2.5	2176	3%	7%	11%	13%	11%	10
	3.5	547	41%	2%	5%	15%	22%	23
	4.4	86	48%	3%	2%	39%	35%	34
	5.8	50	3%	1%	6%	15%	7%	9
40-80%	0.7	198	10%	5%	1%	83%	3%	38
	1.5	849	6%	0%	7%	25%	9%	13
	2.5	553	1%	4%	3%	28%	13%	15
	3.5	279	11%	4%	2%	30%	8%	15
	4.4	68	30%	3%	12%	59%	10%	24
	5.8	35	0%	1%	0%	4%	0%	2

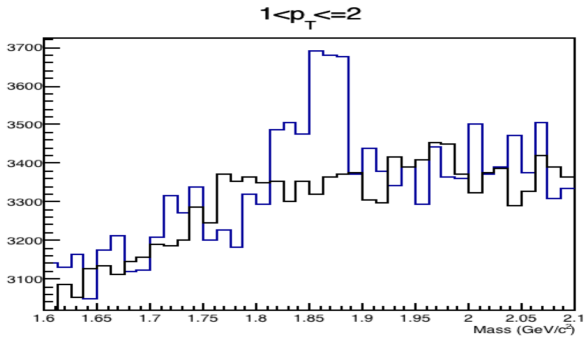

Figure 4.15: Signal (blue) and same sign background (black) obtained in the $1 < p_T < 2$ bin in the most central events 0-10%.

4.4 Charm meson spectra and nuclear modification factor

The raw spectra (without any efficiency correction) of the D^0 for each centrality bin are calculated according to Equation 4.1. The results are presented in figure 4.16 for the different centralities studied. This result is the base for the nuclear modification factor calculations.

The number of binary collisions is obtained from a Glauber model calculation, performed by the LBNL STAR group for Run 2014, and they are listed in the table in the same figure. The number of binary collisions for each centrality bin normalizes the values of the spectra presented in the figure.

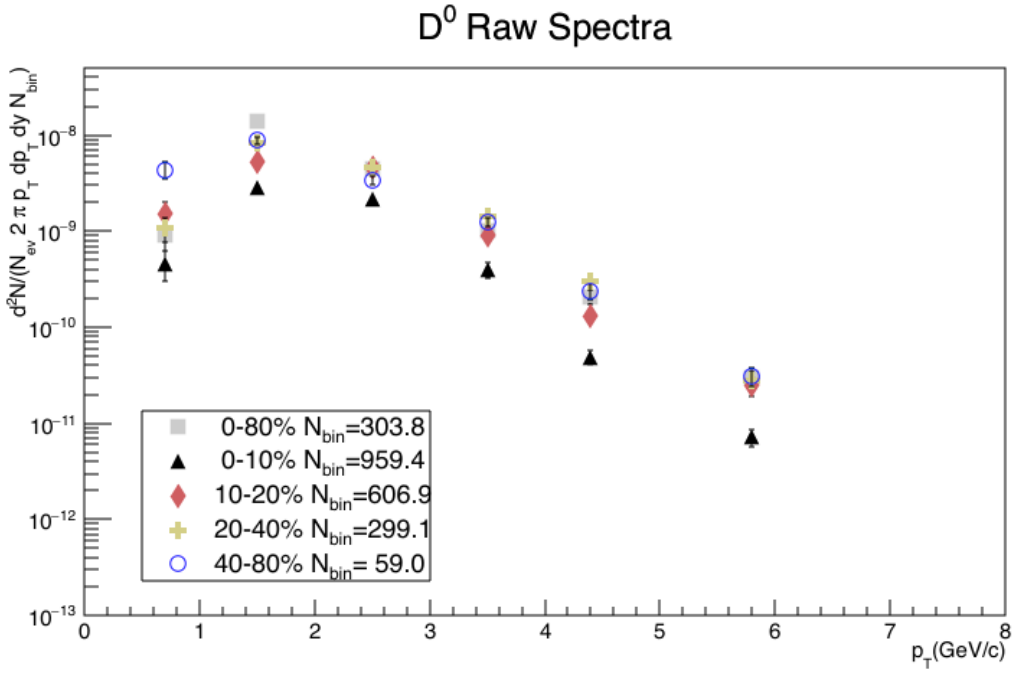

Figure 4.16: D^0 meson raw spectra for different centrality bins, normalized by the number of binary collisions. The average number of binary collisions for each centrality bin is shown in the figure insert.

4.4.1 Nuclear modification factor R_{CP}

The nuclear modification factor R_{CP} can be defined as the ratio of the central to peripheral collision transverse spectra, in contrast to the R_{AA} value where the base line is p+p collisions. The difference is that in R_{CP} one uses the most peripheral centrality bin as a good approximation of a baseline, i.e. collisions without nuclear effects, thus implicitly ignoring possible Cold Nuclear Matter effects in the peripheral bin. The advantage of R_{CP} over the R_{AA} is that most systematic uncertainties cancel out. The only remaining corrections are tracking and D^0 reconstruction efficiency differences between the two centralities but those can be (and are) estimated using Hijing simulations. The R_{CP} quantity compares the number of particles produced at central collisions (where the traversed path-length through the fireball is longer than particles created at peripheral collisions) to the particles produced at peripheral events, normalized to the binary collisions, as a function of p_T. Thus this ratio represents a good estimate of the energy lost of the particles in the medium since a longer time inside the medium might represent larger energy lost. Figure 4.17 shows the R_{CP} result with the efficiency corrections we presented in section 4.2. Tracking efficiency is expected to favor the peripheral sample relative to the central one and this will lead to lower values than the real ones. On the other hand, the worse vertex resolution at peripheral events, relative to central ones, affects more the D^0 reconstruction efficiency and this effect, if corrected, would lead to higher values than the real ones. Only through a full de-convolution of the interplay of these two effects (this study is underway in STAR) can give us the precise net effect. Here we assume that the net effect is much smaller that the estimated systematic errors.

We observe that high p_T (>3 GeV) charm-mesons are strongly suppressed in central Au+Au collisions and at levels similar to that of light quarks. We also see that there is little, if any, suppression at intermediate values of p_T. Detailed comparisons with model predictions are needed in order to further understand the obtained distribution as we discuss below.

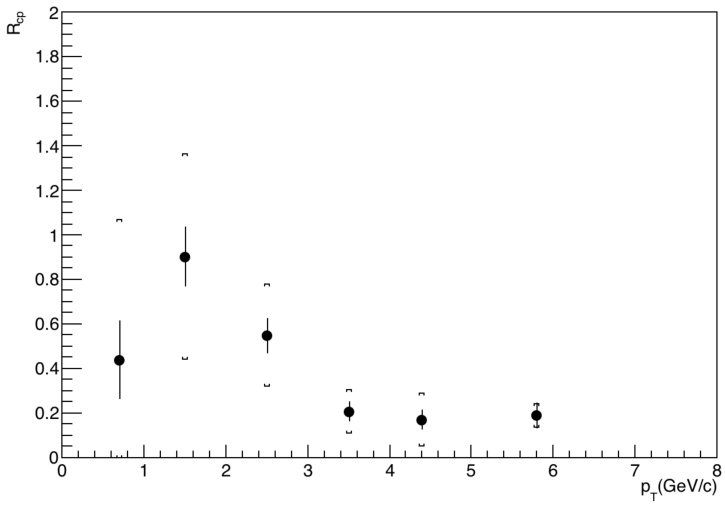

Figure 4.17: R_{CP} for D^0 mesons (with efficiency corrections). The estimated systematic errors are shown in brackets.

4.4.2 Nuclear modification factor R_{AA}

The nuclear modification factor R_{AA} provides crucial information about the particle under study and its interaction with the medium since QGP is not expected to form in p+p collisions. This quantity (equation 1.2) is the ratio that is related to the energy loss of a particle going through the hot partonic matter created in Au+Au 200 GeV collisions and depends of the slope of the p_T spectrum of the D^0. The ratio is

performed between the most central Au+Au events and the p+p base-line to take advantages of the particles with longer path in the medium.

In contrast to the previous R_{CP} measurement discussed above, the R_{AA} calculation uses two different sets of data, so precise efficiency corrections must be done and fully corrected spectra must be obtained before dividing them. By the time of this work, the STAR standard procedure for efficiency estimation via embedding simulated particles into real data was not developed because the HFT is a newly installed detector. A first approximation for R_{AA} calculation is performed with the results obtained in section 4.2 using Hijing simulation. Figure 4.18 shows the spectra obtained for the D^0 mesons reconstructed at the most central events 0-10% with the efficiency correction and the previous result from run 2010 and 2011 without the HFT [Adamczyk et al. 2014]. By the time of finishing this work a bug was found in the official STAR production. The results presented here are corrected for this bug to about 10-20% level.

The values for the p+p baseline come from the previous STAR results [Adamczyk et al. 2012]. One of the goals of p+p Run 2015 in STAR, with the HFT, is to improve this baseline to better constraint the R_{AA} calculation. The p + p result contains data for D^0 plus D^0 from D* feed-down (mainly above $p_T > 2$ GeV/c). The dashed curve is the data fitted to a Levy function to fit the p + p data and scaled to the number of binary collisions for the 0-10% most central events. The Levi function provide a power law approach to fit particle spectrum. It is known from pQCD calculations that a power law shape will describe the spectrum of a particle in the high p_T region. The function is given by (4.3):

$$\frac{d^2\sigma^{c\bar{c}}}{2\pi p_T dp_T dy} = \frac{1}{2\pi}\frac{(n-1)(n-2)}{(nT+m_0)[m_0(n-1)+nT]}\left(\frac{nT+\sqrt{p_T^2+m_0^2}}{m_0+nT}\right)^{-n} \quad (4.3)$$

where $d\sigma^{cc}/dy$, n and T are fitting parameters [Tlusty 2014].

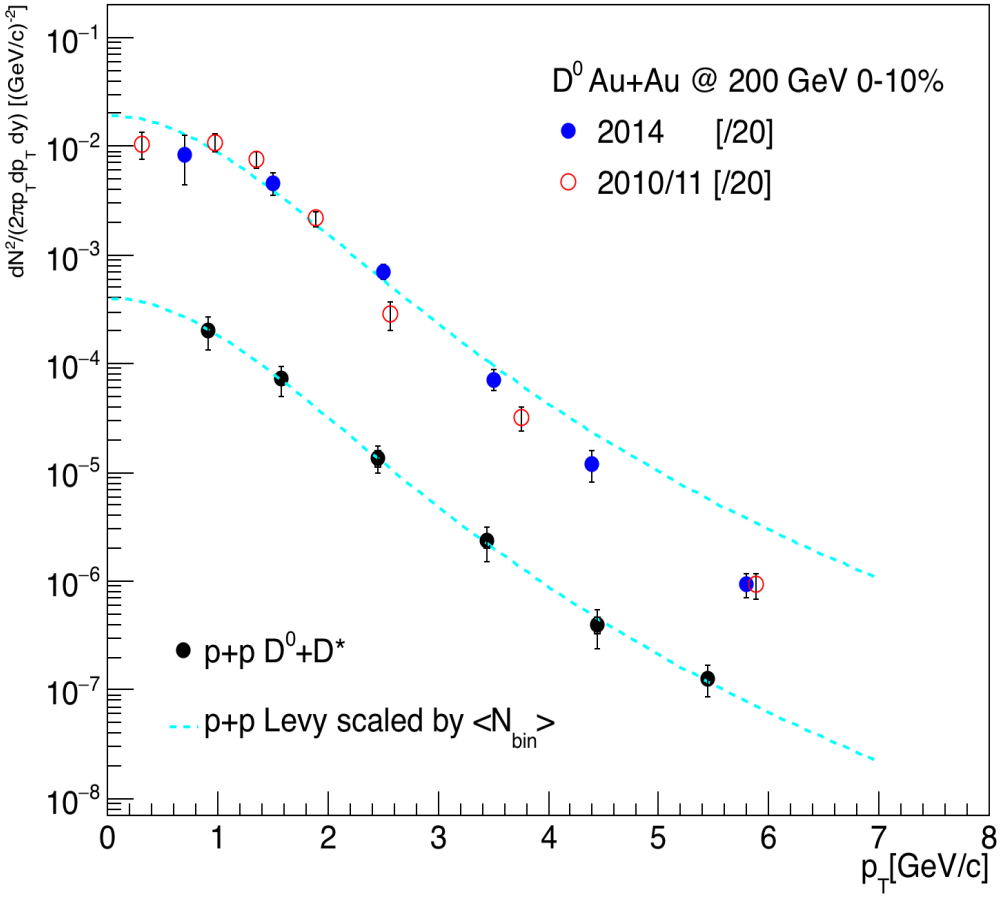

Figure 4.18: Corrected D^0 meson spectrum for the 0-10% most central Au+Au 200 GeV events from this analysis (blue points) and previously published STAR results for D^0 (open red points). The black points are STAR's results for p+p collisions at the same energy fitted and scaled with a Levy function.

Figure 4.19 shows the result of the R_{AA} (filled blue circles) obtained by using as a first approximation the efficiency and purity estimations in section 4.2, and compare with the previous result from STAR without the HFT and current STAR results with helix swim [Xie 2016]. The light green bar at the right of the figure represents the uncertainty of the Au + Au number of binary collision, while the dark green band is the normalization uncertainty for p + p collisions. Vertical lines and bars show the statistical and systematic errors respectively. Also shown in the same figure is our R_{CP} result that serves as an estimate of the overall systematic uncertainty. We observe that at high p_T values (>4 GeV) both results indicate a strong suppression while at intermediate p_T there seems to be little, if any, suppression.

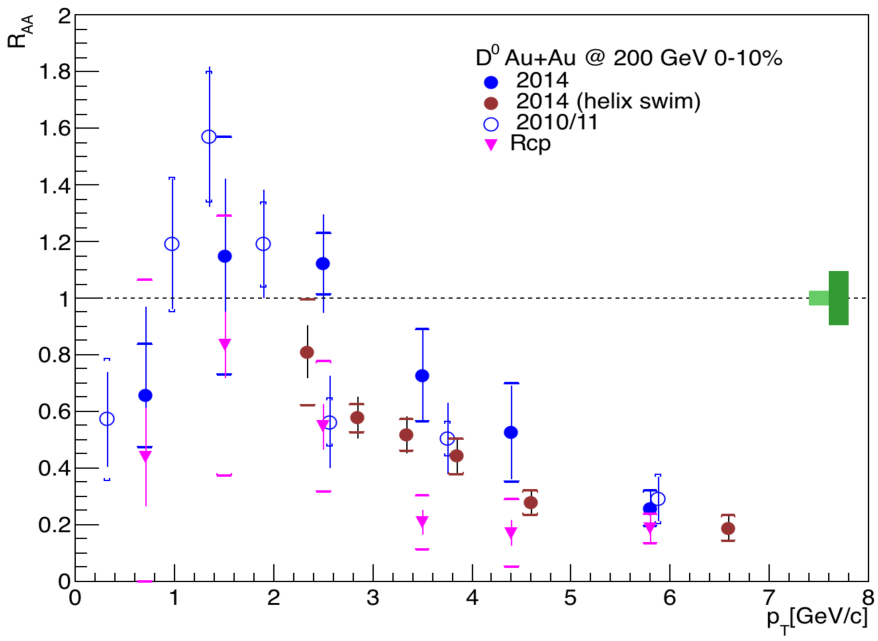

Figure 4.19: R_{AA} and R_{CP} estimation for D^0 mesons (solid blue circles and triangles), previously published STAR results without the HFT (open circles) and current STAR results using helix swim (red circles).

4.5 Comparisons with Theory and other Experiments

The table 4.3 shows the exact values of the results presented previously with the efficiency estimation (only central events) using the fitted function result and the average value of the pion-kaon contamination used for the R_{AA} calculation.

The results obtained for R_{CP} and R_{AA} clearly show the effect of the interaction of the D^0 meson with the medium formed due to the collision. The nuclear modification factor will be equal to one if there is no interaction with the medium; values above one relates to an excess in particle production that do not scale with the number of binary collisions, and values below one correspond to a suppression in the production.

Table 4.3: Results of the nuclear modification factors obtained.

p_T	R_{CP}	Error	Systematic	Eff.	R_{AA}	Error	Systematic
0.7	0.439	0.175	0.628	7.11E-5	0.655	0.311	0.185
1.5	0.902	0.134	0.459	9.36E-4	1.175	0.280	0.420
2.5	0.548	0.080	0.229	5.03E-3	1.186	0.184	0.109
3.5	0.208	0.045	0.095	8.70E-3	0.740	0.162	0.164
4.4	0.171	0.044	0.120	6.37E-3	0.513	0.161	0.174
5.8	0.057	0.057	0.053	1.15E-2	0.250	0.060	0.062

Experimental results from LHC and RHIC show suppression of the heavy quarks at $p_T > 2$ GeV [Adamczyk et al. 2014; Adam et al. 2015]. This effect can be modeled by gluon radiation; however mass hierarchy must be taken into account so it would be expected that heavy quarks lose less energy that light quarks. Figure 4.20 shows STAR results for pions [Abelev et al. 2007] and the results obtained in this work.

The result shows higher suppression of light and heavy quarks at higher p_T values (>4 GeV) Similar suppression was previously reported by RHIC and LHC, which led to revisit the energy loss calculations via gluon radiation.

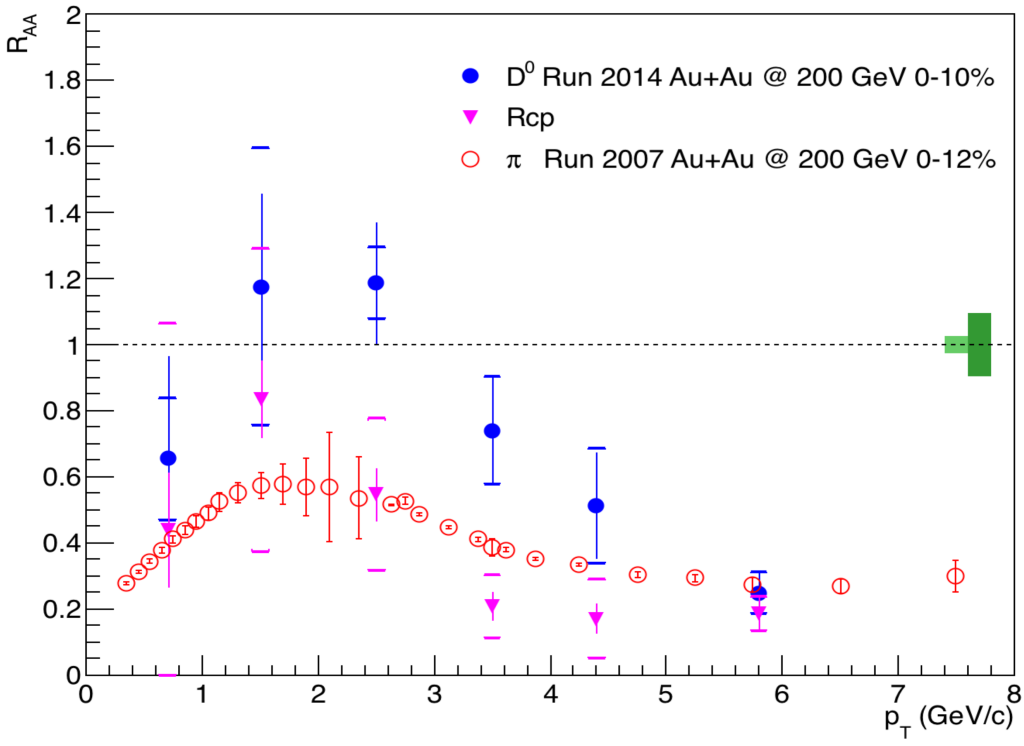

Figure 4.20: R_{AA} and R_{CP} estimations for D^0 mesons in this work and the previous STAR results for pions.

However, another main source of energy loss is elastic collisions, indicating a strong interaction of the particle with the medium at large transverse momentum [Adamczyk et al. 2014; Adam et al. 2015].

At low p_T, heavy quarks are more susceptible to the medium properties. Model calculations show that the collective behavior of these quarks is analogous to a Brownian

motion, so drag and or diffusion coefficient of the medium can be extracted. The collective motion can provide evidence of the degree of thermalization of these heavy quarks and compare with light quarks. Furthermore in this region of the spectrum, the large charm- pair abundance might increase the coalescence probability, which might result in enhancement. Model calculation with a finite charm flow and coalescence hadronization can reproduce this enhancement. Figure 4.21 shows the comparison between the results obtained in this work and several theoretical models in the literature.

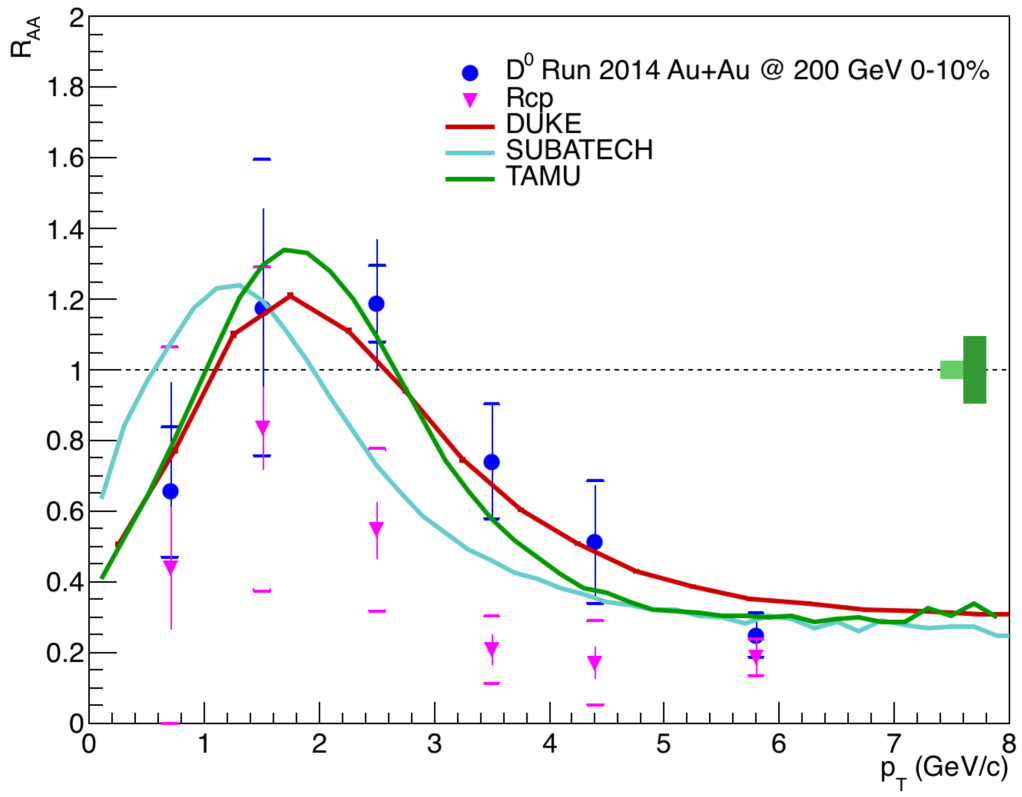

Figure 4.21: R_{AA} and R_{CP} estimation for D^0 mesons and three different theoretical predictions using coalescence.

The three models presented take quark coalescence into consideration. The Duke University group (DUKE) used a modified Langevin equation that incorporates both quasi-elastic scattering and gluon radiation, with (2+1)-D hydrodynamic simulation to represent the medium formed. The diffusion coefficient is a free parameter and it is fixed to fit the LHC results ($2\pi T \times D = 7$) [Cao et al. 2015]. The Subatech research laboratory group applies pQCD calculation and used the Hard Thermal Loop approximation (HTL) to estimate the charm interaction with the medium. Both radiative and collisional energy losses are considered, however radiative energy seem to be negligible at low transverse momentum [Nahrgang et al. 2015]. The Texas A&M University group (TAMU) used Langevin approach to model the quark propagation also in a (2+1)-D hydrodynamic medium but with no viscosity. The interaction of the charm quark with the medium is represented by the non-perturbative T-Matrix dynamical method. The calculations only consider collisional energy loss [He et al. 2013; Andronic et al. 2015].

The results obtained match qualitatively the theory model presented, indicating coalescence at low p_T, and suppression at high p_T. It is not possible at this point to make statements about which model the data favors but elliptic flow measurements favor a diffusion coefficient value in the range [2-10], which is in the TAMU model (dark green line in figure 4.21). The R_{AA} values also seem to slightly favor this model but not the R_{CP} ones; therefor no firm conclusions can be drawn at this time.

Previous STAR measurements (see figure 4.19) and recent results from ALICE [Adam et al. 2015] showed a large discrepancy at low/intermediate p_T values. One of the main reasons should be the complication to reconstruct short lifetime particle at low

transverse momentum for both experiment. Figure 4.22 shows a comparison between ALICE results and the results obtained in this work.

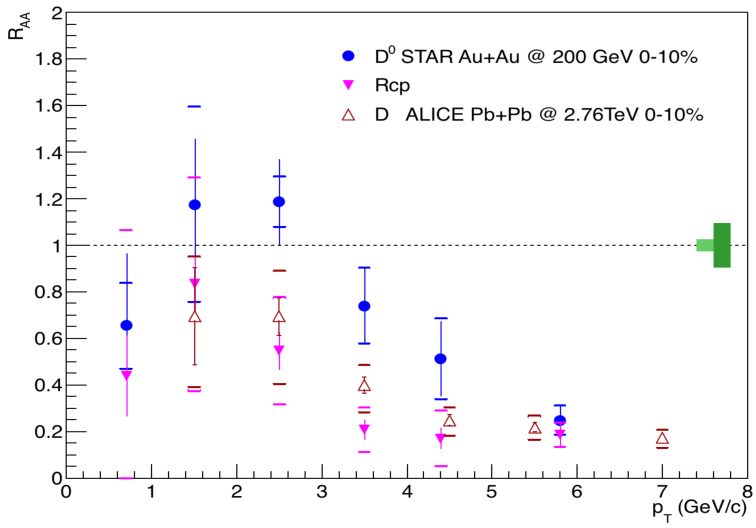

Figure 4.22: R_{AA} and R_{CP} estimation for D^0 mesons compared with recent ALICE results.

At $p_T > 2$ GeV, previous STAR result, recent ALICE results, the theory and the results of this work seem to have some agreement, which indicates that classical approaches adapted to QCD, such as gluon radiation and elastic energy lost seems to describe correctly the medium. There is an indication of a difference at low p_T but we would need to improve our measurement before detailed comparisons and conclusions can be drawn. Experimentally it is very difficult to reconstruct heavy-quark mesons in this region so the theory still cannot be constrained. In this work a novel technique have been introduced to maximize the performance of the next generation of particles detectors and clarify the theoretical framework to understand the QGP.

CHAPTER 5

Summary and Outlook

Many advances have been made to elucidate the properties and behavior of the Quark Gluon Plasma since its discovery at RHIC. However this stage of matter is still not completely understood and its precise properties are still a hot topic and subject of debate within the scientific community. Precise measurements of many physics observables must be done in order to constraint the theoretical models and extract all the important parameters needed for its description. The new generation of particle detectors, like the Heavy Flavor Tracker, that perform precise topological reconstruction of short lived heavy flavor particles is expected to further help us understand high energy nuclear collisions. The commissioning of the HFT in 2014 has improved considerably the capabilities of the STAR experiment. The pointing resolution achieved with the HFT allows reconstruction of several of these short lifetime particles (D^0, $D^{\pm}$, D_s), not reachable with the previous detectors in STAR, and reducing considerably the combinatorial background (by ~4 order of magnitudes). The results have just started coming out and they are very encouraging; some have already been presented in major conferences and first results are being prepared for publication. But it is still an extremely difficult task to reconstruct charmed mesons in some of the most challenging regions of transverse momentum, for example at $p_T < 1$ GeV/c and the most central events where the multiplicity and background are very large. These points are critical for the physics

analysis since the energy loss mechanism at this low p_T region would not play a dominant role, so the motion of the heavy quarks in the medium might be use to extract its properties.

In this work, an algorithm based on the Kalman Filter was used to reconstruct D^0 mesons. The KFParticle package reconstruct short lifetime particle by fitting the daughter tracks considering the full covariance matrix of each track. The package provides the traditional used topological variables (like DCA), but it also gives the error of the decay length and deviations of the DCA. Using a ratio of these variables and the probability of the fit (also provided by the package), the D^0 meson is reconstructed (figure 3.8) in the $K+\pi$ channel, obtaining a good significance. Since the calculation of the mother particle parameters using KFParticle are more elaborated rather than using helix swimming, the computational time increased considerably (~10 times slower per event) so unique particle identification per track was implemented to reduce the combinatorial background and therefore the total computing time. The major complication of this unique PID requirement per track method arises at the region where neither the TPC nor the TOF can distinguish between particles. When TOF information is available (60% of all tracks), the track was identified to be whatever value of the expected result for either pion or kaon with TOF is closes to. In the case when no TOF info is available, a first approach using multivariate techniques and simulated particles was use to discriminated between pion and kaons where the TPC cannot make it. This approach was discarded due to poor results thence every track in this overlap region between kaon and pion is considered to be a pion; in section 4.2 we estimate the purity of this approximation. It is worth

mentioning that the current STAR infrastructure does not have a full and realistic TOF simulation, so a future task after this issue is solved will be to redo the multivariate analysis to separate kaons and pions also using TOF information. The unique PID per track method will be of major impact for several analysis, since it will reduce considerably the background and avoid double counting of the same track but different identification.

The signal optimization performed used multivariate techniques otherwise commonly known as machine learning. Traditional analyses used simple rectangular cuts to optimize the signal, however for multivariable studies this is usually a poor choice. The training performed belongs to the class of supervised training since the expected signal and background is given. The signal used is a Geant simulation of pure D^0 in the studied channel and the background is a small portion of the data sample. The four variables used to extract the non optimized signal where used for the training phase. Different combinations of variables from the KFParticle package were used, however the initial four variables used provide the best discrimination power (see figure 3.13). Several classifiers were tested and the best result was obtained using BDT. From these four initial variables in the training, the classifier provides a single variable (in this work called "TMVA cut") that separated the signal and the background. For the physics analysis this value must be optimized per p_T and centrality bin, so the cut was systematically varied per each bin to maximize the significance. Ideally an individual training per bin might be done, however the computational time and disk space required for a usable simulation

will be enormous so this method is not viable unless more computational resources are available.

All the signals obtained per each p_T and centrality bin studied have significance larger than 5; except for $p_T < 1$ GeV (which are the most difficult ones to obtain) and one bin at centrality 10-20% high p_T that have significances larger or close to 3. The raw spectra of D^0 meson are presented using this optimization. For accurate spectra calculations the proper efficiency correction must be perform. The standard embedding method for efficiency calculation with the HFT was not available at the time of completion this work therefore an estimation of efficiencies was performed using Hijing+Geant simulations.

The nuclear modification factors R_{CP} and R_{AA} were calculated in this study using the simulation-based efficiencies. For the R_{AA}, the Hijing simulation and particle PID contamination was taken into account. Both quantities (R_{CP} and R_{AA}) show a strong suppression at high p_T, an effect that was also observed in previous measurements. No suppression is also observed at $p_T \sim 2$ GeV which is consistent with previous STAR measurements and consistent with models of hadronization via coalescence.

The methods presented in this work are not restricted to the particle studied. Reconstruction of more challenging particles like Λ_C, might be performed since the current studies had failed to reconstruct this particle. The combination of a Kalman Filter base reconstruction algorithm and signal optimization using multivariate techniques have proved to be helpful tools in short lifetime particle reconstruction and in difficult regions of the p_T and centrality.

REFERENCES

[Aad et al. 2013] Aad, G. et al. (2013), "Evidence for the spin-0 nature of the Higgs boson using ATLAS data", Physics Letters B Volume 726, Issues 1–3, 7 October 2013, pp. 120–144.

[Aaij et al. 2014] Aaij, R. et al. (2014), "Observation of the Resonant Character of the $Z(4430)^-$ State", Physics Review Letters 112, 222002, 4 June 2014, pp. 1-9.

[Aaij et al. 2015] Aaij, R. et al. (2015), "Observation of J/ψp resonances consistent with pentaquark states in Λ^0_b -> $J/\psi K^-$ p decays", Physical Review Letters 115, 072001, 15 August 2015, pp. 1-15.

[Abelev et al. 2007] Abelev, B. et al. (2007), "Energy dependence of charged pion, proton and anti-proton transverse momentum spectra for Au+Au collisions at $\sqrt{s_{NN}}$ = 62.4 and 200 GeV", Phys. Letters B 655, pp.104-113.

[Ackermann et al. 2003] Ackermann, K. H. et al. (2003), "STAR detector overview", Nuclear Instruments and Methods in Physics Research A 499, pp. 624–632.

[Adam et al. 2015] Adam, J. et al. (2015), "Transverse momentum dependence of D-meson production in Pb-Pb collisions at $\sqrt{s_{NN}}$ = 2.76 TeV", arXiv:1509.06888.

[Adamczyk et al. 2012] Adamczyk, L. et al. (2012), "Measurements of D^0 and D* production in p+p collisions at $\sqrt{s_{NN}}$=200 GeV", Phys. Rev. D 86, 072013.

[Adamczyk et al. 2014] Adamczyk, L. et al. (2014), "Observation of D^0 Meson Nuclear Modifications in Au+Au Collisions at $\sqrt{s_{NN}}$=200 GeV", Phys. Rev. Lett. 113,

142301, 30 September 2014.

[Adams et al. 2003] Adams, J. et al. (2003), “Evidence from d+Au measurements for final state suppression of high pT hadrons in Au+Au collisions at RHIC”, Physics Review Letters 91, 072304.

[Adams et al 2005] Adams, J. et al. (2005), “Experimental and theoretical challenges in the search for the quark–gluon plasma: The STAR Collaboration's critical assessment of the evidence from RHIC collisions”, Nuclear Physics A Volume 757, Issues 1-2, 8 August 2005, pp. 102-183.

[Adare et al. 2007] A. Adare et al. (2007), “Energy Loss and Flow of Heavy Quarks in Au+Au Collisions at $\sqrt{S_{NN}} = 200GeV$”, Phys. Rev. Lett. 98, 172301.

[Adcox et al. 2005] Adcox, K. et al. (2005), “Formation of dense partonic matter in relativistic nucleus–nucleus collisions at RHIC: Experimental evaluation by the PHENIX Collaboration”, Nuclear Physics A Volume 757, Issues 1-2, 8 August 2005, pp. 184-283.

[Agostinelli et al. 2003] Agostinelli, S. et al. (2003), “Geant4 - a simulation toolkit”, Nuclear Instruments and Methods in Physics Research A, Volume 506, Issue 3, 1 July 2003, pp. 250–303

[Alpaydin 2010] Alpaydin, E. (2010), “Introduction to Machine Learning”, 2nd edition, The MIT Press, Cambridge Massachusetts.

[Anderson et al. 2003] Anderson, M. et al. (2003), “The STAR time projection chamber: a unique tool for studying high multiplicity events at RHIC”, Nuclear Instruments and Methods in Physics Research A 499, 659.

[Andronic et al. 2015] Andronic, A. et al. (2015), "Heavy-flavour and quarkonium production in the LHC era: from proton-proton to heavy-ion collisions", arXiv:1506.03981, 21 November 2015.

[Arsene et al. 2005] Arsene, I. et al. (2005), "Quark–gluon plasma and color glass condensate at RHIC? The perspective from the BRAHMS experiment", Nuclear Physics A Volume 757, Issues 1-2, 8 August 2005, pp. 1-27.

[Back et al. 2005] Back, B. et al. (2005), "The PHOBOS perspective on discoveries at RHIC", Nuclear Physics A Volume 757, Issues 1-2, 8 August 2005, pp. 28-101.

[Beddo et al. 2003] Beddo, M. et al. (2003), "The STAR Barrel Electromagnetic Calorimeter", Nuclear Instruments and Methods in Physics Research A 499, 725.

[Bichsel 2006] Bichsel, H. (2006), "A method to improve tracking and particle identification in TPCs and silicon detectors", Nucl. Instrum. Meth. A 562, 154.

[Bieser et al. 2003] Bieser, F. S. et al. (2003), "The STAR trigger", Nuclear Instruments and Methods in Physics Research A 499, 766.

[Bushwick 2010] Bushwick, S. (2010), "How Low Can RHIC Go?", https://www.bnl.gov/newsroom, 22 July 2010.

[Cacciari, Nason, Vogt 2005] Cacciari, M., Nason, P. and Vogt, R. (2012), "QCD Predictions for Charm and Bottom Production at RHIC", Phys. Rev. Lett. 95, 122001, 14 August 2015.

[Cao et al. 2015] Cao, S., et al. (2015), "Energy loss, hadronization and hadronic interactions of heavy flavors in relativistic heavy-ion collisions", Phys. Rev. C 92, 024907.

[Chaudhuri 2012] Chaudhuri, A. K. (2012), "A short course on Relativistic Heavy Ion Collisions", arxiv:1207.7028.

[Contin 2015] Costin, G. (2015), "The STAR Heavy Flavor Tracker (HFT) and Upgrade Plan", Quark Matter 2015.

[CPEP 2014] Cotemporary Physics Education Project (2014), http://www.cpepphysics.org/images/2014-fund-chart.jpg.

[Gorbunov, Kisel 2007] Gorbunov, S. and Kisel, I. (2007), "Reconstruction of decayed particles based on the Kalman Filter", CBM-SOFT-note-2007-003, 7 May 2007.

[Gross, Wilczek 1973] Gross, D. J. and Wilczek, F. (1973), "Ultraviolet behavior of non-abelian gauge theories", Physical Review Letters 30 (26), pp. 1343–1346.

[He et al. 2013] He, M. et al. (2013), "D_s Meson as a Quantitative Probe of Diffusion and Hadronization in Nuclear Collisions", Phys. Rev. L. 110, 112301, 11 March 2013.

[Heinz 2013] Heinz, U. (2013), "Towards the Little Bang Standard Model", arXiv:1304.3634.

[Hoecker et al. 2007] Hoecker, P. et al. (2007), "TMVA - Toolkit for Multivariate Data Analysis", arXiv:physics/0703039.

[Hu-Guo et al. 2010] Hu-Guo, C. et al. (2010), "First reticule size MAPS with digital output and integrated zero suppression for the EUDET-JRA1 beam telescope", Nucl. Instrum. Methods Sect. A 623 p. 480.

[ITTF 2003] STAR Integrated Tracking Task Force (2003), "STAR Integrated Tracker", https://drupal.star.bnl.gov/STAR/system/files/ITTF.pdf.

[Joseph 2011] Joseph, J. (2011), "Charmed meson measurements using a sillicon tracker in Au+Au collisions at $\sqrt{S_{NN}}$ = 200 GeV in STAR experiment at RHIC", Kent State University Ph.D. dissertation.

[Kalman 1960] Kalman, R. E. (1960), "A New Approach to Linear Filtering and Prediction Problems". Journal of Basic Engineering 82: 35.

[Llope 2003] Llope, W. J. (2005), "The large-area time-of-flight upgrade for STAR" Nuclear Instruments and Methods in Physics Research B 241 306.

[Llope 2014] Llope, W. J. (2014), "The STAR Vertex Position Detector", Nuclear Instruments and Methods in Physics Research A Volume 759, 21 September 2014, pp. 23–28.

[Margetis 2009] Margetis, S. (2009), "A Heavy Flavor Tracker for STAR", http://phys.kent.edu/~margetis/STAR/HFT/CD0/hft_final_submission_version.pdf

[Mehtar-Tani et al. 2013] Mehtar-Tani, Y. et al. (2013), "Jet physics in heavy-ion collisions", Int. J. of Mod. Phys. A, Vol. 28, 1340013.

[Muller 2015] Muller, B. (2015), "A New Phase of Matter: Quark-Gluon Plasma Beyond the Hagedorn Critical Temperature", arXiv:1501.06077.

[Nahrgang et al. 2015] Narhgang, M. et al. (2015), "Elliptic and triangular flow of heavy flavor in heavy-ion collisions", Phys. Rev. C91, 014904, 20 January 2015.

[Ng 2014] Ng, A. (2014), "Machine Learning", https://www.coursera.org

[Olive et al. 2014] Olive, K. A. et al. (2014), "Review of Particle Physics", Chinese Physics C, vol. 38, 090001.

[Politzer 1973] Politzer, H. D. (1973), "Reliable perturbative results for strong interactions". Physical Review Letters 30 (26), pp.1346–1349.

[Poskanzer, Voloshin 1998] Poskanzer, A. M. and Voloshin, S. A. (1998), "Methods for analyzing anisotropic flow in relativistic nuclear collisions", Physics Review C 58, pp. 1671-1678.

[Qiu 2014] Qiu, H. (2014), "STAR Heavy Flavor Tracker", Nuclear Physics A, Volume 931, November 2014, pp. 1141–1146.

[Reed, 2010] Reed, R. et al. (2010), "Vertex finding in pile-up rich events for p+p and d+Au collisions at STAR", J. Phys.: Conf. Ser. 219, 032020.

[Ryder 1996] Ryder, L. H. (1996), "Quantum Field Theory", Cambridge University Press, 2nd edition.

[Senyukov 2013] Senyukov S. (2013), "The upgrade of the ALICE Inner Tracking System", Nucl. Instrum. Meth. A 732, December 2013, pp. 164-167.

[Sinervo 2002] Sinervo, P. (2002), "Signal Significance in Particle Physics", arXiv:hep-ex/0208005.

[Sjöstrand et al. 2015] Sjöstrand, T. et al. (2015), "An introduction to PYTHIA 8.2", Computer Physics Communications Volume 191, June 2015, pp.159–177.

[Snellings 2011] Snellings, R. (2011), "Elliptic Flow: A Brief Review", New J.Phys.13:055008.

[Tlusty 2014] Tlusty, D. (2014), "A Study of Open Charm Production in p+p Collisions at STAR", Czech Technical University in Prague Ph.D. dissertation.

[Ullrich 2009] Ullrich, T. (2009), "What is the Effective Signal and what is it good for? ", http://phys.kent.edu/~smargeti/STAR/D0/NoteOnEffSignal.pdf.

[Walsh 2013] Walsh, K. M. (2013), "Accelerating Particles Accelerates Science", https://www.bnl.gov/rhic/news2/news.asp?a=3758&t=today.

[Wang 2014] Wang, Y. (2014), "Intermediate Silicon Tracker for STAR HFT upgrade", Quark Matter 2014.

[Wang, Gyulassy 1992] Wang, X. and Gyuliassy, M. (1992), "Gluon shadowing and jet quenching in A+A collisions at $\sqrt{s_{NN}}$=200 GeV", Phys.Rev.Lett. 68, pp. 1480-1483.

[Wang, Gyulassy 1994] Wang, X. and Gyuliassy, M. (1994), "HIJING 1.0: A Monte Carlo Program for Parton and Particle Production in High Energy Hadronic and Nuclear Collisions", Comp. Phys. Comm. 83, 307.

[Xie 2016] Xie, G. (2016), "Nuclear Modification Factor of D^0 Meson in Au+Au Collisions at $\sqrt{s_{NN}}$=200 GeV", arXiv:1601.00695.

[Yang et al. 2014] Yang, C. et al. (2014), "Calibration and performance of the STAR Muon Telescope Detector using cosmic rays", Nucl. Instrum. Meth. A 762 1.

[Zhang 2013] Zhang, Y. (2013), "Measurement of D^0 production in Au+Au collisions at $\sqrt{s_{NN}}$=200 GeV", STAR note PSN0594.

[Zee 2010] Zee, A. (2010), "Quantum Field Theory in a Nutshell", 2nd edition, Princeton University Press, p. 172.